



Materials processing by gas cluster ion beams

Isao Yamada^{a,*}, Jiro Matsuo^b, Noriaki Toyoda^a, Allen Kirkpatrick^c

^a*Himeji Institute of Technology, CAST, Kamigori, Hyogo 678-1205, Japan*

^b*Ion Beam Engineering Experimental Laboratory, Kyoto University, Sakyo, Kyoto 606-8501, Japan*

^c*Epion Corporation, Billerica, MA 01821, USA*

Received 10 November 2000; received in revised form 30 May 2001; accepted 30 May 2001

Abstract

This paper discusses the principles and experimental status of gas cluster ion beam (GCIB) processing as a promising surface modification technique for practical industrial applications. Theoretical and experimental characteristics of GCIB processes and of related equipment development are described from the moment of neutral cluster formation, through ionization, acceleration and impact upon a surface. The impact of an accelerated cluster ion upon a target surface imparts very high energy densities into the impact area and produces non-linear effects that are not observed in the impacts of atomic ions. Unique characteristics of GCIB bombardment have been found to offer potential for various industrial applications that cannot be achieved by conventional ion beam processing. Among prospective applications are included shallow ion implantation, high rate sputtering, surface cleaning and smoothing, and low temperature thin film formation. Sputtering effects produced by cluster ion impact are particularly interesting. High sputtering yields and lateral distribution of sputtered atoms cause surface smoothing effects which cannot be achieved with monomer ion beams. Surface smoothing to atomic levels is expected to become the first production use of GCIB. © 2001 Elsevier Science B.V. All rights reserved.

Keywords: Gas cluster ion beam (GCIB); Scanning tunneling microscope (STM); Time-of-flight (TOF)

1. Introduction

When a macroscopic object impacts at high velocity with a large rigid mass, both the surface deformation and the conversion of energy into internal degrees of freedom at the point of contact are substantial. Examples of large-scale impacts can be seen on the surface of the moon where there are about 10,000 craters which are visible to telescopes on the earth. About one thousand of the lunar craters are larger than 1 km in diameter. Other examples of meteor crater formation are seen on the surfaces of many planets. On the earth, approximately 50,000 years ago, a metallic asteroid about 30 m in diameter impacted in northern Arizona and caused formation of a 1.2 km wide crater. An image of this meteor crater is shown in Fig. 1(a). The shape of the crater formed by impact of this large meteor is quite typical and exhibits characteristic formation of a large rim comprised of ejected material [1]. Under impact conditions in the hyper-velocity regime, i.e. more than a few km/s, impacted regions experience high-temperature and high-pressure transients which produce fusion or vaporization of both target and projectile materials and cause craters or hole formation.

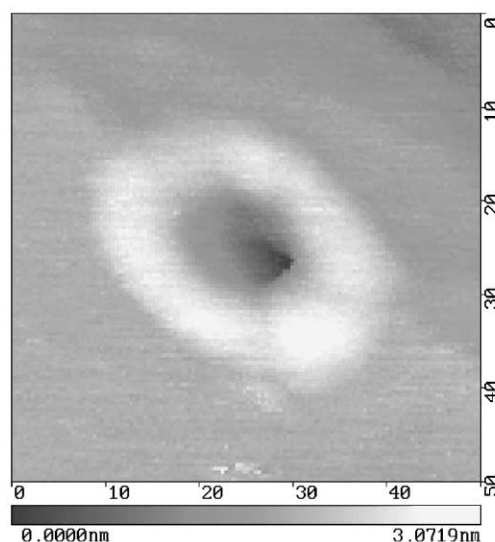
On the microscopic scale, similar craters are created on solid surfaces as a result of impacts of high energy particles or heavy ions [2]. As an example, Fig. 1(b) shows a scanning tunneling

* Corresponding author. Tel.: +81-75-753-5951; fax: +81-75-751-6774.

E-mail address: i-yamada@kuee.kyoto-u.ac.jp (I. Yamada).



(a) The meteor crater at North Arizona
(1.2 km in diameter)



(b) STM image of a crater on Au with Ar cluster ion impact.
(30 nm in diameter)

Fig. 1. Macroscopic and microscopic view of craters.

microscope (STM) image of a micro-crater on an Au surface due to impact of an Ar cluster ion consisting of 3000 atoms and having total energy 150 keV. The crater shown on the Au surface is approximately 30 nm in diameter [3], which is 4×10^{10} times smaller than the meteor crater which was shown in Fig. 1(a). According to estimations made by molecular dynamics (MD) simulations, interactions during energetic cluster ion impact induce transient temperatures of tens of thousands of degrees and transient pressures of tens of GPa within the impact zone of a target surface [4]. Equivalent phenomena are not produced by monomer ion impacts which involve binary collisions

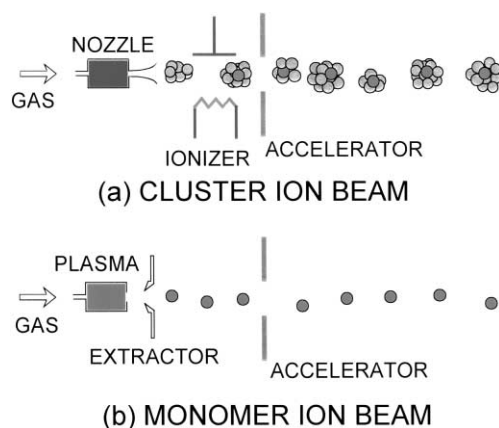


Fig. 2. The basic differences between impacts of monomer and cluster ions.

and do not introduce similarly high energy densities into the impact volume. In the field of materials processing, distinctive irradiation effects are expected due to cluster ion bombardment.

Gas cluster ion beam (GCIB) processing of materials is based on the use of electrically charged cluster ions consisting of a few hundreds to a few thousands of atoms or molecules of gaseous materials. Individual gas atoms are first condensed into neutral clusters which are subsequently ionized and accelerated. When an energetic cluster ion impacts upon a surface, it interacts nearly simultaneously with many target atoms and deposits high energy density into a very small volume of the target material. The concurrent energetic interactions between many atoms comprising the cluster and many atoms of the target result in highly non-linear sputtering and implantation effects which are fundamentally different from those associated with the simpler binary collisions which take place during monomer ion impacts [5–7]. Fig. 2 shows the basic difference between monomer ion and cluster ion beam system. Fig. 3 indicates the fundamental characteristics of cluster ion/solid interaction and identifies possible areas of applications.

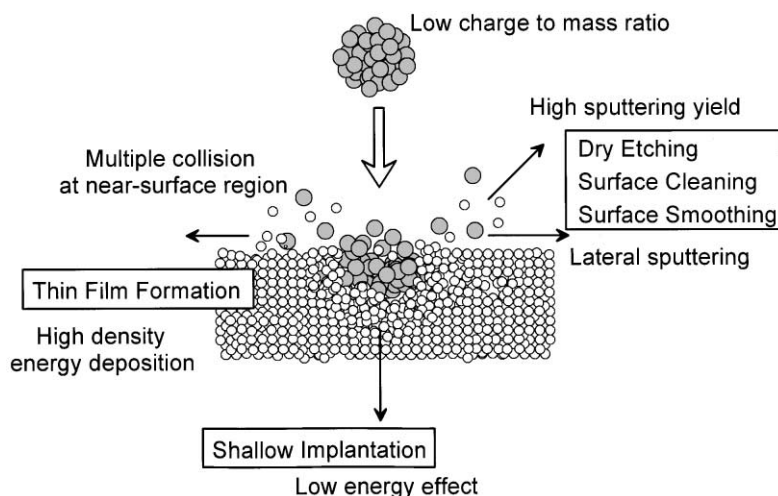


Fig. 3. Diagram showing a cluster impacting on a surface the various effects and typical applications.

In addition to the non-linear effects of the dense energy interaction properties of cluster ions, there are other distinct advantages of using GCIBs for processing applications. One of these advantages relates to the low charge to mass ratio of cluster ions. Cluster ions consisting of up to several thousands of atoms will typically carry only a single electrical charge or a small number of charges. Consequently, a cluster ion beam at any given current density can transport several orders of magnitude more atoms than a monomer ion beam at the same current density. For example, a 1 μA beam of singly-charged cluster ions having average size of 1000 atoms per cluster transports the same number of atoms as a 1 mA monomer ion beam.

Another advantage of GCIB processes is that they involve essentially low-energy individual atomic interactions even when the total energy of the clusters is high. Since the kinetic energy of each atom in a cluster ion is equal to the total energy of the cluster divided by the number of atoms comprising the cluster, cluster ion beams inherently produce low-energy irradiation effects. As an example, when a cluster ion consisting of 2000 atoms has 20 keV of total energy, each of the individual atoms has energy of only 10 eV. While, due to space charge effects, it is exceptionally difficult to transport monomer ion beams at energies as low as 10 eV, equivalently low-energy ion beams can be realized by using cluster ion beams at relatively high acceleration potentials. This characteristic can be very useful for shallow implantation. Using conventional monomer ion beam processes, it is difficult to obtain high-current beams at very low acceleration energies. However, cluster ion beams can transport large numbers of low-energy atoms at low current densities.

GCIBs are now being used for producing novel materials exhibiting superior properties, for developing new chemical compositions and for altering, refining and machining of materials and surfaces. Examples include: low-damage, atomic-scale surface smoothing of metals [8], of polysilicon [9], of superconductors [10], of diamond films [11], of non-spherical plastic lens molds, and of SiC surfaces used for synchrotron radiation (SR) mirrors; shallow implantation for LSI junction formation [12]; high-rate and low-damage anisotropic surface etching for semiconductor device fabrication [13]; assisted-formation of thin multi-layer film coatings to be used in reliable and durable optical filters [14]. Some of the unique processes and properties are discussed below.

2. Cluster beam sources

2.1. Methods to generate cluster beams

The study of cluster beam formation was started during work on intense molecular beam flows [15]. It is well known that small numbers of clusters are produced by ejection of metal vapors from heated Knudsen cells. While a heated Knudsen cell has been one candidate for a cluster beam source, achievable beam intensities have usually been too low for practical experimental use [16,17]. Several other cluster generation methods have been investigated for fundamental study purposes but have not been found to be practical for process applications. These have included: laser ablation [18], sputtering using bombardment by heavy ions, and gas aggregation in which metal vapor is condensed in an inert gas cloud within a stagnation gas chamber [19]. For practical process applications, high intensity cluster beams are to be required.

Cluster formation through supersonic expansion was first studied by Becker et al. for thermonuclear fuel applications [20]. Basically the formation process involves a gas expanding from a high pressure source into vacuum through a small orifice. Adiabatic expansion reduces the relative velocity of the gas atoms and, as a result, clusters are formed. Clusters from many gases and compounds having high vapor pressures can be generated using supersonic nozzles. The supersonic

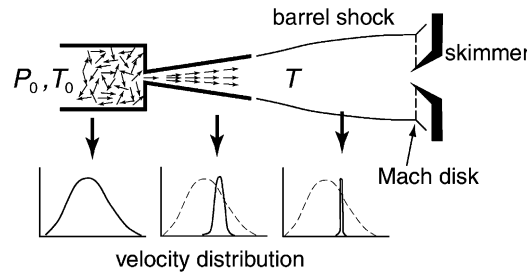


Fig. 4. Schematic diagram of the supersonic expansion and the velocity distribution of the particles.

expansion approach has been most successful to produce cryogenic beams containing large numbers of clusters [20,21]. Although it is difficult to apply this method to solid materials, supersonic expansion is considered to be the best cluster source for gaseous materials.

2.2. Cluster formation by supersonic expansion

Fig. 4 shows a schematic illustration of supersonic expansion from a nozzle. A gas of molecular or atomic mass m expands from a stagnation region at high pressure (P_0) into a vacuum through a small orifice of diameter D . The random velocity of gas atoms within the stagnation region is greatly reduced by the adiabatic expansion, causing all the atoms to move at nearly the same speed, v . A low local temperature is realized for a volume unit within the flow. Considering adiabatic steady flow of a gas, Bernoulli's equation relates the enthalpy in the stagnation region (H_0) with that of the flow (H) and with kinetic energy of the directed mass of flow [22]:

$$H_0 = H + \frac{1}{2}mv^2 = c_p T + \frac{1}{2}mv^2 = c_p T_0 \quad (2.1)$$

where c_p is the specific heat at constant pressure which is $(5/2)k$ for a monatomic gas, and T_0 and T are the temperatures in the stagnation region and in the flow region, respectively. As the Boltzmann constant $k = c_p - c_v$, where c_v is the specific heat at constant volume, Eq. (2.1) can be rearranged as follows:

$$T = T_0 \left[1 + \frac{1}{2}(\gamma - 1)M^2 \right]^{-1} \quad (2.2)$$

where M is the Mach number defined as the ratio of stream velocity v to the local sound speed $c = \sqrt{\gamma kT/m}$. The ratio of specific heat $\gamma = c_p/c_v$ at constant pressure and constant volume can be taken as independent of the temperature for an atomic gas. The Mach number M increases downstream along the beam, and it is described as [23]:

$$M = A \left(\frac{x}{D} \right)^{\gamma-1} \quad (2.3)$$

where A is 3.20 in the case of an atomic beam and x is the distance from the nozzle. For example, T is less than 1 K at $x = 30$ mm for an orifice of diameter 0.1 mm at room temperature T_0 . At the point where the hydrodynamic flow condition is no longer satisfied, there is a terminal velocity, generally at about a few degrees kelvin.

Cluster formation in a supersonic beam begins with a dimer formation process which occurs in tri-atomic collisions, due to energy and momentum conservation [24]:



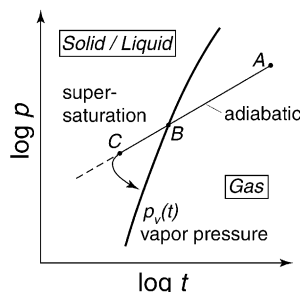


Fig. 5. Phase diagram under supersaturation.

To maintain energy conservation, the kinetic energy of monomers on the left hand side of Eq. (2.4) must be higher than that of those on the right-hand side. Once dimers are formed, they act as condensation nuclei for further cluster growth. If the ratio of atoms to clusters is large, a cluster grows by monomer additions. If the number of clusters is high, cluster–cluster aggregation becomes dominant. The cluster formation process starts within the hydrodynamic region and continues until atomic collisions cease. In the molecular flow region, no additional cluster formation takes place.

Cluster formation can be treated as a gas–fluid phase transition. Fig. 5 gives a schematic phase diagram of the gas flow during expansion. Point A represents the stagnation condition. During the expansion, the expanding gas follows the adiabatic line up to point B, where it meets the vapor pressure curve $p_v(t)$. Under thermal equilibrium conditions, the subsequent expansion proceeds along the $p_v(t)$ curve where gaseous and solid–liquid states coexist. However, this equilibrium expansion is not observed for the nozzle expansion, instead, the expansion continues along an adiabatic path. The gas state in this region is not stable, and is termed *supersaturated*. Soon the expanding gas departs from the adiabatic line at point C and tends to approach the vapor pressure curve $p_v(t)$. This transition from the supersaturated state is initiated by the formation and growth of clusters. A small particle or cluster of radius r has a vapor pressure P_r larger than vapor pressure P_0 of a plane surface:

$$\ln \frac{P_r}{P_0} = \frac{2\sigma m}{kT\rho} \frac{1}{r} \quad (2.5)$$

where σ and ρ are the surface tension of the small particle and its density, respectively. As r increases, the vapor pressure decreases. A cluster having a larger radius than critical value r^* grows, while a smaller one evaporates. Therefore, there are two peaks in the mass spectrum of the cluster beam: one is the exponential decay distribution of small clusters and the other is a wide distribution at the large cluster size region. Details of the mass spectra with time-of-flight (TOF) mass spectrometer results are discussed in Section 2.4.

2.3. Principles of GCIB equipment

The nozzle is a most significant component of a cluster beam source. Nozzle geometry determines flow, cluster size, beam divergence and temperature of the beam. The high rate of collisions among the atoms and molecules, and immediately following, the nozzle allows removal of the heat of condensation so that clusters can form. Only a small fraction of the total number of atoms or molecules in the gas flow become clusters. A variety of nozzles have been used to produce cluster

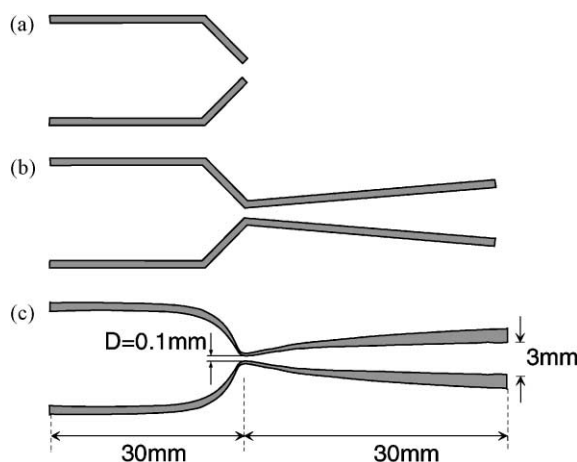


Fig. 6. Schematic diagrams of the nozzle shapes, as indicated: (a) sonic nozzle; (b) conical nozzle; (c) Laval nozzle.

beams. In Fig. 6, three types of nozzles are shown: sonic, conical and Laval configurations. The sonic nozzle is preferred for the study of small clusters of less than 10 atoms. On the other hand, conical and Laval nozzles are converging-diverging supersonic nozzles, and are more efficient than a sonic nozzle for forming intense cluster beams [24]. Cluster beam intensity (I) generated by supersonic expansion depends on the source pressure P_0 , nozzle diameter D and temperature of the source gas T_0 . It is described as follows [25]:

$$I \propto P_0 D \left(\frac{T_b}{T_0} \right)^{(\gamma/(\gamma-1))} \quad (2.6)$$

where γ and T_b are the specific heat ratio and the boiling point of the source gas, respectively. From Eq. (2.6), the neutral beam intensity I increases with P_0 and $1/T_0$ when D and T_b are fixed.

Fig. 7 shows dependence of the neutral beam intensity on the source gas pressure at temperatures $T_0 = 300$ and 220 K for an example Laval nozzle having a throat diameter of 0.1 mm and a diffuser length of 30 mm. In the case shown, the flow rate of Ar was 600 sccm at a stagnation pressure of 4000 Torr. The neutral beam intensity could be determined by observing the difference in

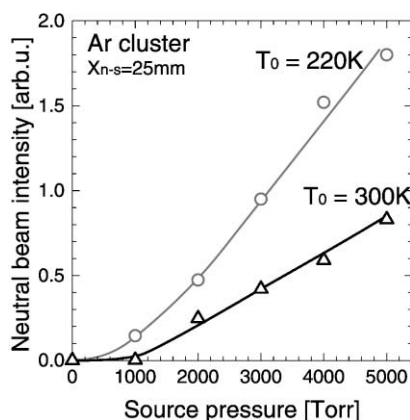


Fig. 7. Source pressure and temperature dependence of neutral beam intensity.

vacuum pressure at the target chamber when the beam shutter was opened or closed. The neutral beam intensity started to increase from P_0 of 1000 Torr and increased monotonically with P_0 . When the source gas temperature was lowered from 300 to 220 K, the neutral beam intensity at the same P_0 was twice as high as that at 300 K. High gas pressures and low gas temperatures are important to obtaining intense cluster beams.

After expansion of the gas out of a nozzle, a skimmer having the shape of a truncated cone is usually employed to separate the cluster-containing core of the gas stream from the molecular flow. Skimmers are typically made from electroformed Ni and have entrance aperture edges made as sharp as possible to avoid collisional distortion of the impinging gas flows. The distance between skimmer and nozzle (x_{n-s}) has been found to be important in obtaining intense cluster beams. In the case of a short x_{n-s} , distortion of the flow downstream of the skimmer is probable. If the skimmer is located far from the nozzle, the neutral cluster beam collides with the residual gases and a shock wave called a *Mach disk* is generated upstream of the skimmer. In this case, intensity of the neutral cluster beam through the skimmer decreases. From numerical studies, the position of the shock wave (x_m) is approximated as follows [26]:

$$x_m = 0.67D \sqrt{\frac{P_0}{P_s}} \quad (2.7)$$

where D , P_0 and P_s are the nozzle diameter, source gas pressure and pressure in the vacuum chamber, respectively. Eq. (2.7) indicates that the position of the Mach disk is determined by the vacuum pumping speed within the source chamber. Under suitable vacuum conditions, the Mach disk will form at least several centimeters from the nozzle exit. Fig. 8 shows a schematic illustration of one example of a basic GCIB apparatus. A collimated neutral cluster beam is formed by supersonic expansion of a gas from a pressure of several atmospheres into vacuum through a small nozzle. A skimmer, aligned with the axis of expansion, removes a large portion of the non-clustered gas and allows some fraction of the more forward-directed clusters to pass through. Gas flow rate through the supersonic nozzle is typically several hundreds of sccm. High-speed pumps are required in order to reduce pressures within the nozzle region, and in the regions after the skimmer. Ionization of neutral clusters which pass through the skimmer is usually performed by electron bombardment. Electrons emitted from multiple tungsten filaments are accelerated by a voltage (V_e) applied between the filaments and a cylindrical anode. Ionization efficiency should depend upon the cluster size. Because of their larger cross-sections, clusters are expected to be ionized much more efficiently than

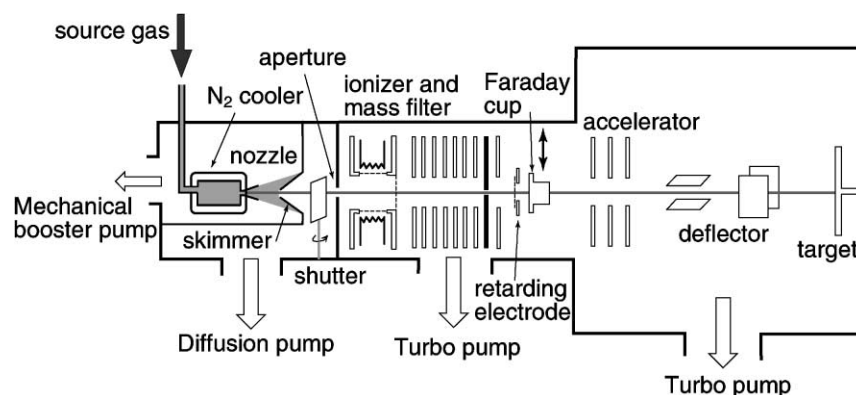


Fig. 8. Schematic diagram of the 30 keV GCIB apparatus.

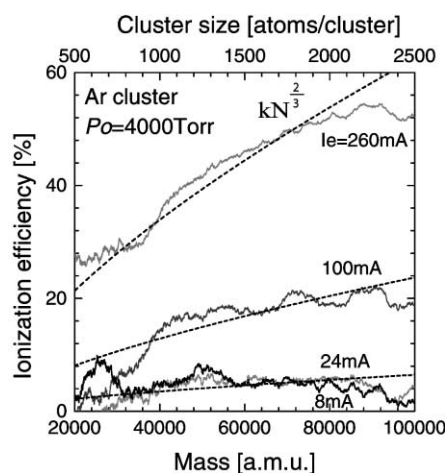


Fig. 9. Cluster size dependence of the ionization efficiency. Ionization was performed by electrons with $V_e = 300$ eV energy.

monomers. Fig. 9 shows experimental results concerning ionization efficiency of Ar clusters as a function of cluster size at different ionization electron currents (I_e) for fixed ionization energy of 300 eV. Dotted lines shown in the figure represent fitting functions $kN^{2/3}$ where k is an arbitrary constant and N is the cluster size. The ionization efficiency was found to increase with cluster size regardless of the ionization electron current. As the cross-section of a cluster with size N is proportional to $N^{2/3}$, a cluster is much easier to ionize than a monomer.

Ionized clusters can be extracted and accelerated within a series of electrodes. As the velocity of all neutral particles (clusters and monomers) is the same, the initial kinetic energy of a monomer is much lower than the total energy of a cluster consisting of many atoms. Thus, the content of monomer ions in a cluster ion beam can be reduced by means of space charge effects by employing only a low voltage (~ 10 V) on the first extraction electrode. Only cluster ions which have large initial kinetic energies are extracted. After extraction using the low voltage, the cluster ions can subsequently be accelerated by a higher voltage (~ 2 kV). In apparatus configured as in Fig. 8, cluster ions have been focused by a series of electrostatic lenses. After elimination of the monomer ions from the beam, the cluster ions are accelerated up to 30 keV, by means of an acceleration column. Following acceleration, two pairs of electrostatic deflector electrodes can be employed to raster the cluster beam uniformly over a selected target area. Ion dose can be measured by integration of the current collected on the target. When a cluster ion impacts upon a target, large numbers of secondary electrons are emitted, resulting in an increase in the observed ion current and causing dose measurement errors. Usually, in order to allow correct beam current measurements, an electrode biased negatively with respect to the target is employed to suppress secondary electron emission from the target.

Formation of clusters from a variety of gases has been studied. From Ar and CO₂ gases, cluster beams are usually produced at room temperature using conical or Laval-type nozzles. In the case of other gases, such as N₂, O₂ and SF₆, it is often difficult to directly form intense cluster beams at room temperature. To produce intense cluster beams from such gases, instead of employing expansion of the pure gas, He gas can be mixed with desired gas as a carrier. The role of the He, which does not become incorporated into the clusters, is to assist in heat removal during the nozzle expansion. Fig. 10 shows cluster beam intensities from a room temperature nozzle for SF₆, CO₂, Ar, N₂O, N₂ and O₂ gases mixed with He gas as functions of the gas ratios. It has been observed that neutral

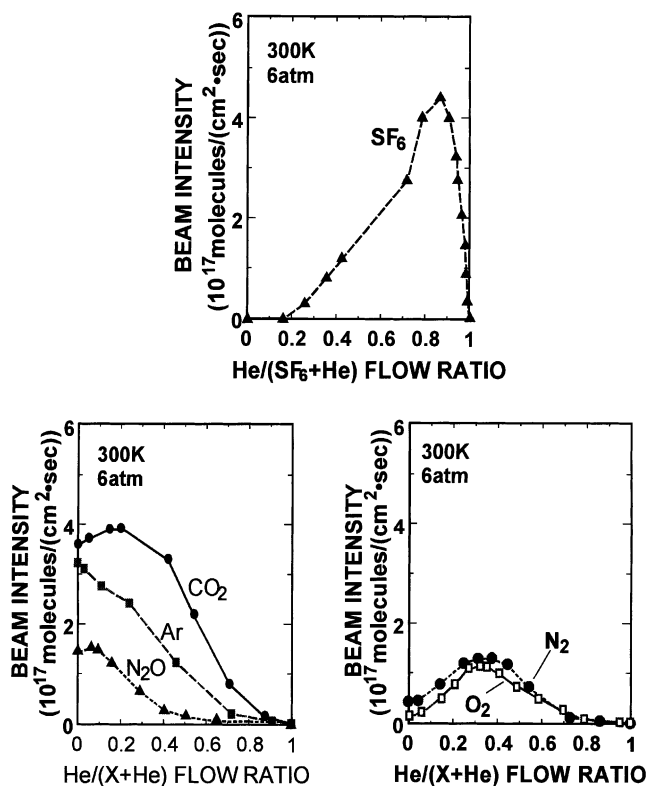


Fig. 10. Cluster beam intensities as functions of He gas mixture ratios.

cluster beam intensities can be increased by up to two orders of magnitude by incorporation of a modest amount of He into the source gas.

2.4. Cluster size distributions

Clusters generated as described above can have large size of up to 10,000 atoms or more. To correctly determine cluster size distributions, equipment which allows analyses over a wide mass range is required. Three methods have been used for measuring size distributions. One method which employs an electrostatic field (retarding field method) is very simple but has poor mass resolution. A second method uses quadrupole mass spectrometry (QMS) which is capable of resolving only relatively small clusters, but has very good mass resolution. The third method employs a TOF mass spectrometer which is suitable for very large clusters but has poor mass resolution large cluster. These methods are described below.

2.4.1. Retarding field method

The principle of the retarding potential method of measuring cluster size distributions is based upon the fact that the kinetic energy of a neutral cluster is proportional to the cluster size. Though the mass resolution with this method is quite low, it is the simplest and easiest way to measure the approximate cluster size distribution. During supersonic expansion, atoms collide with each other and exchange energy. Subsequently, the translational velocity of all particles becomes the same. As all particles, from monomers to clusters, have the same velocity, the kinetic energy is proportional to

the cluster size N . The velocity (v) and kinetic energy (K) are described as follows:

$$v = \sqrt{\left(\frac{\gamma}{\gamma - 1}\right) \frac{2kT_0}{m}} \quad (2.10)$$

$$K = \frac{1}{2} N m v^2 = \left(\frac{\gamma}{\gamma - 1}\right) k T_0 N \quad (2.11)$$

where m , γ , k and T_0 are the atomic mass of the monomer, the ratio of the specific heats, Boltzmann constant and the temperature of the source gas, respectively. In the case of Ar ($\gamma = 5/2$), the velocity is 560 m/s at room temperature, which corresponds to energy per atom of 0.065 eV. The cluster size distribution can be obtained from the energy distribution of the beam. Fig. 11 shows a schematic diagram of an ionizer, lens system, retarding electrode and Faraday cup and indicates typical electric potentials for retarding potential measurements. In this method, each cluster ion able to overcome an applied retarding potential contributes to the ion current measured by a Faraday cup. When the retarding potential is lower than the acceleration voltage, all the ions reach the Faraday cup. However, when the retarding potential exceeds the acceleration voltage, low-energy particles such as monomers and small clusters are repelled, but larger cluster ions with higher energy are still able to pass through. Therefore, the retarding potential works as a high-pass energy filter, and the cluster size distribution can be obtained from the negative derivative of the retarding spectrum. Fig. 12 shows cluster size distributions determined from the derivative of the beam current versus retarding potential curves for an Ar cluster beam at low and high extraction voltages. The source pressure (P_0) during these measurements was 4000 Torr and the extraction voltage (V_{ext}) was either 12 or 500 V as shown. As can be seen in Fig. 12, a cluster ion beam under high extraction voltage conditions contains many monomer ions and small clusters, but under low extraction voltage conditions, the monomer and small cluster components are quite minor.

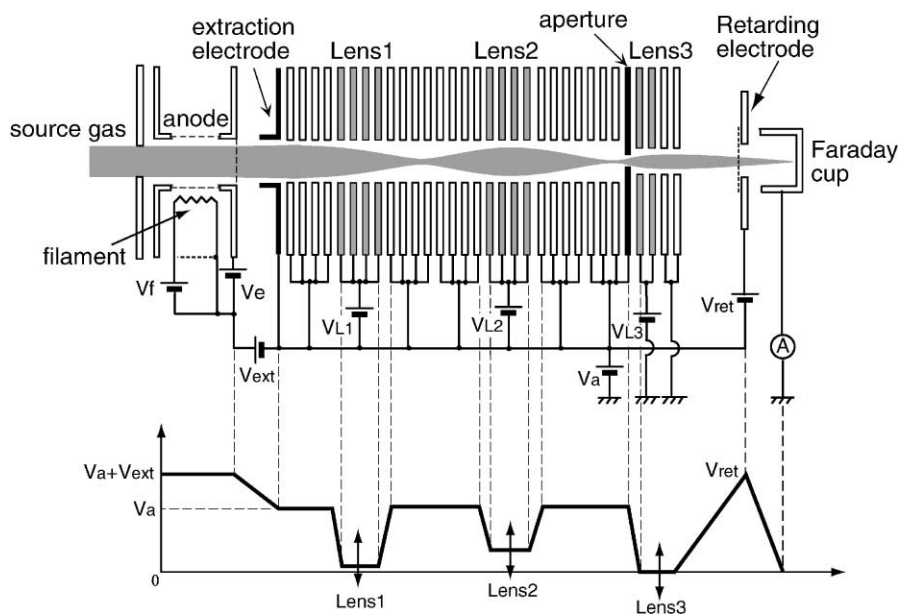


Fig. 11. Schematic diagram of the ionizer and the associated electric potential.

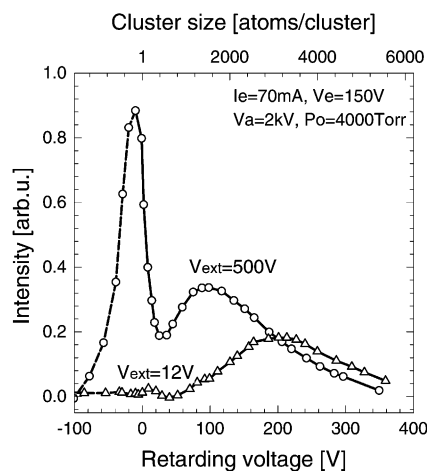


Fig. 12. Ar cluster size distribution at low (12 V) and high (500 V) extraction voltages measured with the retarding potential method.

To assess the validity of the size distributions obtained by the retarding potential method, mass distributions of cluster ions which passed a retarding electrode were also measured using a TOF mass spectrometer method which will be described in detail in Section 2.4.3. Fig. 13 shows TOF spectra from an Ar cluster ion beam without acceleration which was passed through a field aperture to which retarding voltages (V_{ret}) of 0, 50, 100 and 150 V were applied. For kinetic energy of 0.065 eV per cluster atom, the retarding field voltages of 50, 100 and 150 V correspond to cluster sizes of 775, 1550 and 2325 atoms, respectively. From Fig. 13, it can be seen that as V_{ret} was

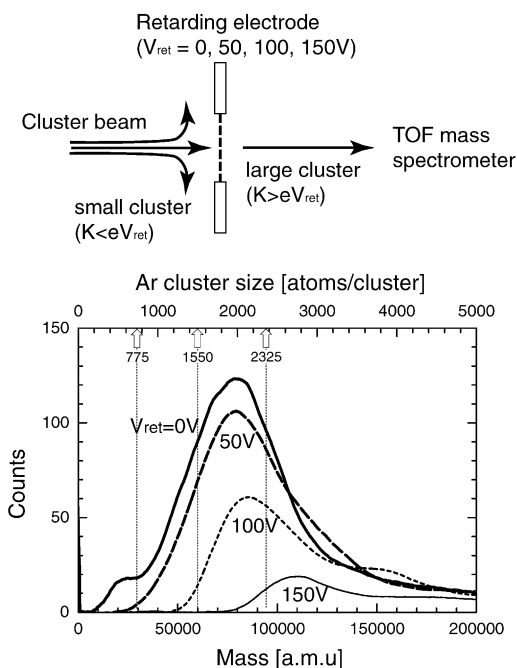


Fig. 13. Ar cluster size distribution after filtering with the retarding potential method. The retarding voltages V_{ret} of 50, 100 and 150 V correspond to the cluster sizes of 775, 1550 and 2325 atoms, respectively.

increased, the minimum size of the clusters which were able to pass the retarding field electrode shifted to larger values.

The mass resolution of the retarding potential method is defined principally by the uniformity of the potentials at the ionizing point and at the retarding electrode. The energy resolution of a typical retarding electrode is about 10 eV which corresponds to a size resolution of approximately 150 atoms. Therefore, the mass resolution of this method is quite coarse compared with that of other mass spectrometers. However, the retarding potential method only requires positioning of an electrode on the ion beam axis, and is the easiest way to perform an approximate determination of the cluster size distribution.

2.4.2. Quadrupole mass spectrometer analysis method

In order to confirm cluster formation and to observe the size distribution of small clusters with high mass resolution, a quadrupole mass spectrometer (QMS: Stanford Research Systems RGA-300) has been used. Fig. 14 shows the mass spectrum of an Ar cluster beam measured by the QMS. Ionization of the clusters was performed using 70 eV electron bombardment. As the atomic mass of Ar is 40, the peaks observed at atomic mass intervals of 40 can be attributed to Ar_n clusters. Although the mass resolution of the QMS is very good, the mass range is limited to less than 300 atomic mass units, which corresponds to a maximum cluster size of seven atoms in the case of Ar. In order to obtain further information concerning larger cluster sizes, TOF mass spectrometry which is discussed below can be used.

2.4.3. TOF mass analysis method

A typical TOF mass spectrum of Ar clusters with sizes of up to 35 atoms is shown in Fig. 15. The source pressure was 4000 Torr and the ionization energy was 70 eV. The spectrum shows many peaks at intervals of 40 atomic mass units, which is equivalent to the mass of an Ar atom. In Fig. 15, the intensity of Ar_n can be seen to decrease exponentially with cluster size. Fig. 16 shows TOF wide-range mass spectra taken at different stagnation pressures P_0 from 760 to 3800 Torr. The ionization energy and the acceleration energy for all spectra were 70 and 1.5 keV, respectively. At P_0 of 760 Torr, the cluster beam intensity can be seen to decrease suddenly with cluster size, starting from monomers. In this condition, the clusters grow by monomer additions. At P_0 of 1500 Torr, the decay is no longer exponential, and there is a small maximum at a size of around 500 atoms per cluster.

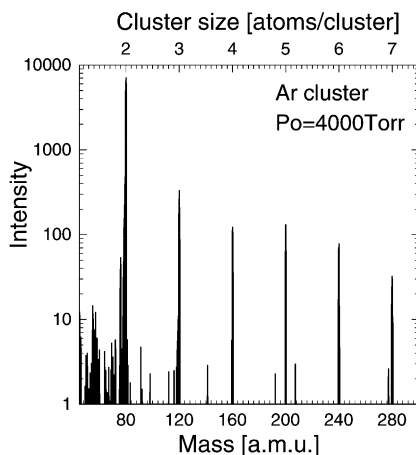


Fig. 14. Mass spectrum of an Ar cluster beam measured with a quadrupole mass spectrometer (mass range 1–300 amu).

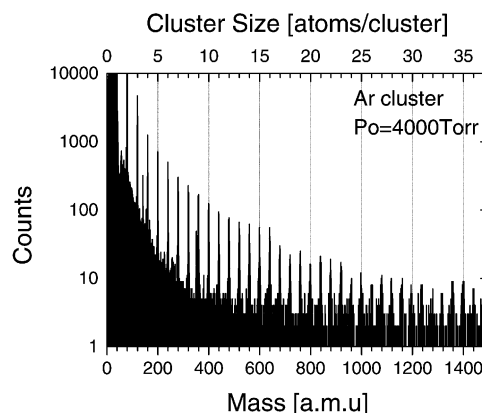


Fig. 15. Mass spectrum of an Ar cluster beam with the TOF mass spectrometer (mass range 1–1500 amu).

With increasing P_0 , the position of the peak of the size distribution can be seen to shift to larger sizes, and the dip observed at the size of about 200 atoms becomes more pronounced. The mass spectrum is expressed as the combination of two distributions, exponential decay in the small size region and wide distribution in the larger cluster region. When P_0 is high, clusters grow not only by monomer additions but also by cluster–cluster aggregation, which contributes to the broad distribution at larger sizes. Beyond a critical size N^* , cluster–cluster aggregation becomes the dominant mechanism for growth of large clusters. The critical size N^* can be estimated from the ‘dip’ in the TOF spectra to be around 200 atoms per cluster at P_0 above 1500 Torr. As can also be observed in Fig. 16, both the total number of clusters and their sizes increase significantly with P_0 above 1500 Torr.

It is well known that there is an enhanced abundance of clusters for particular ‘magic numbers’ which can be successfully explained in terms of the stability of certain close packed shell structures [27]. In the case of Xe, for example, enhancement of the intensity has been observed at sizes of

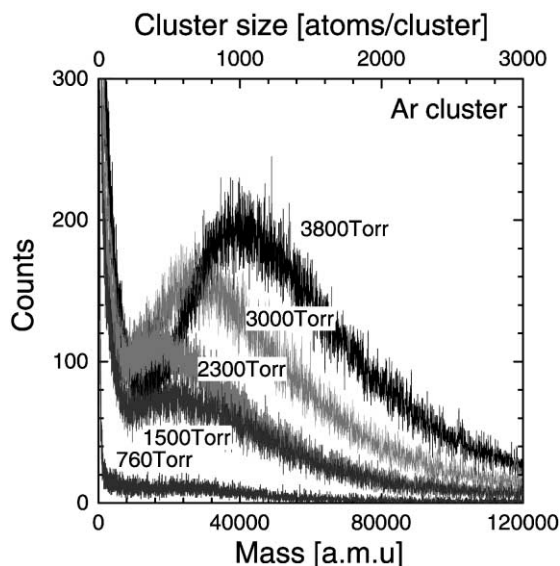


Fig. 16. TOF spectra of Ar large clusters at different source gas pressures up to 3000 atoms per cluster.

13, 55 and 147 atoms, an effect which has been attributed to the icosahedral structures. However, no enhancement at these sizes was reported in the case of Ar, and this was also true in our experiments over the range in which measurements could be performed.

2.5. Beam transport and charge state — advantages of cluster ion beams

According to the Child–Langmuir law, the maximum current density J_{\max} which can be extracted from a plasma ion source is related to the extraction voltage (V) and particle mass (m) and is limited by $J_{\max} \sim V^{3/2}/m^{1/2}$ [28]. Extraction of ions with energies of only a few hundreds of eV from a source is very difficult. Cluster ion beams may solve this problem [13]. A cluster ion of size N transports N times as many atoms as does a single monomer ion. However, at the same energy per atom, the cluster ion can be extracted at N times higher extraction voltage. Therefore, the relative maximum atom flux with GCIB can be expressed as the following:

$$\text{Atom flux} \sim N \times \frac{(NV)^{3/2}}{(Nm)^{1/2}} = N^2 \times J_1 \quad (2.12)$$

where N is the cluster size, J_1 the current density of atomic ions which have the same energy per atom as the cluster and hence penetrate to about the same depth.

The space-charge balance in a high-current beam is another well-known difficult problem in the transport of low-energy ions. Without proper beam neutralization, coulombic repulsion among ions in the beam will lead to beam expansion and lower beam current on the target. The effect becomes increasingly severe as the beam energy decreases or the beam current increases. Cluster beams can provide higher mass transport capability before being excessively affected by space-charge effects and beam blow-up. A cluster ion beam is less susceptible to these problems because the ions are at higher energy and the mass flux at given beam current is very high, as determined by the average number of atoms in each clusters. Reduced beam expansion means more uniform implantation, lower ion-loss on walls or electrodes, and simplified beam neutralization and focusing.

A further advantage of cluster ions can be a reduction in surface charging problems. The ion charge arriving at a target surface per atom of arriving material is reduced as the size of the cluster increases, by three orders of magnitude for the case of singly-charged clusters with $N \sim 1000$. This can greatly simplify the task of controlling surface charging on wafers by means of electron or plasma flooding.

3. Process fundamentals

3.1. Interaction kinetics

When an accelerated cluster ion hits a solid surface, it creates a small, highly compressed and heated “spike” region [29]. The atoms of the target undergo multiple collisions with one another, resulting in a highly non-linear collision cascades. Fig. 17(a) shows a snapshot, and Fig. 17(b) a momentum profile, for a collision of an Ar cluster upon a Si (1 0 0) target as simulated by MD. The snapshot represents a time of 1.2 ps after the impact of a 688 Ar atom cluster having 80 eV per atom. When the cluster collides with the target, the kinetic energy of the cluster is transferred to the target isotropically and a symmetrical crater is formed. Within the region close to the crater, the atomic arrangement has become highly disordered. In the momentum profile (Fig. 17(b)) the radius of the circles and the length of the lines represent the mean kinetic energy and the direction of the

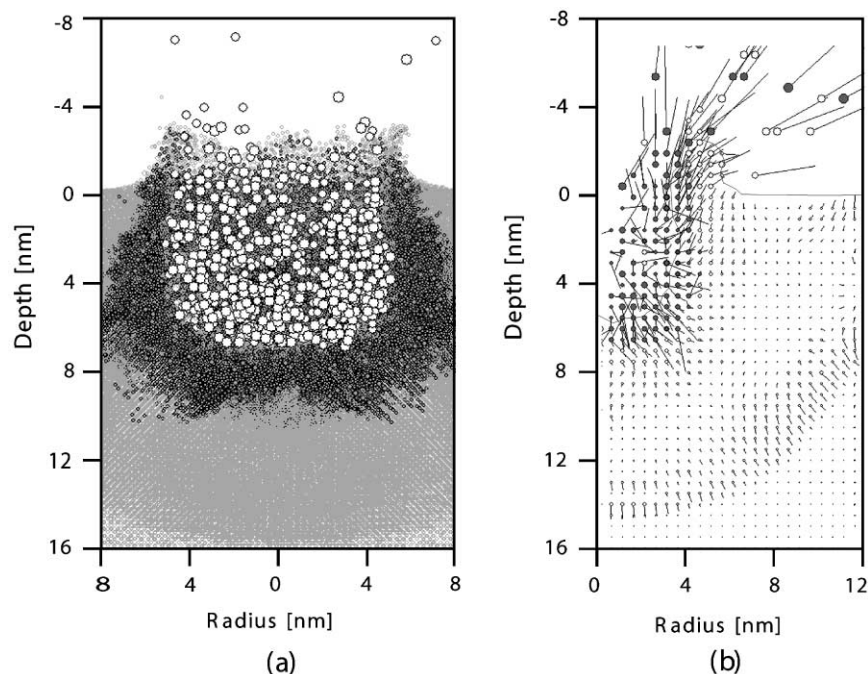


Fig. 17. Cross-sectional snapshot of an Ar_{688} impact with 55 keV energy calculated by MD simulation, 1.2 ps after the impact (a) and energy (circles) and momentum (lines) profiles for the same impact (b). Filled circles show the kinetic energy of the cluster atoms and open circles are for target atoms.

momentum, respectively. These results indicate that many particles are sputtered with directions lateral to the trajectory of the impinging cluster. They also show that many atoms with large lateral momentum become present in the rim of the crater. The kinetic energy of these atoms is higher than 2 eV. Fig. 17(b) also shows a shock wave which propagates outward from the impact region.

These phenomena lie well beyond the limits of the Sigmund linear collision theory [30]. Cluster impact involves electronic excitation of both the projectile and the target [31]. The impacted area experiences both high temperature and pressure transients: local temperatures can rise to 10^4 or 10^5 K and pressures can rise to a few Mbar [4]. As examples, Fig. 18(a) and (b) show the calculated temperature and pressure at 362 fs after the impact of a 50 keV Ar_{349} cluster on a Si substrate. The local pressure after the cluster impact has a roughly cylindrical shape with a very sharp steep front. Such a shock wave can lead to new physical phenomena that do not occur when a single atomic ion bombards a surface. Shock waves which occur during macroscopic body impacts on planets, during explosions [32], during laser ablation of solid surfaces [33], during high energy pulsed ion or laser beam impact on an inertial confinement fusion target [34,35], and during large organic molecule impacts [36], are of much scientific and technological interest [37]. Some of the potential consequences of the shock wave from the impact of an ionized cluster have been simulated and experiments to verify these predictions are in progress. The possibility that they may initiate non-equilibrium phase transitions, such as that from graphite to diamond, is worth exploring.

Very high sputtering yields have been observed experimentally on metal, semiconductor and insulator surfaces due to bombardment by heavy ions [38,39] and by cluster ions [40,41] and have been studied by computer simulation [42–46]. MD simulation results are represented in Fig. 19. The MD simulation of the sputtering yield Y from metal surfaces due to Ar_n cluster ion bombardment (with $N = 200$ –800) at energies of 6–20 keV fits a power dependence $Y \sim E^{1.4}$ on the total cluster

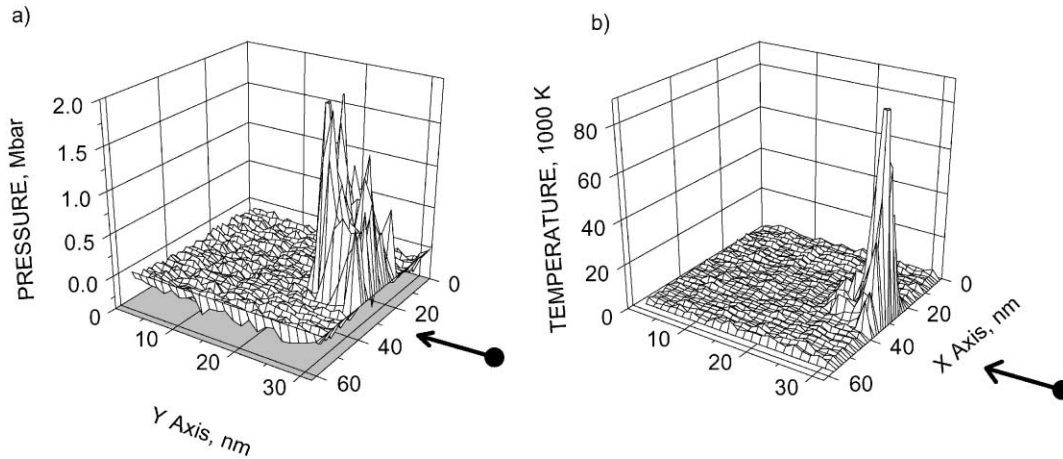


Fig. 18. Local target pressure (a) and temperature (b) calculated by MD simulation for 362 fs after a Ar_{349} cluster impact on a Si surface. Arrows show the direction of cluster impacts.

energy, in good agreement with experiment, at least for energies of 15 keV and higher [40,41]. The power exponent of this expression, 1.4, is close to the value of 1.5 which was obtained in a thermal spike model of high velocity impacts of macroscopic bodies at velocities in the range $(V_p/v) \sim 1\text{--}10$, where V_p and v are the projectile and sound velocities, respectively [47].

In Fig. 20, the angular dependence of sputter ejection is shown and the results of MD simulation for normal incidence on a Cu surface are compared with experimental data for 20 keV Ar_{3000} clusters. A tendency toward “lateral sputtering” is clearly evident in the experimental data and is even more evident in the MD simulation. Fig. 20 also shows the MD simulation of the strongly forward directed sputtering which occurs when the cluster is incident at 60° from the normal. These angular distributions of sputtered particles are important in producing surface smoothing (and roughening). The asymmetry that develops in the rim of the crater with off-normal incidence is also important. Taking these symmetries and asymmetries into account, Monte Carlo computer

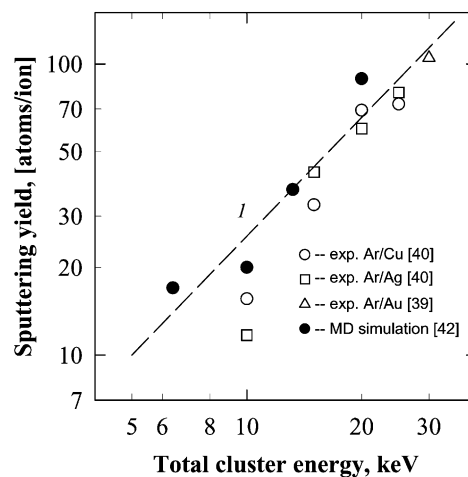


Fig. 19. Calculated and experimental sputtering yields (Y) as a function of total cluster energy (E). The line 1 represents fitting of the MD simulation data by a dependence: $Y \sim E^{1.4}$. Experimental data: open circles — Ar/Cu [41], squares — Ar/Ag [41], triangle — Ar/Au [40]. Our MD simulation results — filled circles.

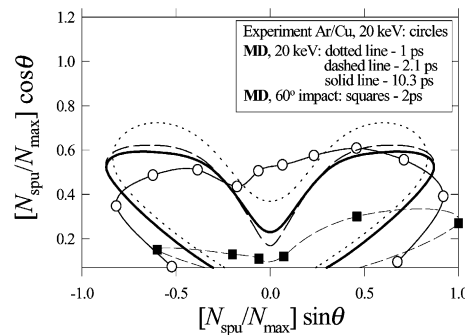


Fig. 20. Angular distribution of sputtering yield obtained for a 20 keV Ar_{3000} cluster impact with normal direction on a Cu surface: circles show our experimental data and lines are our MD simulation results at different time intervals after the impact: dotted line — 1.2, dashed line — 2.1 and solid line — 10.3 ps. Squares show our MD simulation results for cluster impact on a Si surface at an oblique direction 60° off-normal.

simulation models can predict smoothing due to bombardment at normal incidence and roughening due to impacts at oblique incidence [46].

Fig. 21 shows Monte Carlo simulation results obtained for 20 keV Ar_{1000} cluster beams impacting on a model “rough” Si surface. Fig. 21(a) shows a 10 nm high \times 100 nm wide hill before irradiation. Fig. 21(b) and (c) show the same region after cluster beam irradiation with a dose of 1×10^{13} ions/cm² at normal incidence, and at 60° off-normal, respectively. Bombardment with sufficient dose at normal incidence can produce very effective smoothing of the hill, whereas at off-normal incidence, the surface is roughened instead.

Fig. 22 illustrates MD simulations for three representative cases of Ar_{349} cluster impacts with energy of 50 keV on Si surfaces. A central cluster impact on a hill (Fig. 22(a)) shows that the material of the hill is efficiently removed and a crater is formed. A side-impact on a hill (Fig. 22(b)) tends to diffuse the material into a valley. A valley-impact (Fig. 22(c)) shows a much lower sputtering yield. Therefore, the material of the hills will fill into the valleys and the surface which was initially rough, will become smoothed. Furthermore, the material of both areas, that on the hills and that moved to the valleys, will subsequently be removed by the continuation of the cluster ion bombardment.

The driving force for the smoothing mechanism can be thought of as a high non-equilibrium surface diffusivity of target atoms in the rim of the crater. Simulation results have shown that if the surface diffusion term is omitted from models of the surface dynamics, the surface becomes rougher for both types of cluster impacts, normal and oblique [44].

The sputtering characteristics of cluster ions depend strongly upon the type of the cluster–surface interaction process involved. It is quite useful to distinguish the characteristics as being related to “physical sputtering” or to “chemical sputtering”. Physical sputtering at normal cluster beam incidence, for example in the case of bombardment of a SiC surface by Ar clusters, causes significant smoothing of the bombarded surface. Chemical sputtering, as in bombardment of a reactive substrate surface such as W by an SF_6 cluster beam, does not produce the same smoothing effect. The experimental details will be discussed in Section 4.2.

3.2. Shallow implantation

3.2.1. Range and damage characteristics

Fig. 23 shows MD results of 7 keV boron clusters having 1, 13 and 169 atoms at 385 fs after impact on a Si surface [13].

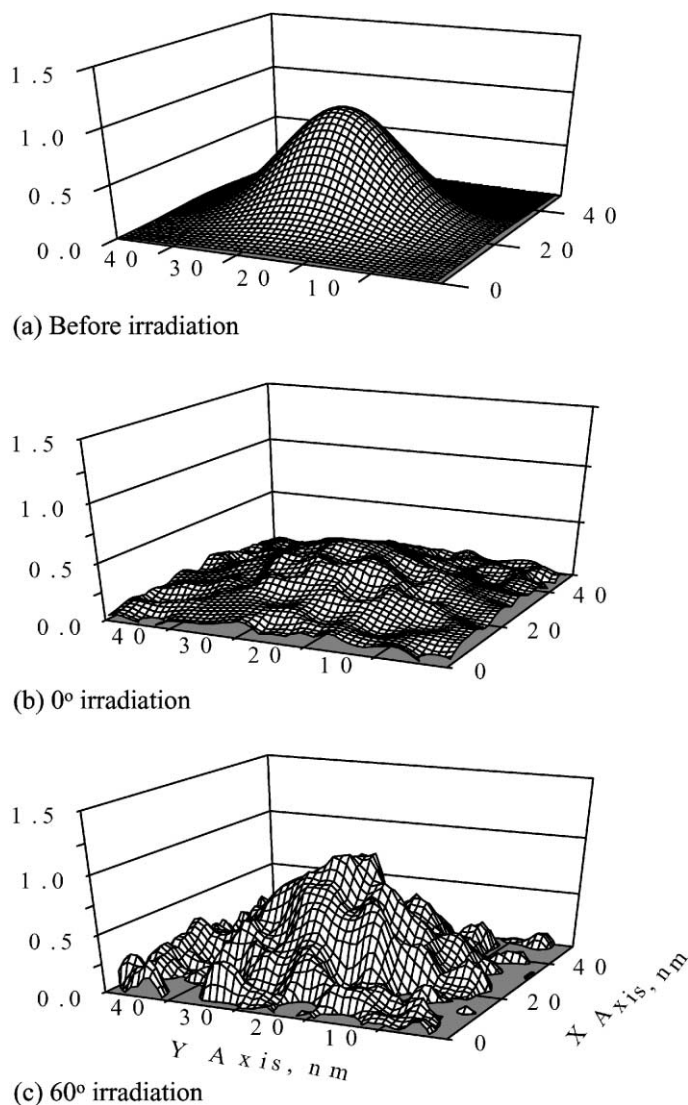


Fig. 21. MD simulation of cluster ion bombardment on a rough Si surface: initial surface geometry containing a single hill (a); after bombardment at 20 keV Ar_{1000} by a dose of 1×10^{13} ions/cm² at normal incidence (b), and at 60° off-normal incidence (c).

For the same energy per impinging atom, the implantation characteristics of monomer ions, small cluster ions and large cluster ions are very different. Fig. 23(a) shows the typical monomer ion implantation effect. A collision cascade is created which causes dislodgment of atoms deep under the surface. The damage appears to be elongated like a string extending below the penetration point. The small cluster with 13 atoms (Fig. 23(b)) collapses on impact with the surface, and the damage created exhibits features different from those associated with monomer implantation: the damage zone resembles a triangle, with a broader base and a shorter depth than the ‘string’ appearance of the monomer. In the case of the 169 atom cluster, Fig. 23(c), part of the cluster remains together as a unit on impact, while only a few isolated atoms break off and generate collision cascades. The penetration is shallower for these cascades, due to the lower energy per atom. In this case, the cluster itself remains essentially intact during impact and a hemispherical “shell of damage” forms around

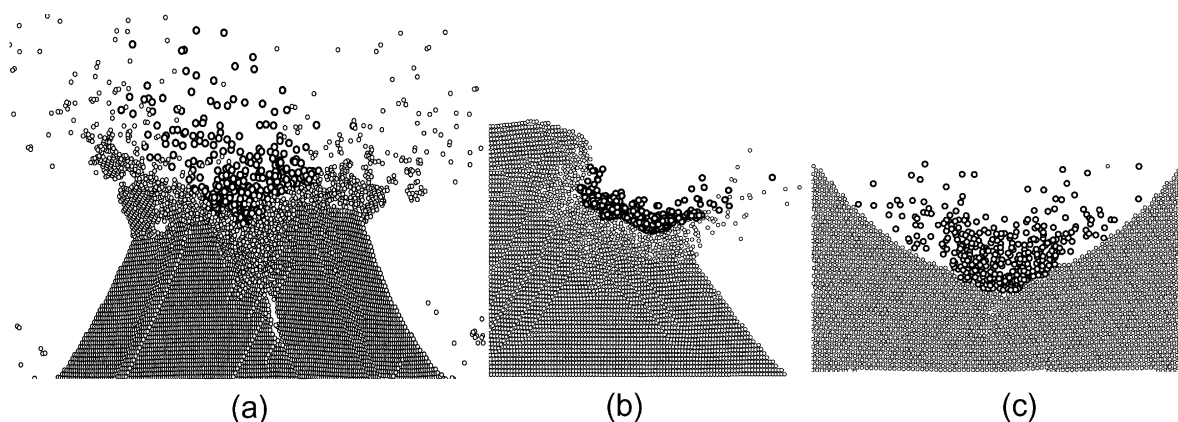


Fig. 22. Two-dimensional MD simulations of Ar_{349} cluster impacts on representative Si substrate surfaces at 50 keV on the top of the hill (a), on the right side (b), and on a valley between two neighboring hills (c). All images correspond to 890 fs after the beginning of the cluster–surface collision.

the cluster as it stops. There is still a possibility of channeling, as the acceptance angle for axial and planar channeling increases as atom energy decreases for small clusters, but the channeling observed in the simulations decreases with increasing cluster size, as expected.

As illustrated in Fig. 24, the 169 atom cluster also produces a shallower distribution of lattice damage. The number of displaced atoms in layers of Si has been calculated from the MD simulations shown in Fig. 23. The peak damage density was found to have doubled and the profile was only about one-fourth as deep as that of the B_{13} cluster. The number of displaced atoms is equal to the number of Si atoms in the region, implying complete amorphization of the Si surface layers to a depth of 5 nm. From the sharp drop-off of this profile, it is probable that there will be different annealing behavior if large clusters are used for implantation. With little damage and few interstitials in the layer underneath the implantation-induced amorphous layer, there should be a smaller driving force for transient enhanced diffusion (TED).

In Fig. 25, a B atom implanted at 230 eV is compared to a B_{13} cluster, where each atom has 230 eV when the total ion energy is divided among the constituent atoms. The profiles are seen to be

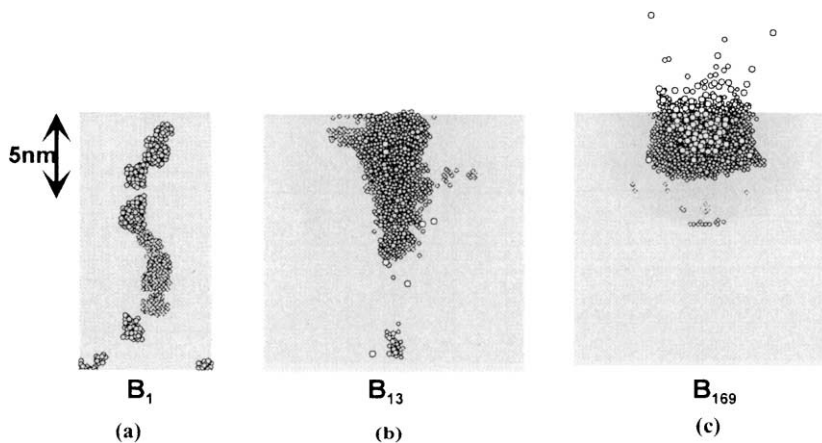


Fig. 23. MD simulation of monomer, 13 and 169 boron cluster impacts on crystalline Si, all at 7 keV acceleration energy after an elapsed time of 385 fs.

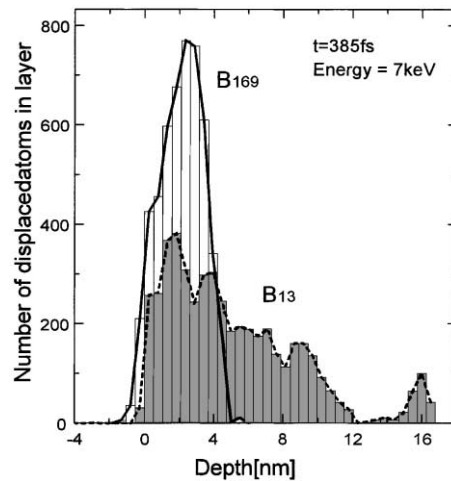


Fig. 24. Simulated displaced Si atom distribution in Si implanted with 7 keV B_{169} or B_{13} clusters after 385 fs.

almost identical. In B_{13} implantation, the cluster dissociates on impact, and the stopping behavior of each of the constituent atoms resembles that of a 230 eV monomer atom. The thirteen atom cluster behaves more like a monomer than like a large cluster.

3.2.2. Annealing effects

Differences in annealing behavior between cluster or monomer ion implantation have been studied by computer simulation of implantation by B and B_{10} with subsequent rapid thermal annealing (RTA). For this simulation a combination of two methods, MD and Monte Carlo was used, because the annealing process takes seconds and is therefore inaccessible for MD simulation [43]. A summary of the results is shown in Fig. 26.

After obtaining the initial positions of implanted B atoms and Si substrate atoms by MD simulation of implantation of B_{10} and 10 single B ions, the as-implanted (MD) atomic positions were

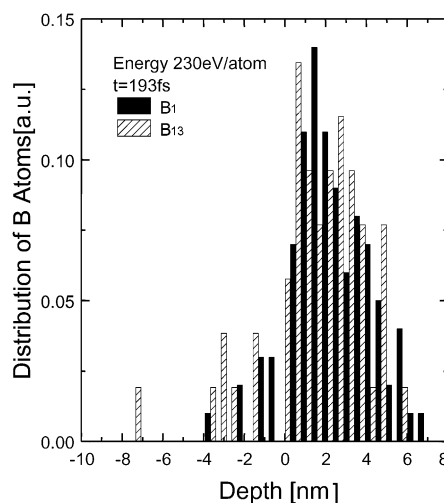


Fig. 25. Simulated dopant position in Si after 193 fs. B monomer implanted with 230 eV, B_{13} cluster implanted with 3 keV (230 eV per atom).

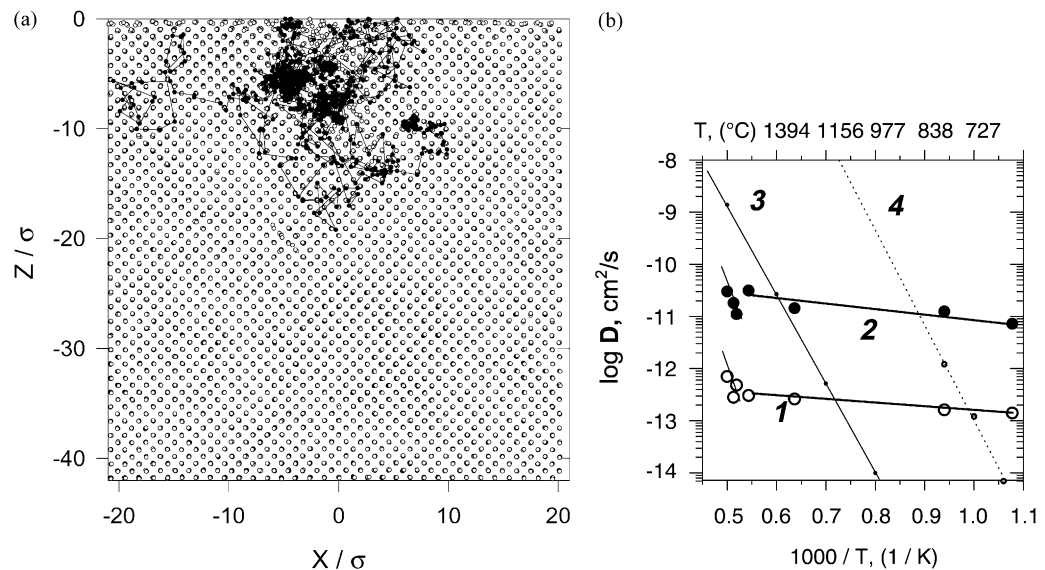


Fig. 26. (a) MMC simulation of B trajectories during RTA after cluster implantation; (b) B and Si diffusion coefficients obtained with MC simulation for 2.5 and 5 keV B_{10} implantation into Si: lines 1 and 2 show the diffusion coefficients obtained in this simulation: 1 — for Si atoms (open symbols), 2 — for B atoms (filled symbols). Line 3 is experimental data for B diffusivity (from [48]) and line 4 — experimental data for Si interstitials obtained for boron TED (from [49]).

transferred to a metropolis Monte Carlo (MMC) code to simulate the RTA process. The trajectories computed for the implanted B atoms during the annealing process are shown in Fig. 26(a). The B atoms from the B_{10} implant diffuse only in lateral directions within the implantation-affected region and do not diffuse to the region deeper in the substrate, thereby leaving it undamaged. The use of the MMC method allowed B diffusion coefficients to be computed for the first time [43]. The B and Si diffusion coefficients shown in Fig. 26(b) (lines 1 and 2), were obtained for implantation of 2.5 and 5 keV B_{10} into Si at annealing temperatures from 100 to 2000 K. These results are compared with the experimental data for B atomic diffusion (equilibrium) [48] (line 3) and with the data for Si interstitials obtained from TED experiments with B multi-layers grown by MBE [49] (line 4). There are no experimental data for boron TED coefficients, but the Si self-diffusion coefficients obtained at the same implantation conditions should be at least of the order of the boron TED. Line 4 for the Si self-diffusion lies from one to three orders of magnitude higher than the B diffusion coefficient obtained by means of this simulation for the range of temperatures used in RTA, i.e. around 900°C and higher. Therefore, these MD/MMC results predict that the boron TED may be significantly suppressed. Other theoretical papers, either analytical or simulations, predict diffusion coefficients higher by as much as six orders of magnitude for the Si interstitials which are thought to be the main partner for a kick-out mechanism responsible for the rapid boron diffusion [49]. The simulation results show that a large area of the substrate is amorphized by the B cluster implantation. The implanted boron atoms are trapped within the amorphized area for the whole annealing time. The atomic movement of boron within the amorphized area is much easier than that for equilibrium diffusion and therefore the resulting diffusion coefficients are quite high. This fast B diffusion in Si has no relation with the TED because it occurs primarily in the x - y plane. From Fig. 26(b), the activation energy for this movement was roughly 0.2 eV, in agreement with the tight-binding diffusion theory [50]. These results suggest that cluster implantation can reduce TED and very shallow junction formation should be possible. Experimental results will be discussed in Section 5.

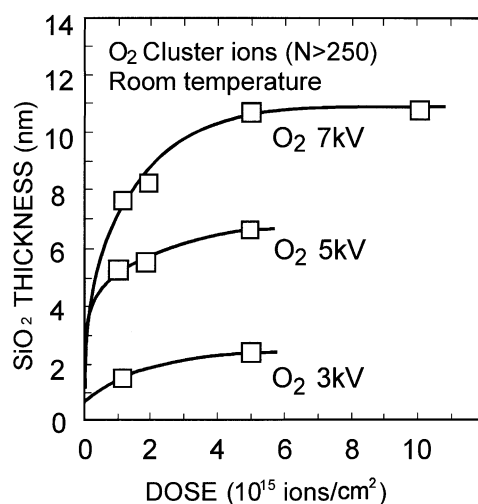


Fig. 27. Dose dependence of the thickness of SiO $_2$ films produced by (O $_2$) $_n$ (mean $n \sim 1000$), cluster ion beams for total cluster energies of 3, 5 and 7 keV.

3.3. Enhancement of surface chemical reactions

Cluster ion beams can be utilized for reactive growth of thin films at low temperatures. High transient energy densities produced by individual cluster impacts on a surface can significantly enhance the rates of chemical reactions on that surface without heating the substrate itself.

In order to evaluate chemical reactivity effects of gas cluster ions, oxidation of Si by O $_2$ cluster ion bombardment was investigated. The results of a low-temperature oxidation experiment using 7, 5, and 3 keV (O $_2$) $_n$ cluster ion bombardment, with $n > 250$ and average size 1000, are indicated in Fig. 27 [51]. This figure shows the dose dependence of the thickness of SiO $_2$ films formed at room temperature on silicon due to bombardment by the oxygen cluster ions. The thickness can be seen to have saturated at a dose above 5×10^{15} ions/cm 2 . SiO $_2$ films 11, 6.5, and 2.5 nm thick were formed by bombardment with 7, 5 and 3 keV O $_2$ cluster ions, respectively, each to a dose of 5×10^{15} ions/cm 2 .

Room-temperature oxidation of silicon by 40–200 eV O $_2$ monomer ion bombardment has been reported [51]. SiO $_2$ films 5 nm thick were formed due to 60 eV ion bombardment to a dose of 10^{18} ions/cm 2 . The expected thickness at a dose of 10^{19} ions/cm 2 was only 6.5 nm because of the slow oxidation rate. Thus, as shown in Fig. 27, it was found that much thicker SiO $_2$ films (11 nm) can be produced by O $_2$ cluster ion beams than by monomer O $_2$ ion beams (6 nm), even though the mean energy per atom in the cluster case was less than 10 eV (assuming a cluster size of approximately 1000 atoms). The diffusion length of the oxygen might be determined by the kinetic energy of the cluster. These results suggest that a new oxidation mechanism might be involved in cluster ion-induced oxidation.

4. Cluster ion beam sputtering

4.1. Physical sputtering

4.1.1. Physical sputtering yield

Sputtering by cluster ion beams involves high sputtering yields and strong surface smoothing effects. Fig. 28 shows an AFM image of an Au target which was irradiated by an Ar cluster ion beam

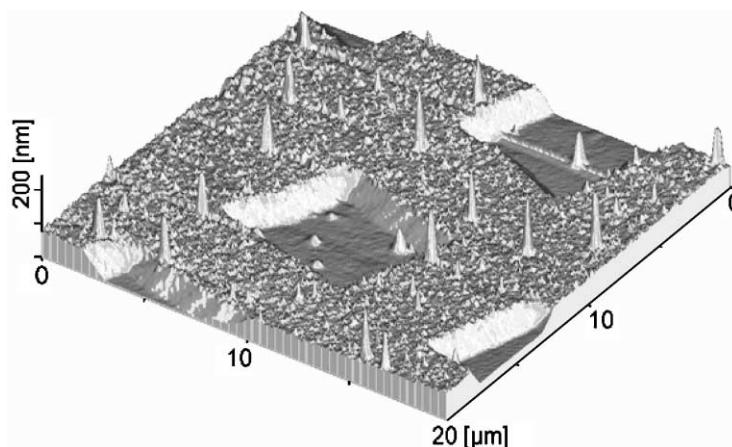


Fig. 28. AFM images of Au surface irradiated with 20 keV Ar cluster ion beams through an ultra-fine mesh at a dose of 1×10^{16} ions/cm².

through an ultra-fine mesh mask. The acceleration energy, cluster size and ion dose were 20 keV, 2000 atoms per cluster and 1×10^{16} ions/cm², respectively. Several square areas which are seen to be at lower height were the regions irradiated by the Ar cluster ions. It can be seen that the bottom of the irradiated area became highly smoothed relative to the surface of the unprocessed area which was protected by the mask. The detailed data from these observations are discussed below.

Sputtering yields of Ar cluster ions in various materials have been obtained from the slopes of the linear experimental relationships between ion dose and sputter depth. Unless this linearity exists, the sputtering yields cannot be defined. Fig. 29 shows the ion dose dependence of sputter depth of various elements due to 20 keV Ar cluster ion beam bombardment [52]. Average cluster size was 2000 atoms per cluster. The target materials were films of Ag, Cu, Au, W, Zr and Ti deposited onto Si. The cluster ion dose was varied over a range from 8×10^{14} to 8×10^{15} ions/cm². Fairly good linearity of the dose dependence can be seen for the different materials.

Fig. 30 shows the sputtering yields of various materials due to 20 keV Ar cluster ions. To validate the experimental procedure, similarly measured sputtering yields for 20 keV Ar monomer ions were compared with known reference values [53]. The sputtering yields showed periodic changes related to the atomic numbers of the target materials. This tendency originates because

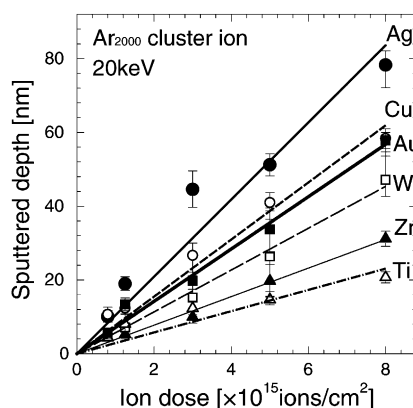


Fig. 29. Ion dose dependence of sputtered depth with 20 keV Ar cluster ions for various materials.

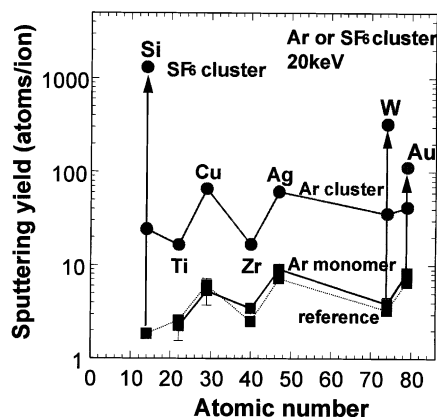


Fig. 30. Sputtering yields of various materials with 20 keV Ar monomer ions and Ar cluster ions.

sputtering yield is inversely proportional to the binding energy of the atoms. Consequently, sputtering yields of the atoms in the Ib group (Cu, Ag and Au) are higher than those in the IVa group (Ti, Zr) or VIa group (W). This can be explained by the fact that the binding energy becomes low whenever the d shell is filled by electrons, which in turn results in an increase of the sputtering yield [54,55]. In these experiments, the measured sputtering yields of monomer ions showed good agreement with the reported values, which validated the experimental method.

Compared with the sputtering yields measured with Ar monomer ions at the same acceleration energy, sputtering yields obtained with Ar cluster ions were approximately one order of magnitude higher. For example, the sputtering yield of Cu with Ar cluster ions (65.5 atoms per ion) was 12 times higher than that with Ar monomer ions (5.3 atoms per ion). Moreover, the sputtering yield with Ar cluster ions followed the same periodic changes as those observed with monomer ions. The sputtering yields of other materials with Ar cluster ions can be roughly estimated from the reference values for Ar monomer ions.

Fig. 31 shows the dependence of the sputtering yields of Cu and Ag upon the acceleration energy of Ar cluster ions. The ion dose for these experiments was 5×10^{15} ions/cm² and the average cluster size was 2000 atoms per cluster. The acceleration energy ranged from 10 to 25 keV. The

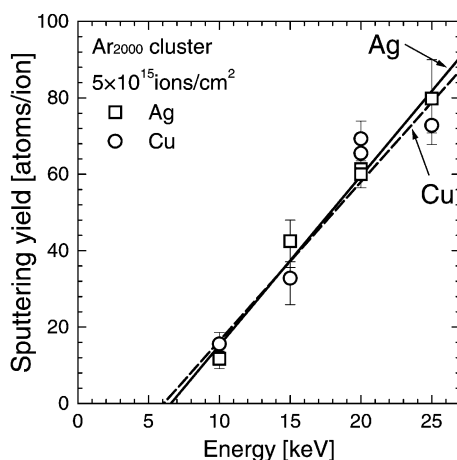


Fig. 31. Energy dependence of the sputtering yield with Ar cluster ions at the dose shown.

sputtering yields increased almost linearly with acceleration energy over this range, and there was a threshold energy for sputtering at 6 keV. In the case of monomer ions, the sputtering yields increased linearly over the range from about 50 eV to 1 keV, and then gradually saturated due to the energy deposition in the deeper region [56]. The threshold energies for sputtering of Cu and Ag by Ar monomer ions are 17 and 15 eV, respectively [57]. In the case of the cluster ions, because cluster size was 2000 atoms per cluster, at the sputtering threshold energy of 6 keV, each cluster atom had a kinetic energy of approximately 3 eV. This measured threshold energy is one-fifth of the value reported for monomer ions. Sputtering by monomer ions is caused by the knock-on cascade which is generated inside of the target and develops towards the surface. This process generates large numbers of defects in the target as the energy of the impinging ion is absorbed. In the case of cluster ions, collisions near the surface are dominant and all the energy is efficiently deposited onto the surface as was suggested in Fig. 17. Thus, the target surface atoms can be sputtered at an energy per cluster atom lower than the threshold value for sputtering by monomer ions.

4.1.2. Incident beam angle dependence

When any projectile ion impacts upon a target at an oblique angle of incidence, the resulting angular distribution of sputtered atoms can be described in terms of two physical mechanisms: cascade collision and direct ejection. With increasing incidence angle, the influence of direct ejection becomes increasingly dominant and ultimately, at glancing incidence, cascade collisions are not observed. In the case of cluster ions, there are few experimental measurements of the incidence angle dependence of the angular distributions of sputtered atoms. As was illustrated in Fig. 1 of Section 1, when a cluster impacts upon a solid surface, the impinging energy of the cluster is deposited into a local area, resulting in the formation of a crater characterized by a central depression surrounded by a protruding rim. Since this characteristic crater formation does not occur in the case of monomer ion impact, a different sputtering mechanism and different angular distribution are associated with the cluster ion bombardment.

Qualitative information on the angular dependence of the sputtering yields due to monomer ions was obtained first by Fetz [58] in the 1940s, and later by Wehner in the early 1950s [59]. For single ion bombardment in the keV energy region, it was found that the angular dependence of the sputtering yield $\phi(\theta)$ was given by $\phi(\theta)/\phi(0^\circ) = 1/\cos \theta$ where θ is the angle from the surface normal. Sigmund, however, showed that $1/\cos \theta$ dependence should be expected only for large m_2/m_1 (where m_1 is mass of target atom, m_2 is mass of ion), and that it increases in proportion to $\cos^{-f} \theta$ ($f = 1$ and 2) [60]. In both cases, the sputtering yield reaches a maximum at an angle of 60–80°. When the incidence angle changes from normal to oblique, the collision frequency in the near surface region becomes high and all the energy is deposited into this region, resulting in high sputtering yields. With a further increase of the incidence angle, the sputtering yield suddenly decreases. This occurs because, at these high angles of incidence, ions are predominantly reflected from the surface and are not able to transfer their kinetic energies effectively to atoms of the target.

The energy loss and deposition processes associated with cluster ions are completely different from those associated with monomer ions. These effects can be observed in the angular dependence of the sputtering yields. Fig. 32 shows the incidence angle dependence of sputtering yields due to 20 keV Ar cluster ions. The targets were Cu and Ag films. The ion dose and the average cluster size were 5×10^{15} ions/cm² and 2000 atoms per cluster, respectively. The measured sputtering yields $\phi(\theta)$ were normalized to those at normal incidence, $\phi(0^\circ)$. The angular dependence resulting with monomer ions was plotted as a function of $1/\cos \theta$. A difference is clearly evident in the incidence angle dependence of the sputtering yields of the cluster ions relative those of the monomer ions. This effect can be explained by the linear cascade collision theory [60,61].

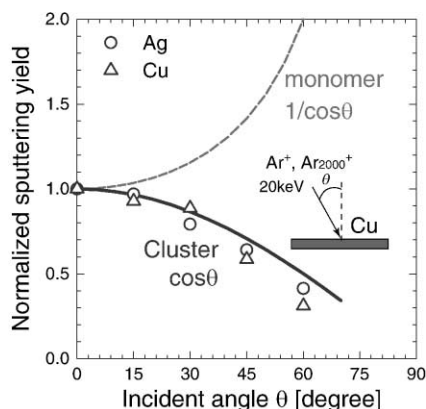


Fig. 32. Incident angle dependence of the sputtering yields of Cu and Ag with 20 keV Ar cluster ions.

In the case of both Cu and Ag targets, the normalized sputtering yields of 20 keV Ar cluster ions decreased in proportion to $\cos \theta$. When the incidence angle was 0° , the penetration was deepest, and most of the kinetic energy of the clusters could be transferred to the target atoms. In the case of oblique incidence, the energy carried by the cluster ions could be only partially transferred into the target because many atoms from the cluster were ejected or reflected from the surface with large kinetic energies. Since the kinetic energy deposited perpendicularly onto the target was proportional to $\cos \theta$, the sputtering yield followed this curve.

Not only the incidence angle dependence of the sputtering yields, but also the angular distributions of atoms sputtered by cluster ions were measured [62]. Sputtered materials were collected on Si substrates surrounding the target and these substrates were subsequently analyzed by Rutherford back-scattering spectroscopy (RBS) to determine atomic concentrations in the deposited layers. The sticking probability on the collector substrates was assumed to be unity. No difference in the measured distributions was observed when the silicon collector substrates were replaced by carbon collector substrates. Fig. 33 shows the experimental configuration. In the case of Ar cluster ions, polycrystalline Cu films were used as a sputter targets because the surface binding energy of Cu is relatively low and Cu consequently exhibits high sputtering yields. In addition, many previous reports concerning sputtering of Cu by Ar monomer ions are available for comparison with the sputtering results observed from cluster ions. Fig. 34 shows the angular distributions of Cu atoms sputtered at normal incidence by 20 keV Ar monomer ions and by 10 and 20 keV Ar cluster ions. The average cluster size and the ion dose were 2000 atoms per cluster and 1×10^{17} ions/cm², respectively. The results shown in Fig. 34 should be compared with the MD simulation results which were shown in Fig. 20.

It has been reported that the morphology of a target surface affects the angular distribution of material sputtered from the target [63]. The Cu film used as the sputter target in this study was initially polycrystalline with grains approximately 400 nm in diameter and 15 nm in height. This Cu surface became effectively fully smoothed by the Ar cluster ions after an ion dose of 3×10^{15} ions/cm², which was just a few percent of the total ion dose employed in the experiment. Therefore, the initial surface roughness in this case was considered to have had little influence on the measured angular distributions.

In the case of 20 keV Ar monomer ions, the measured angular distribution formed the circle shown in the center of Fig. 34. This circular distribution essentially followed the cosine law, which

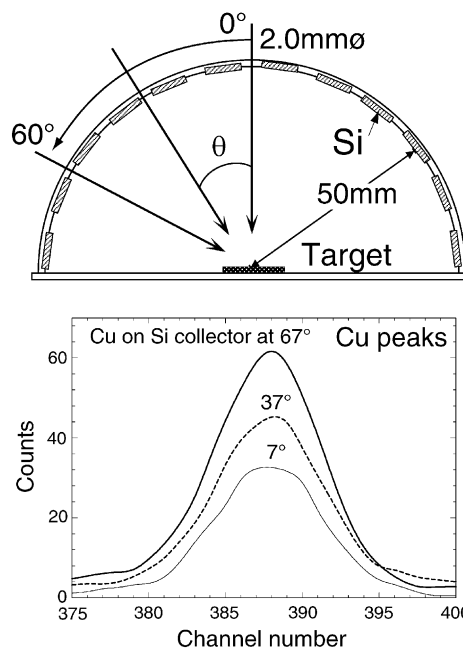


Fig. 33. Sample holder for the measurement of angular distribution of sputtered particles and the RBS spectra around Cu peak on Si collectors.

indicates isotropic ejection of atoms from the target surface. This result shows good agreement with the linear cascade collision theory. In contrast, the angular distribution due to the Ar cluster ions showed a shape completely different from the cosine distribution. With the reduction of incident energy to 10 keV, the angular distribution became even more flattened. It is interesting to note here that Sigmund [64] observed a similar sputtering yield enhancement with heavy monomer ions or molecular ions, an effect attributed to a dense cascade (spike) collision occurring under these conditions. In the case of cluster ions however, the observed effect is due to the quite different reasons discussed above.

As was described in Section 4.1.2, sputtering phenomena, including the penetration depth, density of deposited energy, damaged area, sputtering yield, and numerous other parameters, depend upon the angle of incidence of the bombarding ions. In cluster ion impact, incidence angle also has

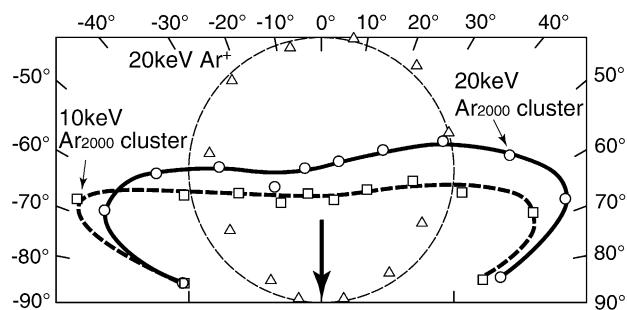


Fig. 34. Angular distribution of sputtered Cu atoms with 20 keV Ar monomer, 10 and 20 keV Ar₂₀₀₀ cluster ions at normal incidence.

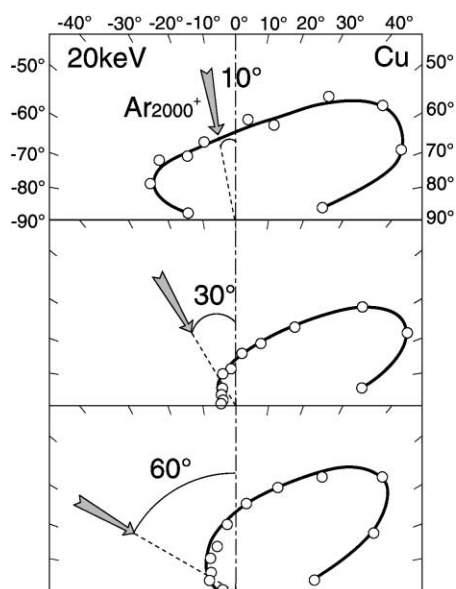


Fig. 35. Angular distribution of atoms sputtered by Ar cluster ions (average size: 2000 atoms per cluster) at several incident angles. Acceleration energy: 20 keV.

strong, but often quite different, influence. Fig. 35 shows the angular distribution of Cu atoms sputtered by Ar cluster ions incident at oblique angles. The angle of incidence ranged from 10 to 60° and the acceleration energy was fixed at 20 keV. The average cluster size was 2000 atoms per cluster. Even at an oblique incidence angle of only 10°, the majority of the sputtered particles were distributed to the forward direction. No significant change in the angular distribution was found when the angle of incidence was changed from 10 to 60°.

The results discussed above indicate that the angular distribution of material sputtered by cluster ions is very sensitive to incidence angle only for angles which are near to normal. When a cluster impacts upon a target at normal incidence, the transferred energy is deposited isotropically. However, localization of energy density occurs during an oblique impact, and this energy is preferentially released from one side. In the case of monomer ions, energetic ions penetrate deep into the target and induce random collision cascades. Consequently, for monomers, there are no significant changes in angular distribution of sputtered material with change of the ion incidence direction at angles near 0°. The large change in the angular distribution of ejected material for incidence angles near normal is another feature which is unique to cluster ion bombardment.

In addition to the macroscopic measurements of sputtered atom distributions described above, microscopic observations of single traces caused by cluster ion impacts were performed using a STM. Fig. 36 shows STM images of a highly oriented pyrolytic graphite (HOPG) surface irradiated with 150 keV Ar cluster ions at incidence angles of 0 and 60°. The Ar cluster size was 100 atoms per cluster as selected with a Wien filter. The scan area of the STM was 50 nm × 50 nm. In the case of normal incidence shown in Fig. 36(a), a doughnut-shaped crater was formed and the ejected atoms from the crater formed a mound around the rim of the crater. At normal incidence, a highly symmetric crater was observed. However, at an incidence angle of 60°, the shape of the crater, as shown in Fig. 36(b), was asymmetric and the ejected atoms formed a large mound in the direction forward from the penetration direction. These microscopic images of a single cluster ion impact showed good agreement with the angular distribution of the sputtered atoms shown in Fig. 35.

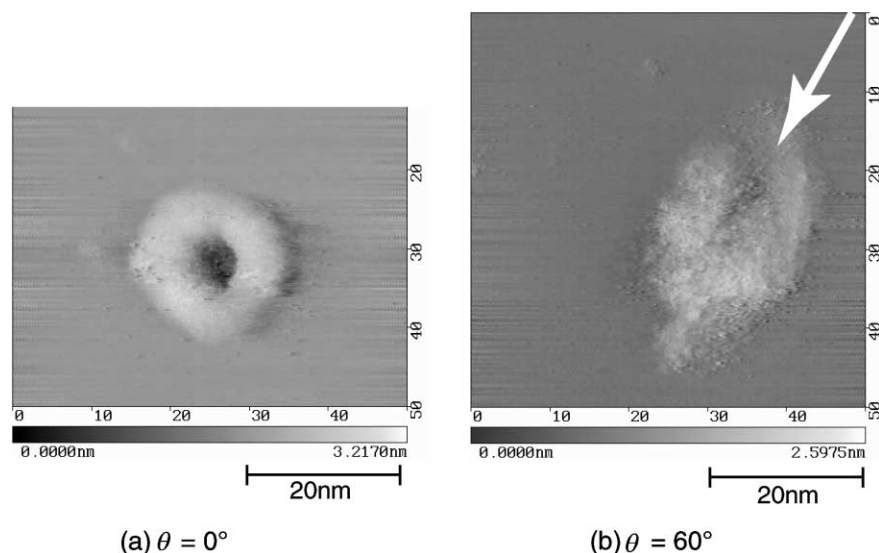


Fig. 36. STM images of Ar_{100} cluster ion impact on HOPG surface at oblique incidence at 150 keV acceleration energy.

4.2. Reactive sputtering

4.2.1. Reactive sputtering yield

When a reactive gas is used as the cluster source gas, enhancement of sputtering effects due to chemical reactions is expected. Because the energy per atom in a cluster is equal to the total energy of the cluster divided by the cluster size, radiation damage induced by reactive cluster ion bombardment can be minimal. For example, in the case of 20 keV cluster ions comprised of 2000 SF_6 molecules, which are found to cause strong reactive sputtering of Si, each SF_6 molecule has an energy of only 10 eV. Because the displacement energy of Si is between 12 and 15 eV [48], this energy per SF_6 molecule is less than the energy needed to physically displace Si atoms. Therefore, low damage etching of a Si substrate is believed to occur.

Further, since the number of atoms transported by a reactive cluster is much larger than the number of charges, a reactive cluster ion beam process does not cause the surface charging which is usually a serious problem in plasma processes. Moreover, in the cluster beam process, the beam impact upon the target is directional. As a result, anisotropic etching is achieved and there is no dependence of the etching rate on etching pattern as is typically caused by radicals in a plasma.

As described in Section 4.1.1, the sputtering yields with Ar cluster ions for various materials are one or two orders of magnitude higher than those of Ar monomer ions at the same energies. However, in the case of reactive gas species, additional enhancement of sputtering yields due to the chemical reactions can be expected. Fig. 37 shows sputtering yields of Si, SiC, W and Au due to Ar monomer ions, Ar cluster ions and SF_6 cluster ions, all at energies of 20 keV. The average size of the Ar and SF_6 cluster ions was 2000 atoms. In comparing sputtering of W and Au, which have similar atomic masses, the sputtering yield of Au due to Ar cluster ions (42 atoms per ion) was only slightly higher than that of W (35 atoms per ion). The same tendency was found with Ar monomer ions. On the other hand, the sputtering yield of W due to SF_6 cluster ions was 320 atoms per ion, which was almost three times as high as that of Au (112 atoms per ion) due to the same SF_6 cluster ions. This was because tungsten atoms reacted with fluorine dissociated from SF_6 clusters and, as a

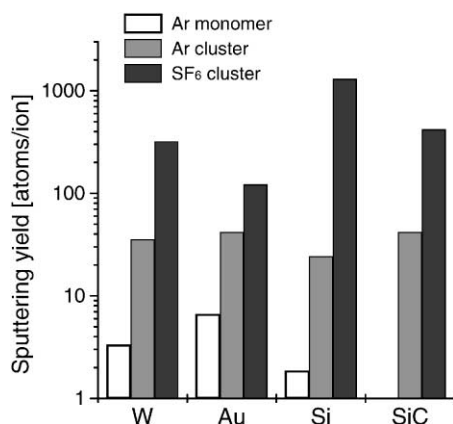


Fig. 37. Reactive sputtering yield with SF₆ cluster ions for various materials at 20 keV acceleration energy.

result, the sputtering yield was enhanced by the production of volatile WF_x materials. Enhancement of the sputtering yields with SF₆ cluster ions was also observed in the case of compound materials such as SiC.

Similarly, the sputtering yield of Si with Ar cluster ions (24 atoms per ion) was enhanced 55 times by chemical reaction with SF₆ cluster ions (1300 atoms per ion). As the average size of the SF₆ clusters was about 2000 molecules per cluster, the SF₆ cluster ions showed high reaction probability with Si. A question can be posed as to why an SF₆ cluster ion shows such a high reaction probability with Si even though an SF₆ molecule is stable at room temperature. In the etching process, the following sequence of events is believed to occur: (a) absorption of the etchant on the surface, (b) formation of a volatile product and (c) evaporation or ejection of the product from the surface. It has been reported that chemical reactions between SF₆ molecules and Si are stimulated by energetic Ar monomer ion bombardments [65]. This has been explained to be a result of SF₆ molecules being dissociated by the energetic ion bombardment and the released fluorine atoms then being able to react with Si atoms.

We suggest that the fragmentation of a cluster and the dissociation of an SF₆ molecule both occur simultaneously when an SF₆ cluster ion collides with a Si or W surface. Consequently, SiF_x or WF_x, which are volatile compounds, are produced. SiF_x and WF_x are physically sputtered by energetic ions or are thermally evaporated into the vacuum. Thus, the sputtering yield increases as a consequence of the production of volatile compounds promoted by SF₆ cluster ion bombardment.

To confirm that the etching yield is enhanced by the production of volatile materials such as SiF_x, mass spectra of particles generated during SF₆ cluster ion irradiation were measured using a residual gas analyzer (RGA). Fig. 38 shows the mass spectra observed when a Si substrate was irradiated with a 25 keV SF₆ cluster ion beam. The average cluster size was 2000 molecules per cluster. An intermediate shutter was installed in front of the Si target and the mass spectra were acquired with the shutter opened and closed. As seen in Fig. 38, a peak at the atomic mass 85 showed a marked increase on opening of the shutter. This peak is attributed to SiF₃⁺. It is well known that SiF₄ undergoes fragmentation to SiF₃⁺ due to ionization. As ionization within the RGA was performed by electron bombardment, SiF₄ molecules were transformed into SiF_n⁺ fragments ($n = 1-4$), with SiF₃⁺ having the highest intensity. Thus, the existence of an SiF₃ peak is an indication of the presence of SiF₄ molecules. A marked increase of SiF₄ is evidence for chemical reaction between Si and fluorine.

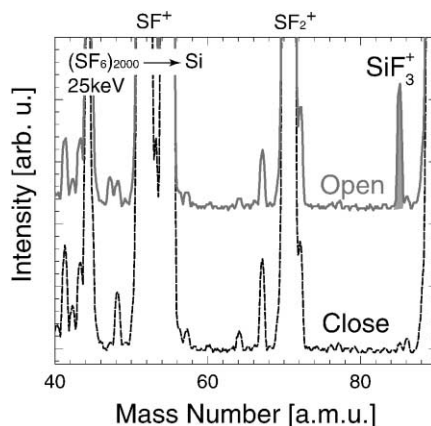


Fig. 38. Etching products during 25 keV SF_6 cluster ion irradiation on Si as observed by QMS. The average cluster size was 2000 atoms per cluster.

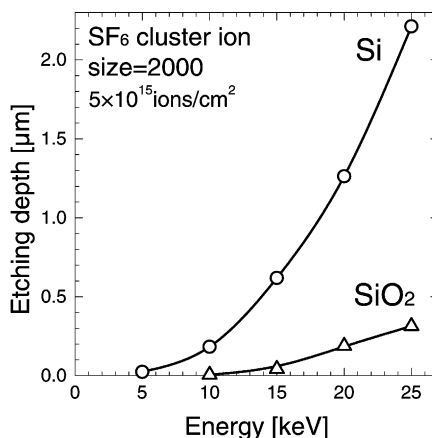


Fig. 39. Energy dependence of etching depth of Si and SiO_2 with SF_6 cluster ions at ion dose of 5×10^{15} ions/cm².

Like SF_6 cluster ions, O_2 cluster ions also produce reactive sputtering of diamond and graphite. Fig. 39 shows the energy dependence of the etching depth of Si and SiO_2 by SF_6 cluster ions. The SF_6 cluster size and the ion dose were 2000 molecules per ion and 5×10^{15} ions/cm², respectively. The target was held at room temperature. In the case of Ar cluster ions, the sputtering yield increased linearly with acceleration energy as shown in Fig. 31. In addition, a threshold energy for physical sputtering was found at 6 keV. In the case of SF_6 cluster ions, the etching depth of Si and SiO_2 increased exponentially with acceleration energy. When the acceleration energy and the ion dose were 25 keV and 5×10^{15} ions/cm², respectively, the etching depth of the Si was 2.2 μm . Even when the acceleration energy was 5 keV, which is lower than the threshold energy for physical sputtering, Si was etched to a depth of 30 nm by the SF_6 cluster ions. In this case, the energy per molecule was 2.5 eV, which lies between the activation energy of chemical reactions and the displacement energy of crystalline Si atoms. Chemical reaction between Si and fluorine was the dominant etching mechanism at low energies.

Selectivity arises from the volatility of the reaction products and the difference of the binding energies of the materials. The selectivity with Ar cluster ions is only defined by the surface binding

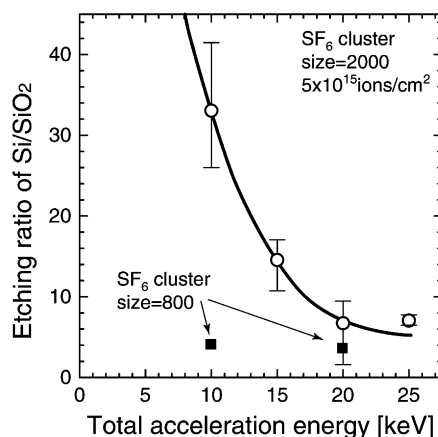


Fig. 40. Energy dependence of the etching ratio of Si to SiO₂ for the cluster sizes shown.

energy of the elements, resulting in the low selectivity. Fig. 40 shows the energy dependence of the etching ratio of Si to SiO₂ with SF₆ cluster ions. With decreasing acceleration energy, the etching ratio increased markedly below 15 keV. The etching ratios at acceleration energies of 25 and 10 keV were 7 and 33, respectively. In plasma etching processes, the etching ratio of Si to SiO₂ has been reported to be in the range of 10–50 [66]. It should be noted that the energy of the cluster ions was in the keV regime, and an increase of the selectivity was usually found below 1 keV in the case of monomer ions. When the acceleration energy was 5 keV, Si was etched to depth of 20–30 nm, but the etch depth in SiO₂ was less than the detection level of the surface profiler. This means that the etching ratio was extremely high, and chemical etching was the dominant process at 5 keV.

In contrast, the etching ratio with high-energy SF₆ cluster ions became low because not only the Si, but also the SiO₂, was physically sputtered by SF₆ cluster ions. The etching ratios produced by small cluster ions are thought to be lower than those of larger cluster ions. In Fig. 40, the etching ratios of Si to SiO₂ for smaller cluster sizes are also plotted. It should be noticed that the extraction voltage was set higher ($V_{\text{ext}} = 500$ V) than usual in order to extract smaller size cluster ions and this caused mixing of some fraction of monomer ions into the cluster ion beam. The average size of SF₆ cluster ions in these extraction conditions was 800 molecules per ion. As shown, there was no dependence of the etching ratio on the acceleration energy because physical sputtering became dominant in this size range. These results indicate that the etching ratio with cluster ion beam can be controlled by the cluster size as well as by the total acceleration energy. This method however is limited by the low resolution of available mass filtering.

Anisotropic etching using reactive cluster ion beams has been confirmed by observations of the etching pattern profiles [8]. Fig. 41 shows a scanning electron microscope (SEM) image of a Si(1 0 0) substrate etched by 20 keV SF₆ cluster ions at normal incidence. The Si surface was covered with a patterned SiO₂ mask 700 nm thick having a 0.5 μm diameter opening. The ion dose and the average cluster size were 1×10^{15} ions/cm² and 2000 molecules per atom. The substrate was held at room temperature. The result shows that etching by the SF₆ cluster ion beam is anisotropic and etching under the SiO₂ mask (undercutting) did not occur. If the direction of the ion trajectories was dispersive or curved, as would be caused by charge build-up on the patterned mask, the side walls of the hole would have been etched, and this would have resulted in curvature near the bottom region of the wall. Because only energetic cluster ions penetrated into the hole, the trajectories were almost perpendicular to the hole opening. In addition, charging up of the mask was less significant in the cluster ion beam process because the mass-to-charge ratio of the clusters was quite high.

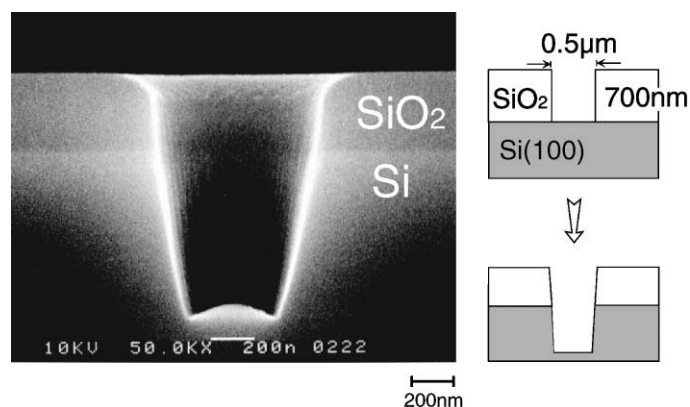


Fig. 41. Etching of Si with 0.5 μm diameter SiO_2 mask.

In Fig. 41, a tapered structure was observed on the etched side walls. This structure originated from the spreading of the SiO_2 mask caused by cluster ion bombardment. This spreading of the SiO_2 mask could have been avoided by using a multi-layer resist mask which would have been more durable against the ion bombardment [67]. It is very difficult to achieve similar anisotropic etching with fluorine-based plasmas at room temperature because of the fluorine radicals in a plasma. To avoid isotropic etching with fluorine radicals, additional treatments such as cooling of the substrate or protective formations for the side walls have been proposed [68]. In the case of the reactive cluster ion beam, anisotropic etching is possible without such treatments.

In the experiment discussed above, the cluster ion current density was $2 \mu\text{A}/\text{cm}^2$ at acceleration energy of 20 keV. From the etching depth of the Si substrate, the etching rate of Si by the SF_6 cluster ion beam was $0.2 \mu\text{m}/\text{min}$. In order to apply a reactive GCIB process in industry, a much higher cluster ion current density would be required.

4.2.2. Angular dependence of sputtered atoms

As sputtering effects due to cluster ions occur near the surface region, the angular distribution of the sputtered material is affected by the surface state of the target. When the projectile ion reacts with the target atoms, compound products are generated on the surface as a consequence of the chemical reactions, and these increase or decrease the sputtering yields. The angular distributions of sputtered atoms are expected to be strongly affected by these chemical reactions [69]. The angular distributions of atoms sputtered by SF_6 cluster ion beams have been measured on both reactive and non-reactive targets. Tungsten and gold films were used as reactive and non-reactive targets, respectively. The Au target suffered only physical sputtering effects from SF_6 cluster ions, whereas SF_6 reacted with tungsten and gave rise to both physical and reactive sputtering effects.

The atomic masses of gold (197) and tungsten (184) are almost the same. The mass ratio of an impinging ion relative to the target atoms is significant in physical sputtering phenomena. Therefore, in the case of Au and W targets, the effects of chemical reactivity on the angular distributions can be compared without considering the mass ratio of primary ion to target atom. Fig. 42 shows the angular distribution of the Au atoms sputtered by SF_6 cluster ions. The acceleration energy of the cluster ions was 20 keV and the incidence angles were 0 and 10° . The angular distribution of sputtered Au due to SF_6 cluster ion sputtering at normal incidence showed a flattened profile, which was the same as that of Cu due to Ar cluster ions. In addition, sputtered Au atoms were distributed in the forward direction at an incidence angle of 10° . Since no chemical reaction occurred on the Au surface with

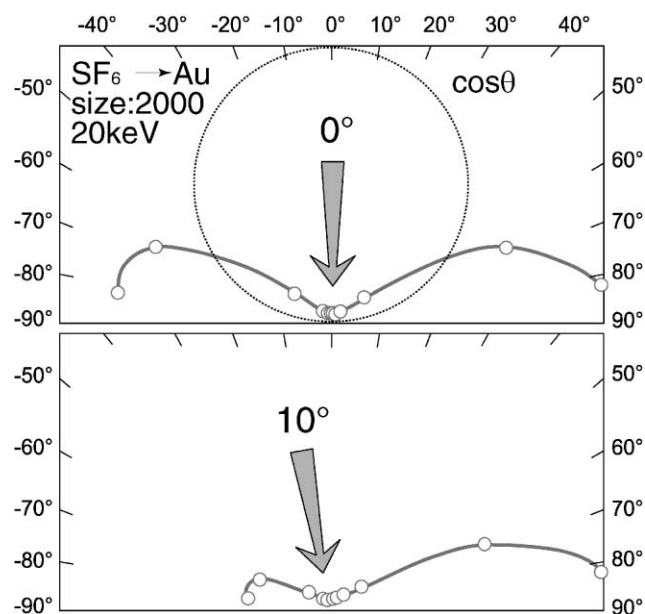


Fig. 42. Angular distribution of sputtered Au atoms with 20 keV SF_6 cluster ions at incident angles 0 and 10° .

SF_6 cluster ions, these angular distributions were induced only by physical sputtering. From these results, it appears that the lateral sputtering at normal incidence and the marked change of angular distribution at near normal incidence are inherent to physical sputtering due to any cluster ion.

Fig. 43 shows the angular distribution of W sputtered by SF_6 cluster ions. In contrast to the situation with Au, the distribution with SF_6 cluster ions almost followed the cosine law at normal

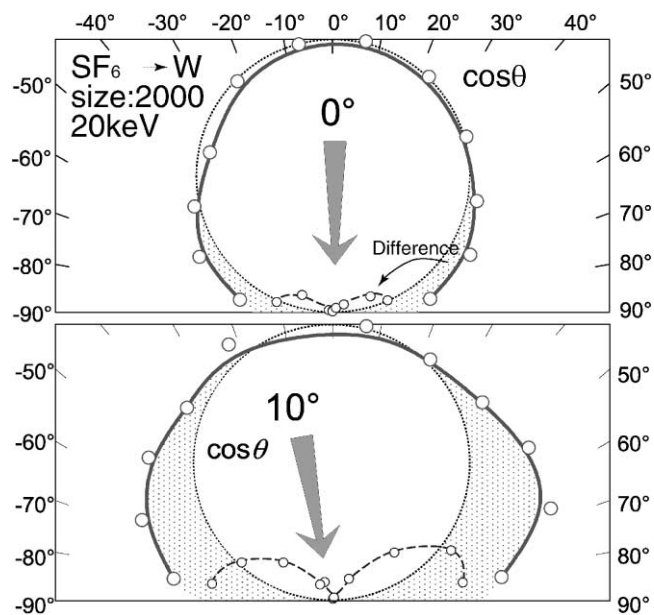


Fig. 43. Angular distribution of sputtered W atoms with SF_6 cluster ions at incident angle of 0 and 10° . The difference of the yield between the as-measured and the cosine distribution is plotted by the dotted line in the center.

incidence. As discussed in Section 4.2.1, tungsten reacted with fluorine and produced reaction products such as WF_6 , a volatile material which was then thermally evaporated from the surface isotropically. As a result, the angular distribution followed a cosine law. Even at an oblique impact, the angular distribution was almost isotropic. This was completely different from the behavior of Ar cluster ions on a Cu surface, or that of SF_6 cluster ions on an Au surface at oblique impact, which showed asymmetric distribution to the forward side of the incident direction.

However, the number of sputtered particles at high angles (near to the surface) was larger than would be expected from the cosine law (shown as a circle). The difference of the yield between the as-measured and the cosine distribution were also plotted by the dotted line in Fig. 43. This additional yield showed an under-cosine distribution which was similar to that of Cu with Ar cluster ions. This could be attributed to the physical sputtering effects of SF_6 cluster ions on W. Chemical reaction was a dominant etching process at this energy level. However, the contribution from physical sputtering with reactive cluster ions showed the same distribution as with the Ar cluster ions. Therefore, both physical and chemical sputtering effects were present in the SF_6 cluster impact, and the angular distribution became isotropic when chemical reactions were dominant. It should be mentioned that surface smoothing effects are also strongly influenced by the angular distributions of the sputtered atoms. This will be discussed in Section 4.3 below.

4.3. Surface smoothing

4.3.1. Surface smoothing with Ar cluster ions

In order to study the difference in surface smoothing effects caused by monomer and cluster ions, surface morphologies of Cu targets were observed using an AFM. Cu films were deposited onto Si substrates by sputtering and were irradiated with Ar monomer and cluster ion beams at normal incidence. The targets were at ambient temperature. The scan area of the AFM was either $1\ \mu\text{m} \times 1\ \mu\text{m}$ or $10\ \mu\text{m} \times 10\ \mu\text{m}$. Fig. 44(a)–(c) show AFM images of Cu surfaces irradiated with 20 keV Ar monomer and Ar cluster ion beams. The average cluster size was 2000 atoms per cluster. The ion doses were 1.2×10^{16} ions/cm² with Ar monomer ions and 8.0×10^{15} ions/cm² with Ar cluster ions. The initial Cu surface (Fig. 44(a)) had many grains 400 nm wide and 15 nm in height, and the average roughness was 5.8 nm. Following Ar monomer ion bombardment (Fig. 44(b)), there were still many grains on the surface and small hillocks caused by the energetic ion bombardment were observed. The average roughness of this surface was 4.9 nm, which means that the surface roughness was only slightly improved by the 20 keV Ar monomer ions at normal incidence.

When the Cu target was irradiated with Ar cluster ion beams (Fig. 44(c)), the average roughness was reduced to 1.3 nm, which was only a little more than one-fifth of the initial roughness. Considering that the cluster ion dose was only two thirds that of the monomer ions, the Cu surface was obviously smoothed more effectively by the Ar cluster ions than by the Ar monomer ions. In monomer ion sputtering, it has been reported that the anisotropy of the sputtering yield depends on the presence of facets or grain boundaries. From Fig. 44(c), no grains were observed on the surface and there seemed to be little dependence of sputtering yield with cluster ions on grain boundaries or facets. In the same way as in the case of Cu targets, other metals, semiconductors and insulator surfaces have been smoothed very effectively using cluster ions.

Fig. 45 shows the ion dose dependence of the average roughness of the Cu surfaces bombarded with 20 keV Ar cluster ion beams at normal incidence. The ion dose ranged from 8×10^{14} to 8×10^{15} ions/cm² and the average cluster size was 2000 atoms per cluster. In addition to the average roughness, AFM images at each ion dose are shown. As shown in Fig. 45, the average roughness decreased monotonically with increasing ion dose from the initial value of 6–1.3 nm at an ion dose

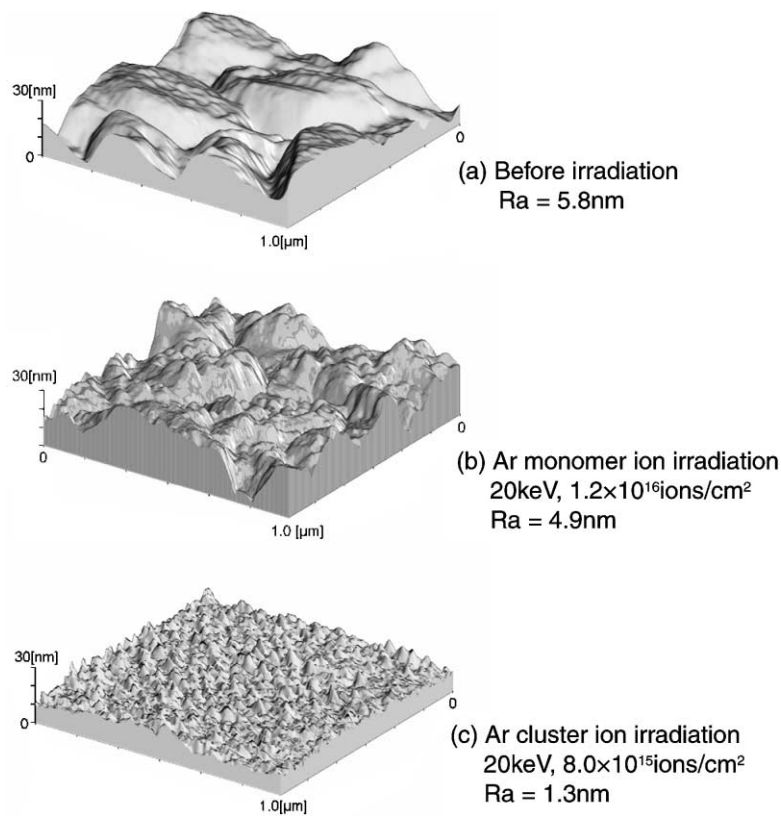


Fig. 44. AFM images of Cu surfaces irradiated with Ar monomer and Ar cluster ions at 20 keV total acceleration energy.

of 8×10^{15} ions/cm². In the case of monomer ion irradiation at normal incidence, the surface roughness became worse with ion dose due to erosion or bubble formation inside the target [70]. However, no roughening mechanism was observed with Ar cluster ion irradiation upon increasing dose. The average roughness of the Cu surface saturated at an ion dose above 3×10^{15} ions/cm².

Fig. 46 shows the relationship between the average roughness and the depth of Cu sputtered by Ar cluster ions. The open circles with a full curve refer to the average roughness caused by 20 keV Ar cluster ions shown in Fig. 45. The other data points show the average roughness values resulting after 10–25 keV Ar cluster ion irradiation to ion dose of 5×10^{15} ions/cm². When the acceleration energies were varied between 10, 15 and 25 keV, the average roughness with all acceleration energies was near the solid line, which means that there was no significant difference in smoothing efficiency compared with that of 20 keV Ar cluster ions. However, the average roughness value with 10 and 15 keV Ar cluster ions was situated a little lower than the curve, whereas that of the 25 keV Ar cluster ions was located a little above the curve.

4.3.2. Incidence angle dependence of surface smoothing

A glancing angle of ion incidence is frequently used to produce surface smoothing by monomer ions. It is reported that ion bombardment at high fluence produces a variety of surface topological features. The most interesting of these are ripple or wavelike structures developed on metals (Ag(1 1 0) [71]), semiconductors (Ge(0 0 1) [72], Si [73,74], GaAs [75,76]) and insulators (SiO₂ [77], glass [78]). This ripple formation is problematic in many applications, including in secondary

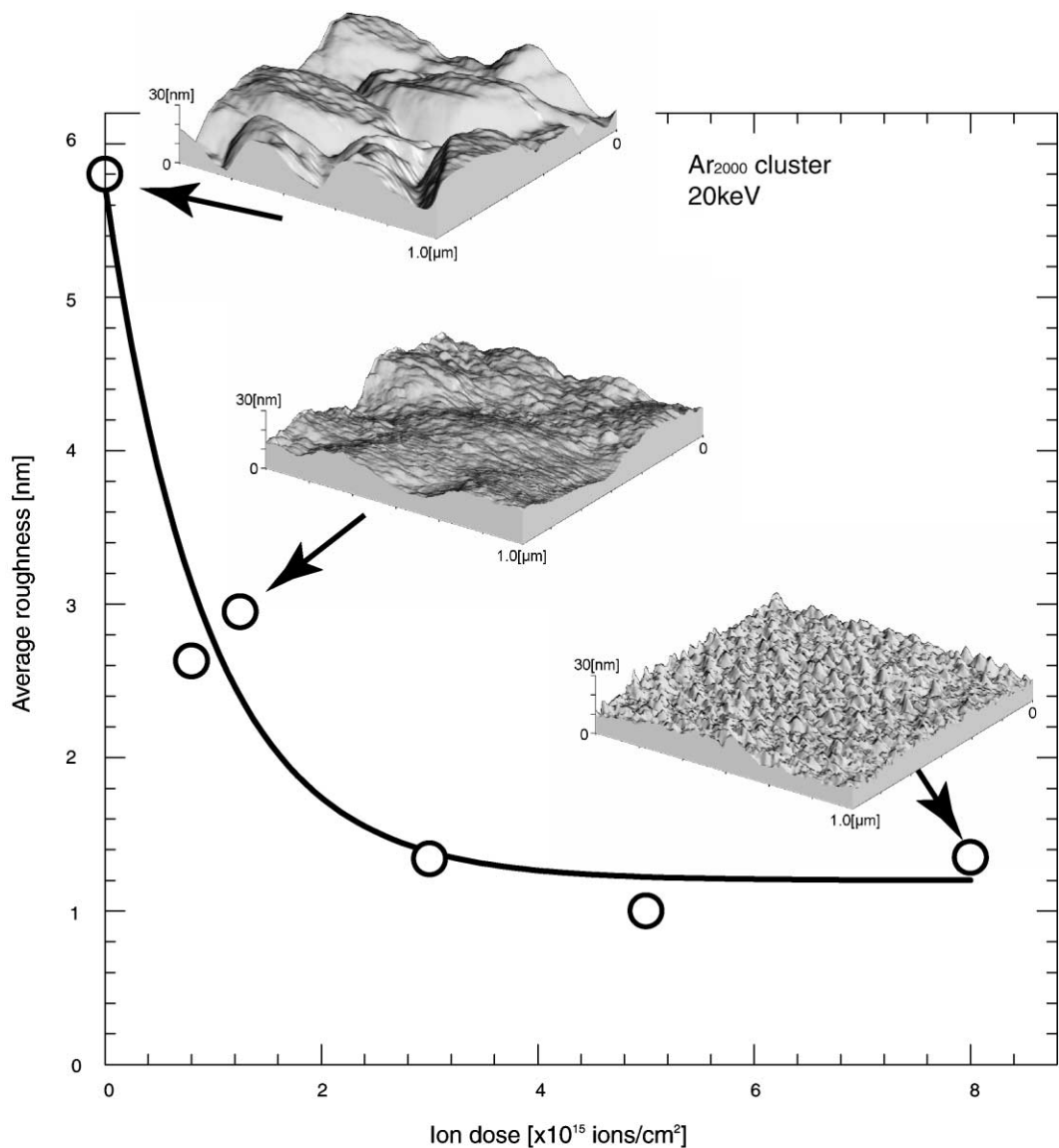


Fig. 45. Ion dose dependence of the surface roughness of Cu irradiated with 20 keV Ar cluster ions.

ion mass spectroscopy (SIMS) [79], depth profiling of Auger electron spectroscopy (AES) [80,81] and ion milling [82]. In a typical SIMS apparatus, the incidence angle of the primary ions is made oblique in order to obtain high sputtering yields and to avoid ion mixing. As sputtering proceeds, ripples are formed on the surface and these ripples induce degradation of the depth resolution.

Ripple formation at glancing incidence by monomer ions was first modeled by Bradley and Harper [83]. They considered it as a competition between the local curvature dependence of the sputtering yield and the thermal diffusion (TD) on the surface. This theory agreed well with many experimental results. However, it could not explain the lack of ripple formation for small incident angles, nor the insensitivity to both temperature and ion energy. Carter and Vishnyakov suggested that ion and atom–atom collision processes provided a ballistic atomic motion parallel to the surface

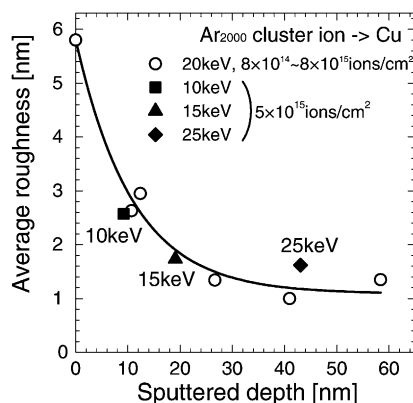


Fig. 46. Sputtered depth dependence of the surface roughness of Cu irradiated with Ar cluster ions with 10–25 keV acceleration energy.

in addition to the generally accepted isotropic diffusivity [73]. Koponen et al. [84] have also simulated ripple formation on ion bombarded surfaces by atomistic simulations and have found the ripple wavelength to be dependent on beam orientation and on the magnitude of diffusion.

In cluster ion bombardment, the situation is quite different. Fig. 47 shows AFM images of Cu surfaces irradiated with Ar cluster ions at several incident angles (0, 15, 30, 45 and 60°) [85]. The average size of the Ar cluster ions was 2000 atoms per cluster. The acceleration energy and the ion dose were 20 keV and 5×10^{15} ions/cm², respectively. The initial Cu surface shown in Fig. 47(a) exhibited average roughness of 6 nm in a $1 \mu\text{m} \times 1 \mu\text{m}$ area. In the case of the incidence angle of 0° (Fig. 47(b)), the Cu surface was smoothed, and its average roughness became 1 nm. On increasing the incidence angles to 15 and 30° (Fig. 47(c) and (d)), distortions begin to appear on the surface. Although the surface smoothing effect was less strong with increasing incidence angle, the surface roughness was improved from the initial value of 6 nm to 1.9 and 4.4 nm, at incidence angles of 15 and 30°, respectively.

When the incidence angle exceeded 45°, the surface roughness increased and ripples whose wave vector was parallel to the incident direction appeared. The wavelength of the ripple produced by a 60° impact was about 0.2 μm . The average roughness values at incidence angles of 45 and 60° were 7.1 and 11.3 nm, respectively, which are higher than the initial value of 6 nm. Thus, surface roughening with ripple formation occurred at high incidence angles with cluster ions. These ripple formations at glancing angles were also observed on silver surfaces.

To confirm that the increase in surface roughness at oblique impact was not due to the reduction of the sputtered depth, the relation between the sputtered depth and the average roughness was measured and is shown in Fig. 48. If the surface smoothing effect at an oblique incidence and at normal incidence were the same, the data points should lie on the same line as at normal incidence, but this was not the case. In the case of an incident angle of 60°, Cu was sputtered to a depth of about 10 nm, and its average roughness was 13 nm, which was five times higher than that for normal incidence at the same sputtered depth. Therefore, it is clear that a surface roughening mechanism exists at oblique incidence.

In the case of a monomer ion beam at a glancing angle of incidence, rotation [86] or rocking of the target [87] is performed during irradiation, which prevents the steady-state of ripple formation, and leads to a smooth surface. In the case of cluster ions at normal incidence, while lateral motions of atoms occur on the surface, the direction in the horizontal plane is random. This non-directional motion of the atoms does not cause steady-state ripple formation. In contrast, one-directional

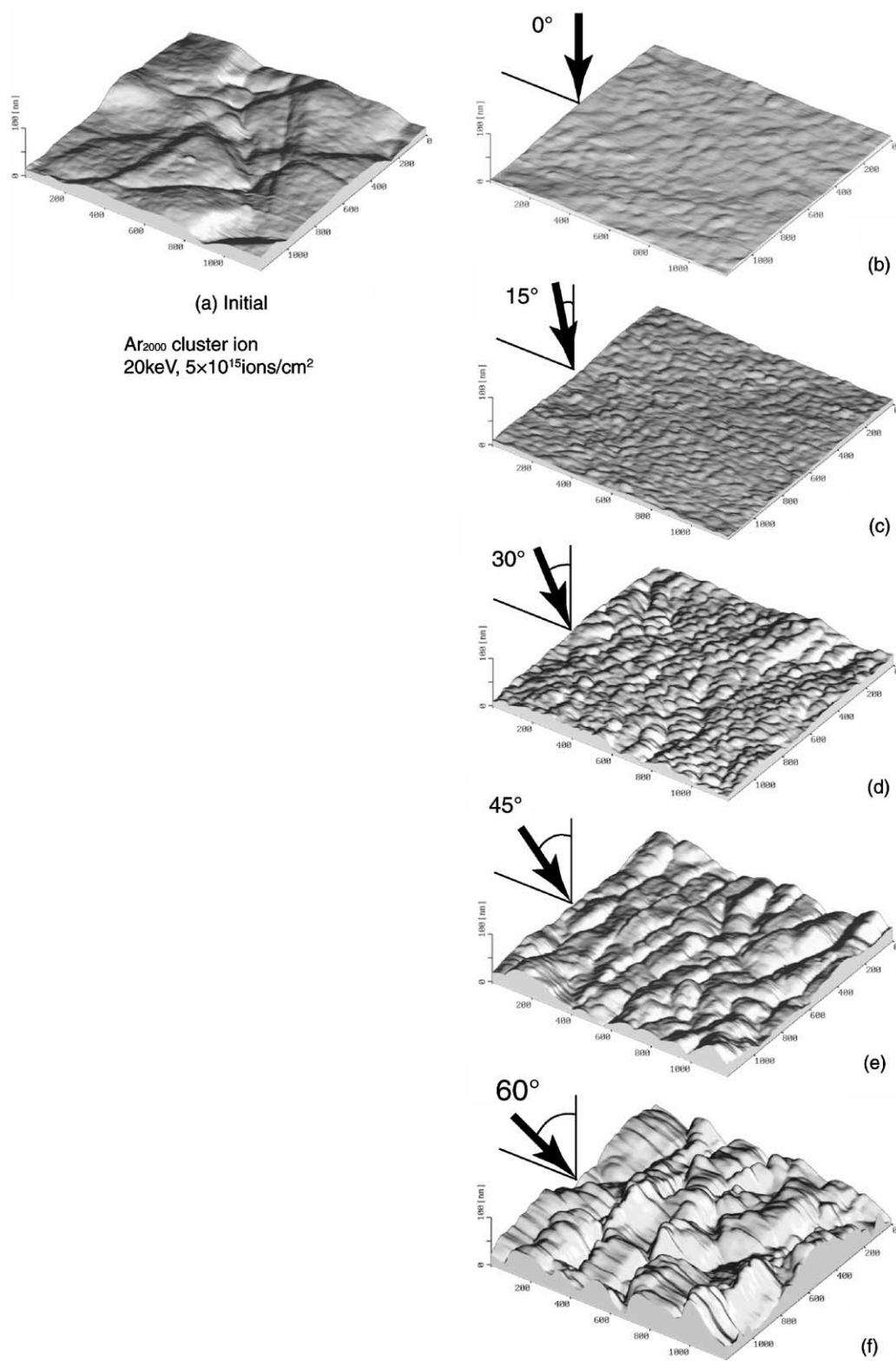


Fig. 47. AFM images of Cu surface irradiated with Ar cluster ions at various incident angles from 0 to 60°.

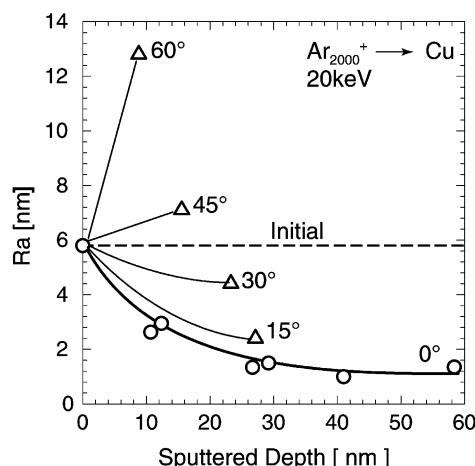


Fig. 48. Dependence of the surface roughness on the sputtered depth at various angles of incidence.

motion of the atoms was observed at off-normal impact of cluster ions, which resulted in steady-state ripple formation, the same as with monomer ions. In the case of monomer ion irradiation, periodic structures are rarely observed on metal surfaces because the diffusion mobility of vacancies and adatoms is high [71]. However, since ripples were formed on a metal surface with cluster ion beam irradiation, TD was expected not to be the main reason for the smoothing or roughening with cluster ions.

4.3.3. Surface smoothing with reactive cluster ions

From the discussion in the previous section, the surface smoothing with Ar cluster ions was influenced by the lateral motion of atoms, termed “lateral sputtering”. However, in the case of reactive cluster ions, the angular distribution of the sputtered atoms is completely different from that with Ar cluster ions. As was shown in Figs. 42 and 43, the angular distribution of Au with SF₆ cluster ions (non-reactive) at normal incidence shows non-cosine distribution, whereas that of W with SF₆ cluster (reactive) follows the isotropic distribution. In addition, the distribution of sputtered Au changes remarkably at the slightly off-normal incidence of 10°, whereas that of W is almost isotropic. Therefore, a SF₆ cluster ion gives rise to only physical sputtering effects on Au, but gives mainly chemical sputtering effects with minor physical sputtering effects on W.

To compare the surface smoothing effects by physical and reactive sputtering, surface morphologies of Au and W irradiated with SF₆ cluster ions were observed using an AFM [88]. Fig. 49 shows AFM images of both Au and W surfaces irradiated with 20 keV SF₆ cluster ions at incident angles of 0 and 60°. The ion dose and the average cluster size were 7×10^{15} ions/cm² and 2000 atoms per cluster, respectively. The initial average roughnesses of the Au and W surfaces were 7.3 and 19 nm, respectively. AFM images of the initial Au surface are shown in Fig. 49(a) and images after irradiations at incidence angles of 0 and 60° are shown in Fig. 49(b) and (c), respectively. The W surface in initial condition, and after irradiation at incident angles of 0 and 60°, is shown in Fig. 49(d), (e) and (f), respectively.

In the case of Au, surface roughness was improved from 7.3 to 2.4 nm at normal incidence (Fig. 49(b)). At an incidence angle of 60°, the surface roughness was 8.5 nm (Fig. 49(c)), which was higher than the initial value. There exists a roughening effect at oblique impact with SF₆ cluster ions which was the same as that of Cu with Ar cluster ions at oblique impact. Surprisingly, ripples whose

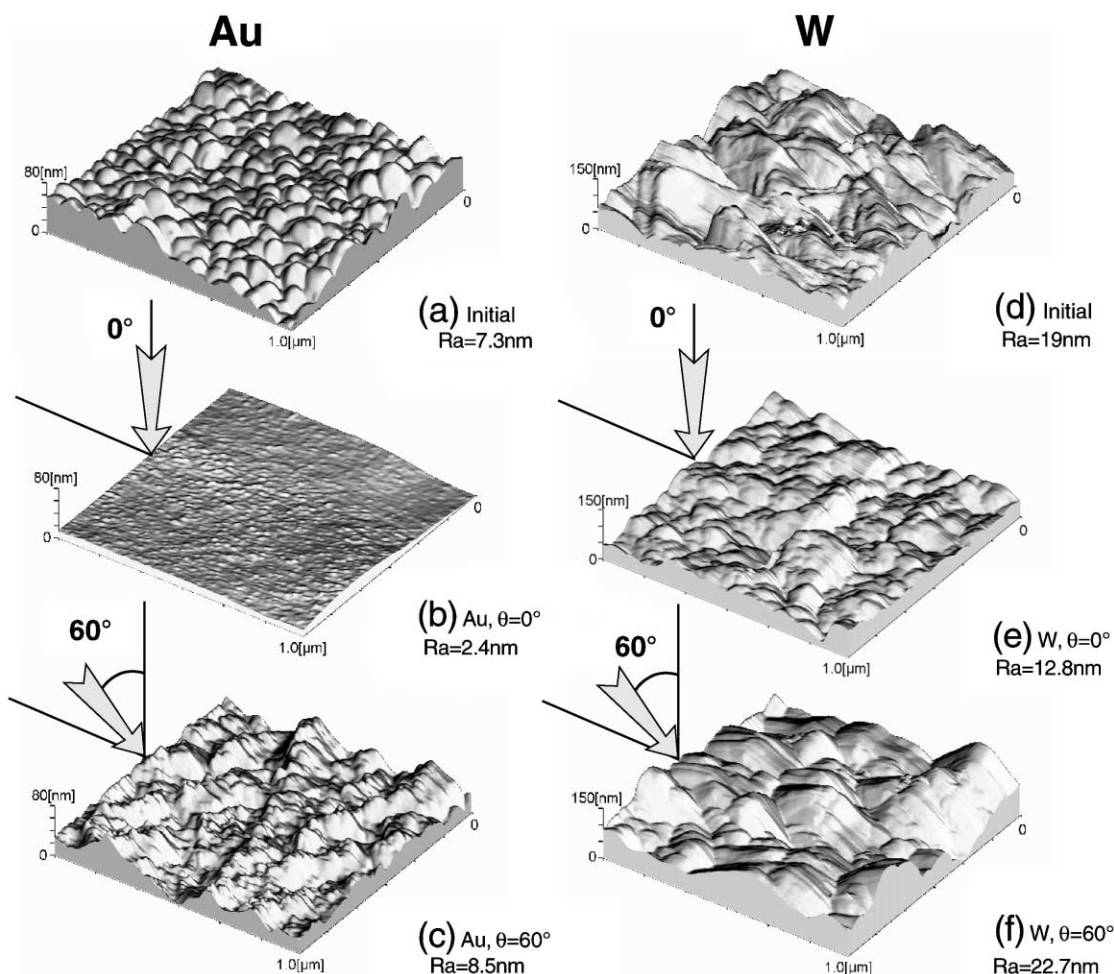


Fig. 49. Surface morphology of Au and W surfaces irradiated with SF_6 cluster ions accelerated at 20 keV, at normal and oblique incident angles. Ion dose was 7×10^{15} ions/cm².

wave vector was parallel to the incident direction were formed at an incident angle of 60° , and these were also observed at high angles of Ar cluster impact as shown in Fig. 47.

In contrast, the surface roughness of W was not similarly improved by SF_6 cluster ions at normal incidence. The average roughness was slightly reduced from 19 to 12.8 nm after SF_6 cluster ion irradiation. However, the morphologies of W surface before (Fig. 49(d)) and after irradiation (Fig. 49(e)) did not differ significantly. Even when the sample was tilted to an incidence angle of 60° , the surface roughness showed only a slight increase from 19 to 22.7 nm, and no ripple formation was observed (Fig. 49(f)).

As was shown in Fig. 43, the angular distribution of W atoms sputtered by SF_6 cluster ions was isotropic and the oblique impact did not cause any marked difference in the angular distribution. This caused poor surface smoothing effects on W due to SF_6 cluster ions. However, there was a small amount of physical sputtering effect, so that the tungsten surface was slightly smoothed by the SF_6 cluster ions. It can therefore be concluded that the effect of surface removal by reactive cluster ions involves a totally different mechanism than that of lateral sputtering, the dominant effect with non-reactive gases.

Table 1
Examples of surface smoothing by gas cluster ion bombardment

Material	Initial surface state	R_a (nm), surface average roughness, before irradiation	Type of irradiation	R_a (nm), surface average roughness, after irradiation
Cu/Si	Large hills of average \varnothing 200 nm	5.8	Ar _n cluster beam, $E = 20$ keV, dose 8×10^{15} ions/cm ²	1.3
YBCO film	Hills, spikes of average \varnothing 13–200 nm	7.0	Ar _n cluster beam 20 keV, 2×10^{16} ions/cm ²	0.8
SiC film	Large hills	14.5	Ar _n cluster beam 20 keV, 1×10^{16} ions/cm ²	0.6
CVD diamond film	Large hills	33.0	Ar _n cluster beam, 20 keV, 1×10^{17} ions/cm ²	4.0

4.3.4. Applications of cluster ion beam sputtering and smoothing

Table 1 shows that GCIB irradiation of different classes of thin film materials results in extraordinary smoothing effects which are distinct from effects due to any other particle irradiation processing techniques. The measurements were made over $1 \mu\text{m} \times 1 \mu\text{m}$ scan areas using an AFM.

4.3.4.1. CVD diamond films. Due to diamond's stability against X-ray radiation, high Young's modulus, high heat conductivity and high transparency, polycrystalline diamond film deposited by a chemical vapor deposition (CVD) technique [89] might be an ideal material to use as a membrane to support X-ray lithography mask patterns [90]. CVD diamond films are also candidates for coating of cutting tools, for wide gap semiconductors, for surface acoustic wave (SAW) devices, for cold emitter arrays in flat panel displays (FPD), and for a wide range of other challenging applications.

There are many structured crystallites on an as-deposited CVD diamond film and the diamond surface roughness is usually high. Even when deposition conditions have been optimized so as to minimize surface roughness, the size of the diamond crystallites has typically been about 300 nm and the roughness has been 20–40 nm for 1–2 μm thick diamond films [91]. In the case of other membrane materials, such as CVD-deposited SiC and SiN_x, surface roughness values of 2–5 nm are common. Thus, there are requirements to develop new surface smoothing techniques for CVD diamond films, and also for other materials. In the case of CVD diamond films, chemical mechanical polishing (CMP) [92], ion beam modification at grazing angles [93], the etch-back method [94], and plasma etching [95,96] have been tried for surface smoothing. There are problems with all of these smoothing techniques. As examples, the etch-back method induces contamination by resist materials, ion beam modification at grazing angles involves slow etching rates and induces damage in the diamond, mechanical polishing techniques produce microscale scratching or cracking of diamond and are out situ wet processes. In addition, smoothing of any surface with a non-planar three-dimensional structure or low mechanical strength is generally difficult by mechanical polishing methods.

A GCIB process, which can offer high sputtering yields, excellent surface smoothing effects, and low introduction of damage is expected to be useful for the smoothing of diamond film surfaces [97]. Diamond thin films deposited on Si substrates by CVD were subjected to irradiation using Ar or Ar/O₂ mixed cluster ion beams. The surface roughness, depth of the etching, transparency of the processed films and Raman spectra were subsequently measured. Based upon the results, GCIB is being considered for smoothing of diamond membranes to be used for X-ray lithography [98].

Fig. 50 shows scanning electron microscopy (SEM) images of CVD diamond films before and after 20 keV Ar cluster ion irradiation. The average cluster size and ion dose were 2000 atoms per cluster and 1×10^{17} ions/cm², respectively. Before irradiation, the diamond surface was comprised

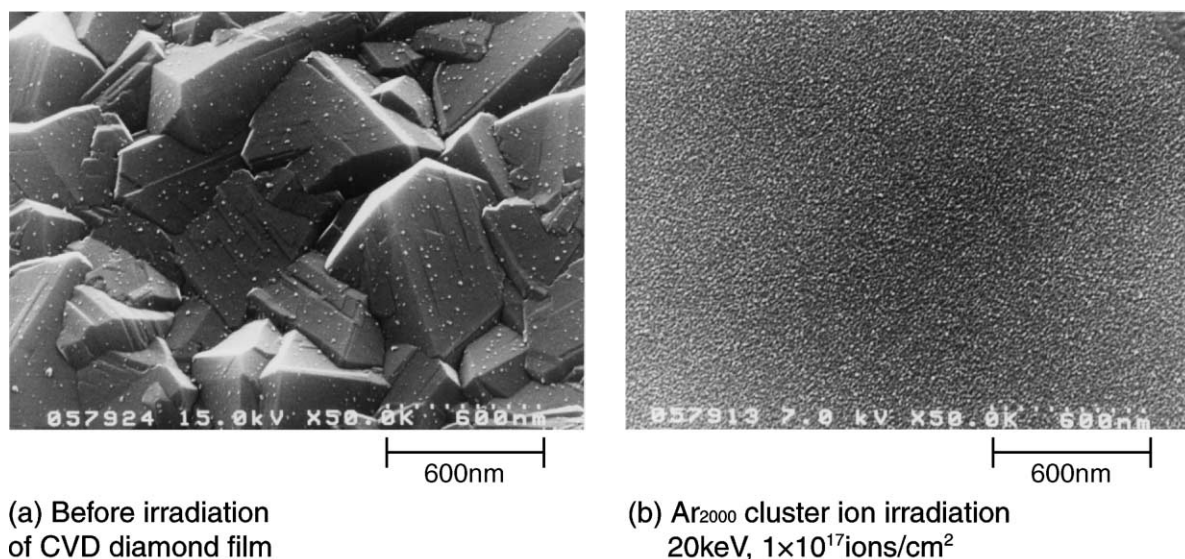


Fig. 50. SEM images of a CVD diamond surface before (a) and after Ar cluster ion irradiation (b). The acceleration energy and the ion dose were 20 keV and 1×10^{17} ions/cm², respectively.

of large numbers of faceted pyramidal grains which are typical of polycrystalline diamond films. The average roughness of the initial diamond surface was 40 nm as measured by AFM. After irradiation, the pyramidal grain structures were no longer present and a flat surface with average roughness of 8 nm was observed. In the case of monomer ion irradiation for polycrystalline diamond film surfaces, sputtering anisotropy on the various facet orientations has been reported. The monomer ion sputtering yield from a $\{1\ 0\ 0\}$ surface is larger than that from a $\{1\ 1\ 1\}$ surface [99], which typically causes roughening of the diamond surface. In the case of cluster ion bombardment, there was no observed influence associated with different crystallite orientations, which was similar to the situation resulting on the Cu surface shown in Fig. 44.

Fig. 51 shows the ion dose dependence of the average roughness of CVD diamond films irradiated by 20 keV Ar cluster ions. In addition to the average roughness values, AFM images of the diamond surfaces before and after irradiation are shown. The AFM scan areas were $1\ \mu\text{m} \times 1\ \mu\text{m}$ and $10\ \mu\text{m} \times 10\ \mu\text{m}$. The cluster ion dose ranged up to 1×10^{17} ions/cm². The measured initial average roughnesses were 40 nm over a $10\ \mu\text{m}$ square scan area and 26 nm over a $1\ \mu\text{m}$ square scan area. The average roughness was observed to decrease monotonically with ion dose. The average roughnesses resulting at an ion dose of 1×10^{17} ions/cm² were 8 nm over the $10\ \mu\text{m}$ square scan area and 2 nm over the $1\ \mu\text{m}$ square area. The diamond film was etched to a depth of 175 nm by the dose of 1×10^{17} ions/cm², which corresponds to a sputtering yield of approximately 30 atoms per ion.

Cluster ion bombardment might cause formation of a thin amorphous graphite layer on the immediate surface of the diamond. Raman spectroscopy was used to observe the surface states on the diamond. Fig. 52 shows Raman spectra of CVD diamond films before and after irradiation by 20 keV Ar cluster ions. The cluster ion dose and average cluster size were 1×10^{17} ions/cm² and 2000 atoms per cluster, respectively. The sharp peaks at $1332\ \text{cm}^{-1}$ in the Raman spectra are attributed to diamond. If a graphite layer were to have been present on the diamond surface following cluster ion bombardment, a broad peak around $1600\ \text{cm}^{-1}$ would have been expected to be observed in the Raman spectrum. However, there was no marked difference between the initial and post-bombardment spectra and, consequently, the crystal structure of the diamond surface was

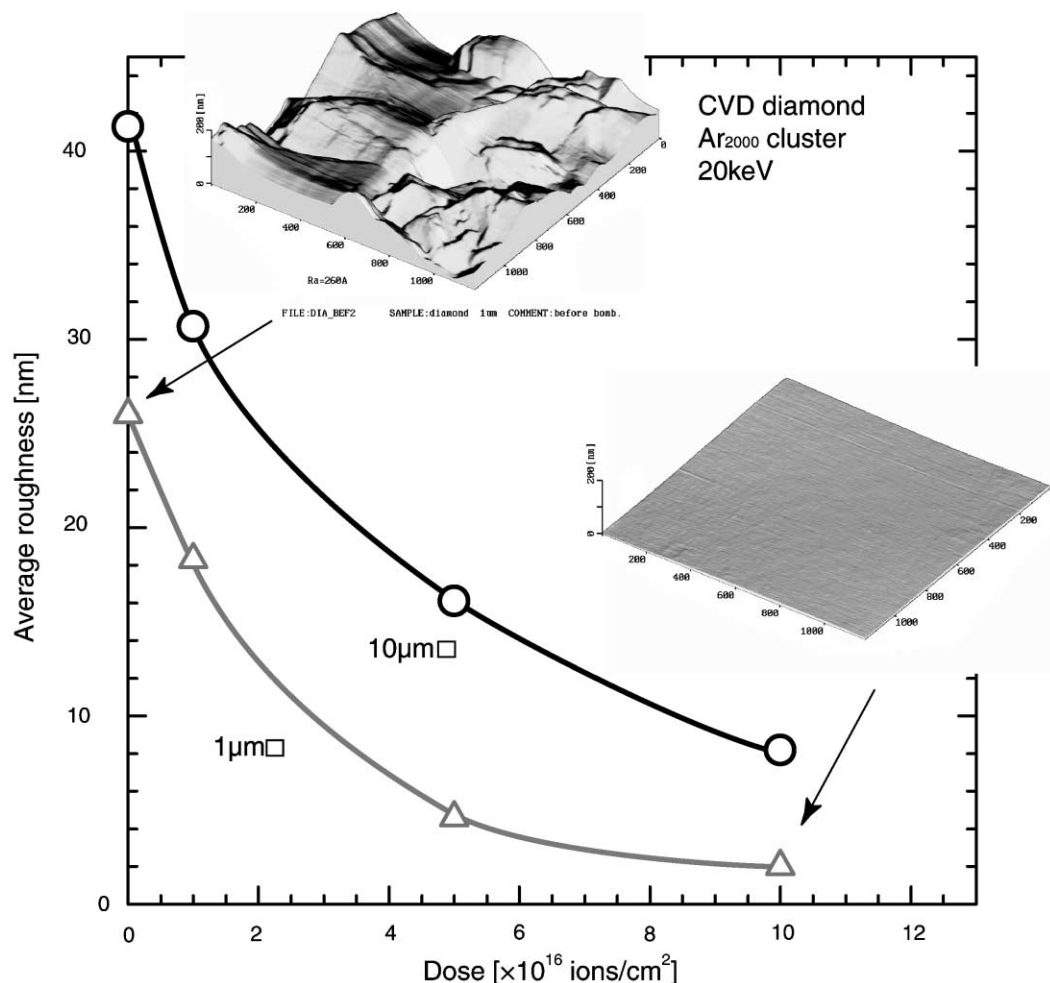


Fig. 51. Ion dose dependence of average roughness of CVD diamond irradiated with Ar cluster ions accelerated at 20 keV.

believed to have remained essentially unchanged following Ar cluster irradiation. Any amorphous layer which might have been created on the surface would have to have been extremely thin.

Fig. 53 shows the ion dose dependence of the surface roughness of diamond films irradiated by cluster ion beams of pure Ar and by cluster ion beams of mixed Ar and O₂ with oxygen content f_{O_2} of 5%. From Fig. 53, it can be seen that the surface roughness with Ar/O₂ mixed cluster ions fell more rapidly than in the case of pure Ar cluster ions. At an ion dose of 1×10^{17} ions/cm², the average roughness was about half of that produced by the pure Ar cluster ions. Therefore, by using Ar/O₂ cluster ions, smoother diamond surfaces can be obtained at lower ion doses. A small amount of oxygen (<5%) mixed in the argon was enough to significantly improve smoothing efficiency. The surface smoothing effect was found to become weaker when the flow fraction f_{O_2} was increased beyond 5%.

In order to fabricate thin diamond membranes to be used for lithographic masks, diamond films 2 μm thick were deposited onto Si substrates by microwave plasma CVD using a CH₄ and H₂ gas mixture. After deposition, the diamond films were irradiated at normal incidence by cluster ion beams. The Si substrate was then removed from an area of the films by etching from the reverse side

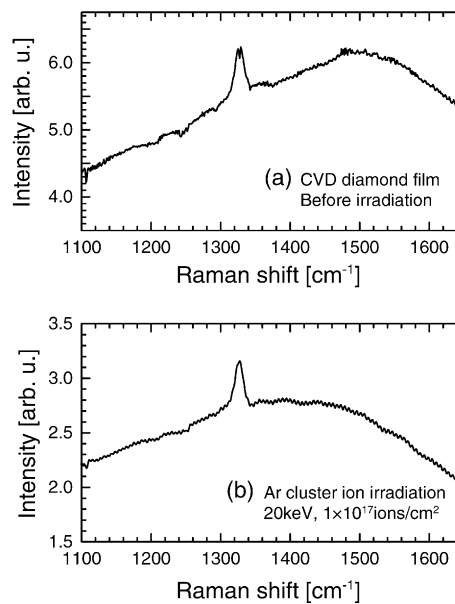


Fig. 52. Raman spectra of CVD diamond films before and after 20 keV Ar cluster ion irradiation.

using an HF/HNO₃ solvent. Good optical transmittance of the diamond films is to be important in order to allow for alignment of the X-ray lithography patterns. Fig. 54 shows optical transmittance of the edge-supported CVD diamond films after irradiation by Ar/O₂ mixed cluster ion beams to a dose of 1×10^{17} ions/cm² at 20 keV using oxygen flow fraction f_{O_2} of 5%. Over the measured wavelength range of 400–800 nm, the optical transmittance of 2 μ m thick diamond films after irradiation by the mixed gas clusters was almost the same as the initial transmittance. If a graphite layer were to have been formed on the diamond surface, the optical transmittance would have decreased and processed diamond would have appeared dark. There was no visible change after irradiation. Because the sputtering yield of diamond due to oxygen cluster ions was high, a damaged layer would be etched away even if it were to have formed on the surface. By using the Ar and O₂ mixed cluster ion beams, very smooth flat diamond surfaces without graphite layers can be obtained.

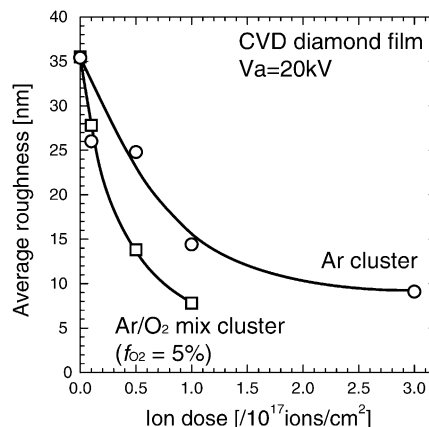


Fig. 53. Ion dose dependence of the surface roughness of CVD diamond irradiated with pure Ar cluster and Ar/O₂ mixed cluster ion beams. The mole fraction of O₂ was 5%.

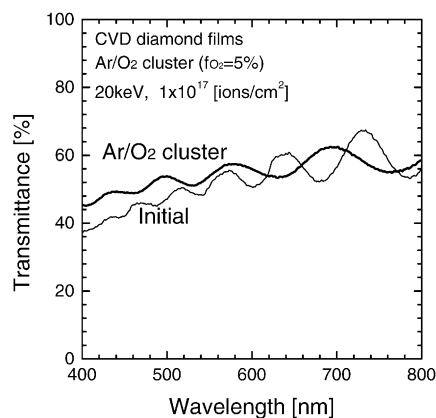


Fig. 54. Optical transmittance of diamond film irradiated with Ar and O₂ cluster ions at 20 keV acceleration energy and 1×10^{17} ions/cm² ion dose.

To demonstrate capability of the cluster ion beam for fabrication of a membrane for an X-ray lithography mask, a cluster ion beam of Ar mixed with 5% O₂ was used to irradiate a 30 mm × 30 mm area of diamond film. Fig. 55 shows a 3 in. wafer on which diamond thin film was deposited to 2 μm thickness using plasma CVD. The acceleration energy and ion dose for the cluster ion bombardment were 20 keV and 4×10^{16} ions/cm², respectively. The entire 30 mm × 30 mm area was smoothed uniformly by the cluster ions. From this result, it can be expected that the GCIB technique will be very promising for surface smoothing of diamond films.

4.3.4.2. SiC wafer. SiC is a material which is considered to be promising for electronic power devices. The energy gap of SiC is three times higher than that of Si, the heat of conductivity is three times higher, and the breakdown voltage is 10 times higher. These superior characteristics provide a

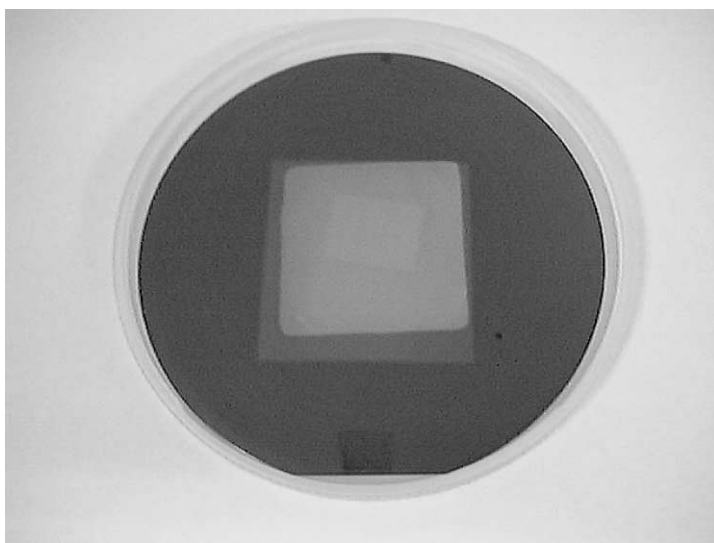


Fig. 55. CVD diamond films of 30 mm × 30 mm area irradiated with 20 keV Ar/O₂ mixed cluster ions ($f_{O_2} = 5\%$). After irradiation, the Si substrate was etched from the back side.

potential solution for meeting difficult operating requirements such as those which exist in very high power devices, in devices which must operate at high temperatures, and in devices which must exhibit high stability against X-ray radiation.

Single crystalline SiC can be grown using sublimation from SiC powder. SiC can have many crystal polytypes such as 4H–SiC, 6H–SiC, 3C–SiC, etc. The actual crystal structure of grown SiC depends upon the substrate material and the growth temperature. Today, 6H–SiC and 4H–SiC wafers are commercially available in various sizes. However, the SiC surfaces have to be mechanically polished, and the polishing induces scratches such as shown in Fig. 56(a). Together with internal defects within the SiC wafers, the defects on the surfaces make it difficult to fabricate semiconductor devices on presently available SiC wafers.

To demonstrate the possibility for removing scratches produced on SiC wafer surfaces by mechanical polishing, SiC wafers were irradiated by Ar cluster ion beams. Fig. 56 shows AFM images from a 1 in. diameter 6H–SiC wafer (Cree Research, Inc.) before and after 20 keV Ar cluster ion irradiation at normal incidence. The ion energy and dose were 20 keV and 1×10^{17} ions/cm², respectively. Before irradiation, the initial surfaces included high densities of polishing scratches and had average roughness of 0.75 nm. In contrast, no scratches were observed after Ar cluster ion irradiation and a very flat surface was obtained. The average roughness of the cluster ion bombarded surface was 0.56 nm. Surface smoothing with cluster ions is most suitable for removal of locally small surface structures, such as small scratches on the initial surface.

In addition to the demonstration for monolithic SiC substrates, SiC thin films deposited on Si substrates by CVD were also irradiated by Ar cluster ion beams. The average cluster size and the acceleration energy were 2000 atoms per cluster and 20 keV, respectively. The initial roughness of the SiC thin films was 15 nm, and the average roughness decreased with the ion dose in the same manner as that observed on Cu or diamond films. Following an ion dose of 5×10^{16} ions/cm², the

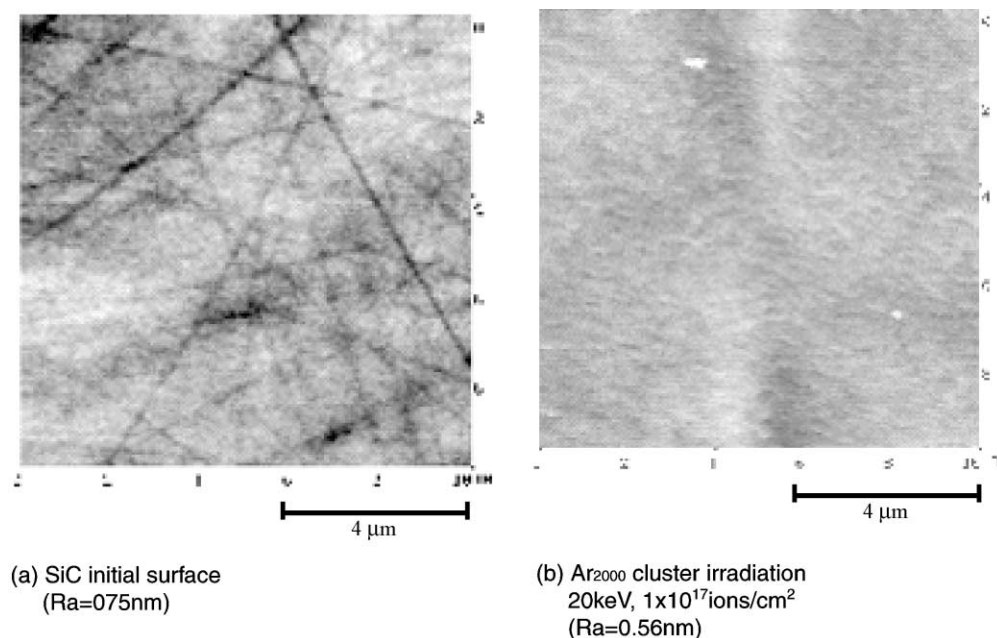


Fig. 56. AFM images of a 6H–SiC wafer (1 in.²) (Cree Research, Inc.) irradiated with 20 keV Ar cluster ions at a dose of 1×10^{17} ions/cm². (a) Before irradiation large scratches are observed from mechanical polishing ($R_a = 0.75$ nm — by AFM); (b) after irradiation ($R_a = 0.56$ nm).

surface roughness was improved from 15 to 1.2 nm. Although SiC is a compound material, no influence due to selective sputtering was observed following cluster ion beam irradiations. Similar to the diamond films, SiC is a very hard material which is generally considered to be very difficult to smooth. The cluster ion beam smoothing technique promises to be useful for very hard materials such as SiC and diamond.

4.3.4.3. YBCO superconducting films. For the fabrication of high temperature superconductor (HTS) thin film devices, especially for multi-layer integrated circuits, a smooth HTS surface is crucial for reliability and for yield of the fabrication processes. In the formation of HTS integrated circuits, up to six levels of masking with epitaxial film growth are required. Therefore, the surface roughness of the first HTS layer is considered to be critical to the reproducibility and yield of the HTS junctions. In HTS thin film epitaxial depositions, the substrate is usually kept at a high temperature, resulting in the formation of islands or mesas which produce rough surfaces. Therefore, $\text{YBa}_2\text{Cu}_3\text{O}_7$ (YBCO) HTS films were prepared and surface smoothing of these films was performed by Ar cluster ion beams [10].

YBCO thin films, 900 nm thick, were produced on LaAlO_3 by laser ablation. The films were then irradiated by 20 keV Ar cluster beams having clusters of average size 2000 atoms. Fig. 57 shows AFM images from YBCO films before and after irradiation. As can be seen in Fig. 57(a), prior to cluster irradiation, islands or mesas were present on the deposited YBCO films due to the variation of growth speed along the various crystalline directions [10]. Additional debris and impurities deposited by the deposition process were also present on the film surfaces. The average roughness of the YBCO film shown in Fig. 57 was 40 nm over the $1\text{ }\mu\text{m} \times 1\text{ }\mu\text{m}$ area. After irradiation by the Ar cluster ions to a dose of 2×10^{16} ions/ cm^2 , the YBCO surface was smoothed significantly. The depth of YBCO film removed by the cluster bombardment was 220 nm. As can be seen in Fig. 57(b), small hillocks and other features initially present on the film surface were totally removed by the bombardment. The average roughness after cluster irradiation was 1.2 nm in a $1\text{ }\mu\text{m} \times 1\text{ }\mu\text{m}$ area. Although $\text{Y}_1\text{Ba}_2\text{Cu}_3\text{O}_7$ involves 13 atoms of four different elements per unit cell, and has the very complex perovskite structure compared to simple mono-elements and binary compounds, the Ar cluster beam was able to smooth the YBCO surface without inducing selective sputtering of the individual elements.

In order to fabricate HTS multi-layer devices, it is desired that epitaxial layers can be grown upon the YBCO surface after pretreatment smoothing by an Ar cluster ion beam. To verify that a

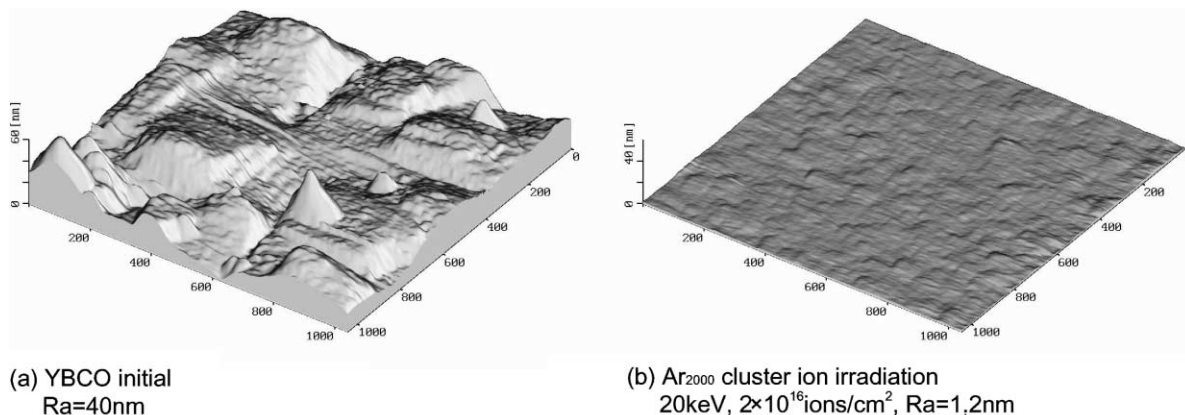


Fig. 57. AFM images of YBCO thin films irradiated with Ar cluster ions accelerated at 20 keV. Ion dose was 2×10^{16} ions/ cm^2 .

YBCO surface processed by the cluster ion beam could support epitaxial growth, the bombarded film was first thermally annealed and then a second YBCO layer was deposited on the surface by laser ablation. Homo-epitaxial YBCO films were obtained and crystalline re-growth was verified by the RBS channeling method [10]. Although the newly deposited film was single crystal, the surface was rough, as expected. If it is necessary to fabricate structures on top of this new layer, surface smoothing with a cluster beam will be required again for the second layer. Thus, smoothed multi-layer systems can be constructed. This procedure is expected to be important for improving the yield and reliability of HTS junction IC devices, as well as for fabrication of passive stripline delay lines, antennas and filters that will use HTS films.

5. Cluster ion implantation

Cluster ion beam technology has been found to be able to offer solutions for a number of well-known problems associated with conventional monomer ion beam implantation. Cluster ion implantation has been found to offer important differences which are expected to lead to development of cluster approaches as additional tools for device miniaturization. Prospective advantages of cluster ion implantation are discussed in the sections below.

5.1. Low-energy ion implantation and suppression of TED

Low-energy ion implantation is expected to be essential for the fabrication of shallow junctions as the size of LSI devices decreases. Because of its very low-energy per atom characteristics, GCIB has been proposed for this application [5]. As has been previously discussed, by using cluster ion beams it is relatively easy to obtain high-current beams with equivalently low ion energies. However, in conventional low-energy ion implanters, it is difficult to generate high-current beams, because the low-energy ion beams are subject to space charge effect problems in the beam transport line. Also, for shallow junction formation, some way must be found to suppress TED which occurs during annealing. The unique interaction kinetics and damage formation characteristics associated with the localized energy deposition and multiple collision properties of cluster ion impacts have been discussed in Section 3.2. Because of these characteristics, cluster implantation is expected to be able to produce shallow, abrupt defect profiles and to be able to avoid charge-up damage and channeling effects.

Cluster ion implantation using decaborane ($B_{10}H_{14}$) has been proposed for shallow junction formation [99]. Extensive investigation of this topic has been carried out by collaboration between researchers at Kyoto University and at Fujitsu Research Laboratories [12,100]. Decaborane ($B_{10}H_{14}$, melting point: 99.7°C, boiling point: 213°C at STP conditions) is a stable solid at room temperature. Decaborane is of course actually a molecule, not a gas cluster, but it does contain 10 boron atoms and fourteen hydrogen atoms. When an ionized and accelerated decaborane molecule impacts upon a surface, the nature of this impact, which involves simultaneous impingement by 10 boron atoms, is essentially the same as what would occur in the impact of a cluster ion that might have been formed from ten boron-containing molecules. Ion implantation using decaborane ions can offer all of the advantages associated with GCIB processing which were discussed in Section 3.2.

For the implantation process, vapor sublimed from a solid $B_{10}H_{14}$ source was fed directly into an ionization chamber and was ionized by electron bombardment. Because $B_{10}H_{14}$ is easily fragmented by high-energy electron bombardment, the electron energy had to be kept low (60 eV) in order to avoid dissociation of $B_{10}H_{14}$. The ionized $B_{10}H_{14}$ clusters were extracted and then accelerated through potentials of 2–20 keV before being electrostatically scanned over target surfaces.

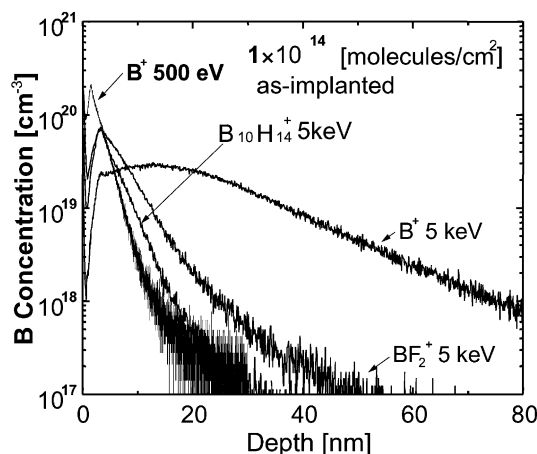


Fig. 58. Boron SIMS depth profiles from Si samples implanted with B, BF₂ and decaborane (B₁₀H₁₄) ions with energy of 5 keV, compared with 500 eV boron monomer ion. The ion dose was fixed at 1×10^{14} ions/cm² for boron and BF₂ and at 1×10^{13} ions/cm² for decaborane. The B distribution for the sample implanted with 5 keV decaborane ions is similar to that for the sample implanted with 500 eV boron monomer ions.

In order to compare low-energy implantation effects, boron atom distributions were introduced into Si using 0.5 and 5 keV boron monomer ions, 5 keV BF₂ ions by conventional implantation, and 5 keV decaborane ions as described above. The resulting boron distributions are compared in Fig. 58. The ion dose was 1×10^{14} ions/cm² for the B and BF₂ ions. For decaborane, the ion dose was one order of magnitude lower (1×10^{13} ions/cm²) than that used for the B and BF₂ implants, because each decaborane ion implants 10 B atoms. As can be seen from Fig. 58, at the same implantation energy, the heavy ion species were implanted to shallower depth. The boron atom distribution with 5 keV decaborane ions is seen to be identical to that resulting with 500 eV boron monomer ions. These results demonstrate that the cluster ion beam technique can be suitable for shallow implantation.

Typical SIMS dopant profiles of boron, implanted with decaborane at 10 and 5 keV, before and after annealing at 900 and 1000°C, are shown in Fig. 59. As the profiles show, TED was essentially completely suppressed. The TD which occurred at 1000°C is dependent on the dopant density and was a consequence of the very high concentration of boron in these very shallow implants. Boron TED is thought to be mediated by Si interstitials and therefore can be controlled by introducing C atoms to act as traps for Si interstitials [101,102]. The generation of Si interstitials appears to be highly suppressed in the case of decaborane cluster ion implantation. Moreover, the amorphized area formed by the decaborane implant may also function as a sink for silicon interstitials thus decreasing their mobilities.

Fig. 60 shows the dependence of the actual atomic dose on implant energy, as measured by nuclear reaction analysis (NRA). As shown, the actual atomic dose at 20 keV was larger than the required dose of 1×10^{15} atoms/cm² (1×10^{14} ions/cm²), because the measured ion current was smaller than the actual ion current as a result of the emission of secondary ions. In the case of low-energy (2 and 3 keV) ion implantation on the other hand, the actual atomic dose was measured to be lower than the required dose. This result shows that the efficiency of implantation decreases as the implant energy decreases. This is a critical problem in low-energy ion implantation.

Because the suppression of TED is an important issue for the formation of ultra-shallow junctions, significant effort has been spent trying to understand and model TED. It is believed

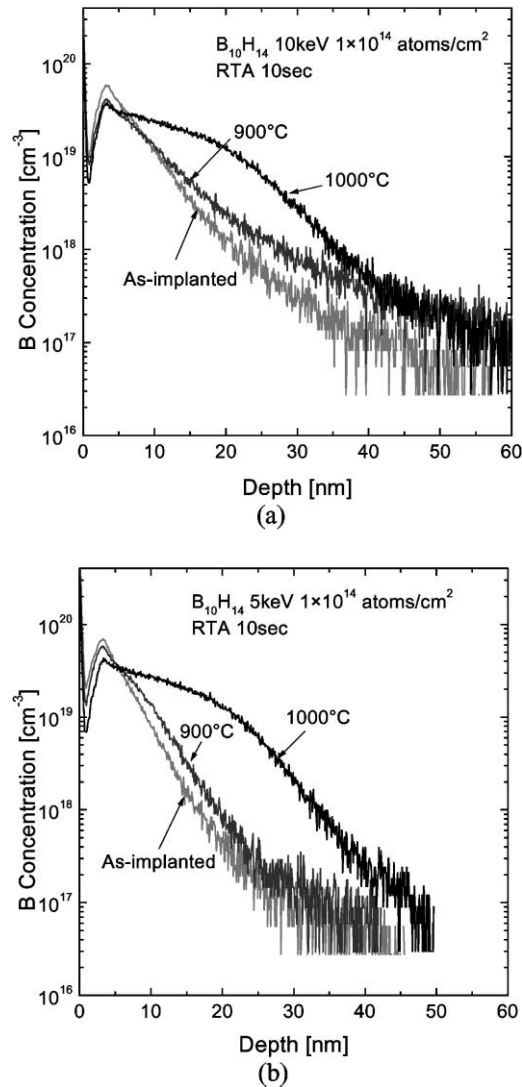


Fig. 59. SIMS analysis of B concentration after B₁₀H₁₄ implantation at 5, 3 and 2 keV before and after 10 s RTA at 900 and 1000°C.

that TED is caused by the implantation-induced damage, which evolves into supersaturation of interstitials [101]. In order to reveal the relationship between TED and the damage introduced by B₁₀H₁₄ ion implantation, the effect of implant energy on the diffusion length was investigated. The diffusion length is defined as the deviation between as-implanted and annealed profiles at 3×10^{17} atoms/cm³. Fig. 61 shows the diffusion length obtained from the SIMS profiles during annealing at 900 and 1000°C as a function of implant energy. This figure demonstrates that in the case of annealing at 900°C, TED is reduced by decreasing the implant energy. On the other hand, in the case of annealing at 1000°C, the diffusion length does not depend on implant energy. These results suggest that the mechanism of B diffusion is different in the cases of the 900 and 1000°C annealing temperatures. Fig. 62 shows the energy dependence of diffusivity enhancements (ratio of observed diffusivity to equilibrium diffusivity: D_B/D_B^*). Equilibrium boron diffusivities are

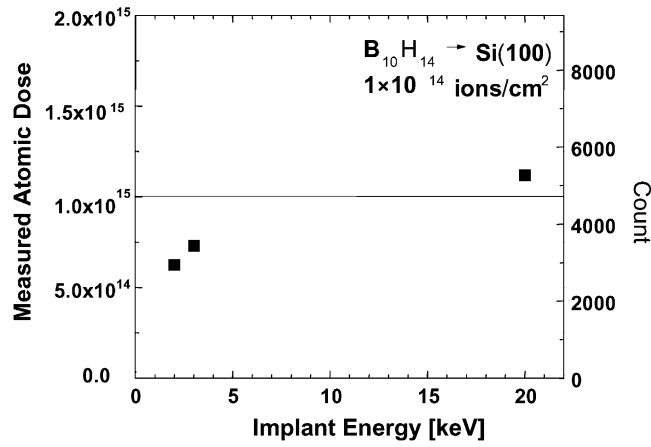


Fig. 60. The dependence of the actual atomic dose on implant energy. The line at 10^{15} ions/cm² shows the required dose.

given by Eq. (5.1) [48]:

$$D_B^* = D_B^0 + D_B^+ \text{ (cm}^2\text{/s)} \quad (5.1)$$

$$D_B^0 = 0.278 \exp\left(\frac{-3.946 \times 10^4}{T}\right)$$

$$D_B^+ = 0.23 \exp\left(\frac{-3.946 \times 10^4}{T}\right)$$

For the case of the annealing at 900°C, the large enhancement value of 70 associated with 10 keV implantation results from the occurrence of TED. However, the enhancement value decreased with decreasing implant energy, and the TED enhancement was not observed when the incident energy was below 3 keV. This result indicates that low-energy B₁₀H₁₄ ion implantation successfully suppressed the TED during annealing at 900°C. In the case of 1000°C annealing, the enhancement values were, however, almost constant with energy and were small, ranging around 3–4.

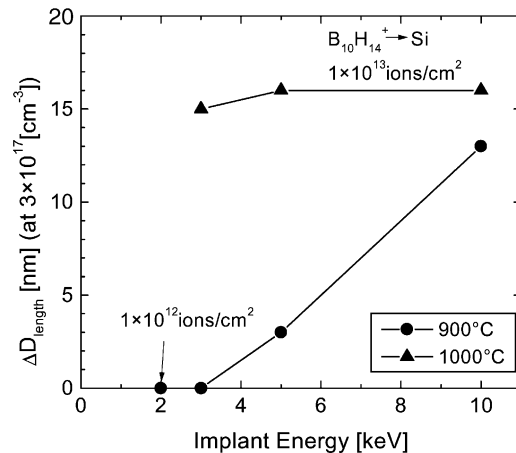


Fig. 61. The dependence of boron diffusion length on implantation energy.

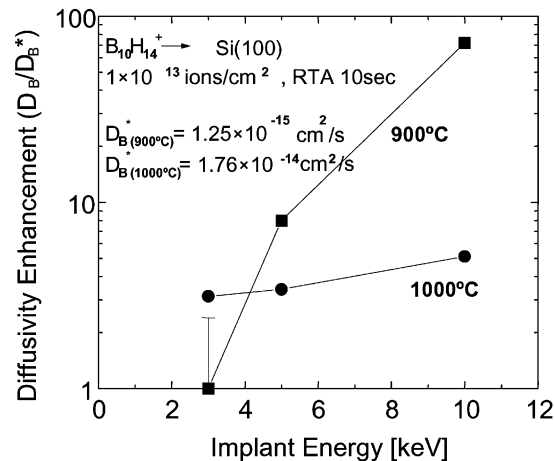


Fig. 62. The dependence of diffusivity enhancement (D_B/D_B^*) on implantation energy.

These results suggest that the mechanism of TED at 3 keV is not the same as that at 10 keV. It has been reported that in the case of 10 keV implantation, the interstitials which cause the TED are generated by the $\{3\ 1\ 1\}$ defect in the end-of-range (EOR) damage, while in the case of 3 keV, the interstitials are generated near the surface during recovery of the amorphous layer. Since both TED and TD are almost perfectly suppressed by 3 keV implantation and by 900°C annealing, it is expected that ultra-shallow junctions can be formed under these conditions.

A possible explanation for the suppression of TED with decreasing implantation energy during 900°C annealing is that the damage is concentrated in a region very close to the surface. In such a case, the surface is believed to act as a sink for interstitials. Consequently, the interstitials introduced by ion implantation are recombined and annihilated at the surface, thereby suppressing the TED [102,103].

Fig. 63 shows the observed experimental relationship between diffusivity enhancement and implanted B dose. At 3 keV, the enhancement is seen to be only weakly dose dependent for

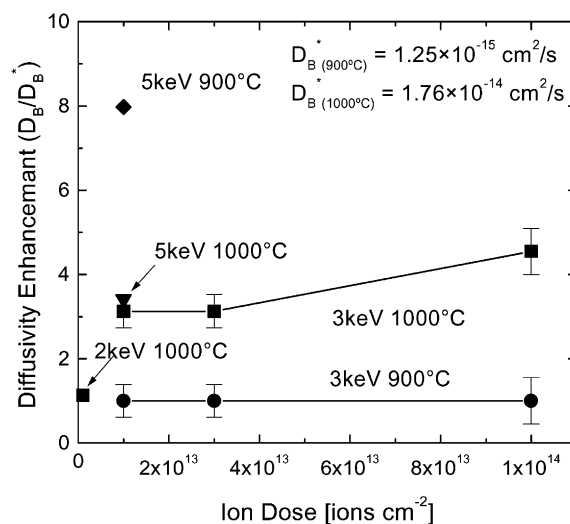


Fig. 63. The dependence of diffusivity enhancement (D_B/D_B^*) on implantation dose.

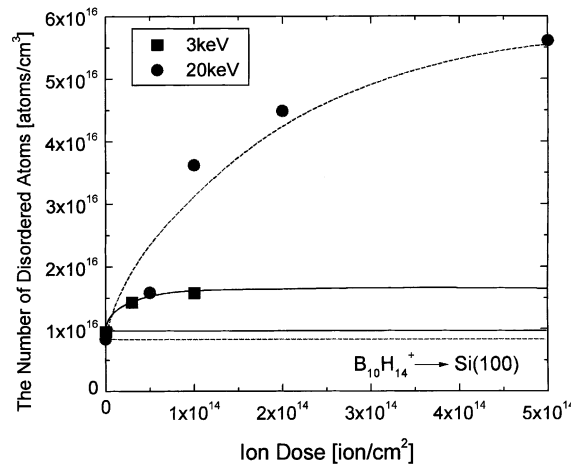


Fig. 64. The dependence of the number of disordered atoms on ion dose.

annealing at 900 or 1000°C. At 900°C, diffusivity is very small and the amount of boron diffusion could not be measured by SIMS in the case of any of the implant doses. During 1000°C annealing, the amount of TED does depend weakly on implant dose, probably because the number of defects near the surface has become saturated and the implanted region of substrate becomes amorphous for any dose greater than 1×10^{13} ions/cm². Fig. 64 shows the observed dependence of the number of disordered atoms upon ion dose. B₁₀H₁₄ ions were implanted at 3 and 20 keV. The total numbers of resulting disordered atoms were obtained by integration over the surface peaks in the RBS channeling spectra [104]. The density of disordered atoms on the unirradiated surface, due to surface distortion and intrinsic vacancies, is shown as a background in Fig. 64. In the case of B₁₀H₁₄ ion implantation at 20 keV, the number of disordered atoms saturated at about 6×10^{16} atoms/cm³ for a dose of 5×10^{14} ions/cm². On the other hand, with 3 keV implant the disordered atoms saturated at about 1.6×10^{16} atoms/cm³ for a dose of 1×10^{14} ions/cm². Because the projected range (R_p) decreases with decreasing implant energy, the amorphous layer becomes shallower and the number of disordered atoms decreases, which means that the threshold dose required to amorphize the layer decreases with implant energy. In the case of B₁₀H₁₄ ion implantation at 3 keV, an amorphous layer was formed near the surface at a dose of 1×10^{13} ions/cm². Therefore, as is indicated in Fig. 64, in the case of low-energy implantation, the enhancement during annealing at 900 and 1000°C depended only weakly on implant dose. On the other hand, in the case of implantation at 10 keV, the implanted region, at a dose of 1×10^{13} ions/cm², was not fully amorphized and large numbers of interstitial Si atoms remain in the substrate such that TED was consequently very extensive.

5.2. Application to p-MOSFET fabrication

To demonstrate B₁₀H₁₄ cluster implantation for shallow source/drain formation, 40 nm p-MOSFETs have been fabricated [12]. B₁₀H₁₄ ion implantation for p-type source/drain (S/D) junctions was performed at 30 keV to a dose of 1×10^{13} ions/cm² and was followed by an anneal at 1000°C for 10 s. A junction depth of 20 nm was achieved. For S/D extensions, B₁₀H₁₄ ion implantation was carried out at 2 keV to a dose of 1×10^{12} ions/cm², followed by annealing at 900°C for 10 s. In the absence of TED or TD, an ultra-shallow 7 nm junction was achieved.

Among the devices which were fabricated, a highest resulting drive current (I_d) of 0.40 mA/μm (with current at 0 V (I_{off}) = 1 nA/mm and drain voltage (V_d) = −1.8 V), was 15% better than best

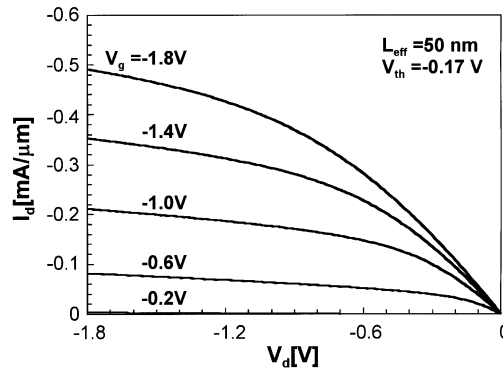


Fig. 65. I_d - V_d characteristic of a p-MOSFET with L_{eff} of 0.05 μm .

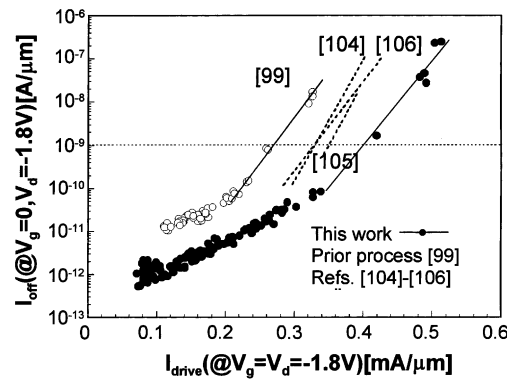


Fig. 66. I vs. I_{off} values of the new process compared to those of the old process [109] and recently reported high-performance p-MOSFETs [106–108].

previously published data [105–107]. A low S/D series resistance R_{sd} of 750 Ω m was achieved, even when a high sheet resistance (>20 k Ω /sq.) was used for the extension regions (due to the diminished extension length). The smallest p-MOSFET to date, with an effective gate length L_{eff} of 38 nm, was demonstrated. Fig. 65 shows the I_d versus V_d characteristic of a p-MOSFET with an L_{eff} of 0.05 μm . A drive current of 0.5 mA/ μm , with a threshold voltage V_{th} of -0.17 V, which is considered excellent for these dimensions, was achieved. In Fig. 66, the I_d versus I_{off} values of the devices fabricated using the new process are plotted relative to those of devices from the older process [100] and of recently reported high-performance p-MOSFETs [105–107]. This work has resulted in a maximum I_d of 0.40 and 0.70 mA/ μm due to the success in scaling L_{eff} down to 0.05 and 0.038 μm , without the device being affected by short channel effect (SCE), and while maintaining a low R_{sd} . This result is significant because it guarantees an improvement in drive current by scaling device size down to at least 0.04 μm with suppressed SCE. Fig. 67 is an SEM image of the device illustrating a poly-Si gate length of 40 nm after side-wall removal.

6. Cluster ion beam-assisted deposition and applications

Direct ion beam deposition (DIBD) and ion-assisted deposition (IAD) are candidate processes for depositing high quality thin films. However, there are damage effects induced by energetic ions

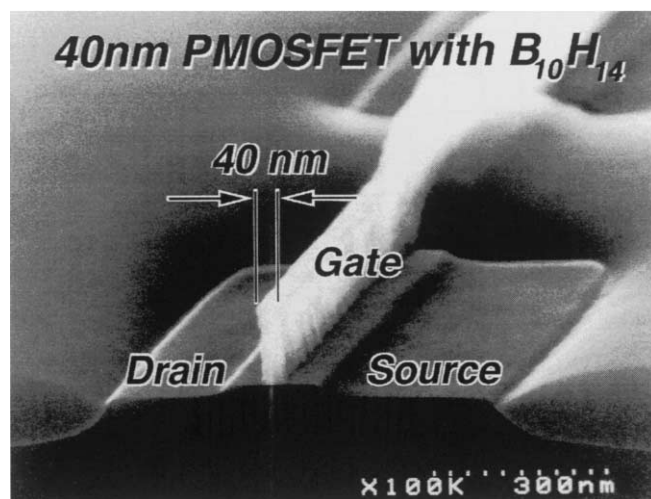


Fig. 67. SEM image of p-MOSFET having a 40 nm gate.

bombardment in some delicate materials, which makes very low-energy ion beams highly desirable. However, as mentioned previously, high currents of low-energy beams are difficult to produce and transport. GCIB-assisted processes are well suited to solve these problems for deposition applications.

There are three basic approaches available for producing thin films using GCIB. These differ according to the substrate to be used and the type of film desired. In the first approach, cluster ions of a reactive gas can interact directly with a target material. In the case of silicon dioxide to be formed on Si, for example, it is sufficient to simply bombard the Si substrate by oxygen clusters in order to create a thin layer of SiO_2 [108]. This has already been described in Section 3.3 above in the context of chemical reaction enhancement by GCIB. The films produced by these types of reactions of atoms comprising the cluster ion with atoms of a target surface are necessarily very thin.

The second and third approaches to GCIB-assisted deposition, which are suggested in Fig. 68, can be used to deposit various types of films by using either reactive or non-reactive process variations. In these variations, vapor of some material is deposited onto a substrate while simultaneous bombardment of the growth surface by gas cluster ions is occurring. If the cluster ions are of a non-reactive gas such as argon, this method can be used to form films having very high packing densities, smooth surfaces, improved adhesion, etc. If the cluster ions are of a reactive gas such as oxygen, the cluster gas atoms will react with the depositing vapor atoms. The method has been used in deposition of oxides, such as PbO_2 , and indium oxide films [109–111]. Tin-doped indium oxide (ITO), which is one of the most extensively used oxides, is transparent in the visible spectrum and is electrically conductive. Because of its relatively low resistivity, less than $1 \times 10^{-3} \Omega \text{ cm}$, and high transparency to visible light, above 80% at 550 nm, ITO has found numerous applications in opto-electronic devices, for example as transparent electrodes of flat panel display (FPD) devices and in photovoltaic devices.

One of the most interesting features of gas cluster ion-assisted deposition is its versatility. For example, the evaporation source for ITO in a GCIB-assisted deposition process can be either a prepared high purity mixture of indium and tin oxides, ITO pellets, or pure In and Sn metals which are evaporated simultaneously while being oxidized by the cluster ion beam at the substrate surface [110,111]. Because the deposition in the latter case involves two metals, two separate evaporation sources have to be used, and each must be controlled using a separate deposition rate monitor. Similar results have been obtained using co-deposition of metals and by use of pre-mixed ITO pellets [111].

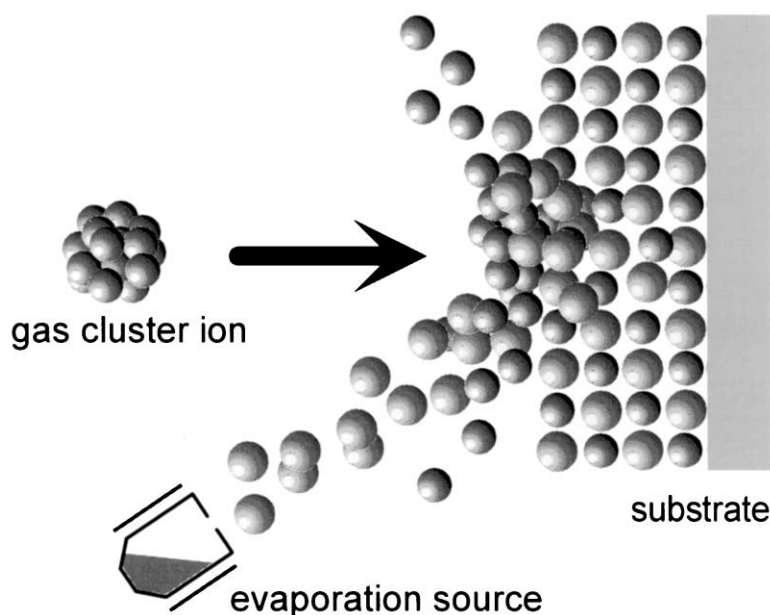
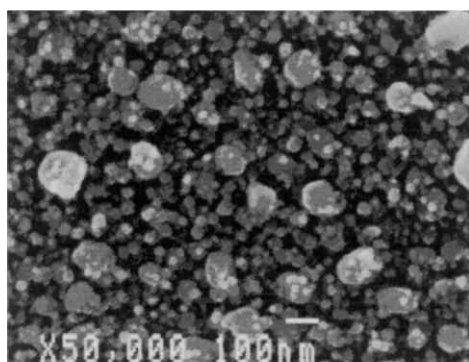


Fig. 68. Schematic diagram of the GCIB-assisted deposition process.

A series of experiments was performed with In to study the effects of various cluster ion parameters on the structure and properties of indium oxide films. The effect of the cluster ion acceleration voltage on the morphology of ITO films produced using GCIB-assisted deposition is shown in Fig. 69(a)–(c). Scanning electron microscopy (SEM) micrographs are shown from films which were obtained using an In target either without acceleration energy (Fig. 69(a)), or with very low acceleration energy (below 5 keV) (Fig. 69(b)). In these cases, because the amount of oxidation which occurred was insufficient, metallic precipitates were present on the surfaces, and these precipitates caused deterioration of the optical properties: the films were dark and visibly non-transparent. Highly transparent films were obtained when the oxygen clusters ions were accelerated to energies above 5 keV [112]. These films (Fig. 69(c)) exhibited featureless morphologies with no metallic islands on their surfaces. Outside of the cluster-irradiated areas, the deposited films were dark and non-transparent, indicating that the cluster ion beam caused enhanced oxidation of the metals. The irradiated areas were also extremely smooth relative to the non-irradiated areas.

In Fig. 70, the In/O ratios of films which were grown at room temperature are shown as a function of the acceleration voltage (V_a). The composition of the InO_x films was measured by Rutherford backscattering spectrometry (RBS). Stoichiometric In_2O_3 films were obtained when the O_2 cluster ion energy was above 5 keV. At 7 keV the films were highly transparent. This result clarifies the role of the oxygen cluster ions during film growth: for efficient oxidation of the indium surface, a particular energy range is required, and the mere presence of oxygen in the ambient is not sufficient to produce the correct stoichiometry. Also, an acceleration voltage above 5 kV was found to be necessary in order to form high quality films by means of enhanced chemical reactions. Approximately, 10% of the atoms of the irradiating O_2 cluster ions have been found to have become incorporated in the films. AFM measurements showed that above 5 keV very smooth films were formed with surface roughness of less than 2 nm, which is considered to be sufficiently smooth for utilization in many opto-electronic devices. Indium oxide films formed by irradiation with O_2 cluster



(a) $V_a = 0$ kV



(b) $V_a = 3$ kV



(c) $V_a = 9$ kV

Fig. 69. Micrographs showing dependence of ITO film morphology upon acceleration voltage of O_2 cluster ions. SEM micrographs from films obtained from an In target either without (a), and very low acceleration energy (below 5 keV) (b). The InO_x film becomes transparent for the acceleration voltages higher than 5 keV.

ion beams at energies higher than 7 keV at 250°C substrate temperature showed high visible transparency of over 80% and resistivity values smaller than $8.5 \times 10^{-5} \Omega \text{ cm}$ [111].

Due to the very low-energy ion bombardment effects, and other unique properties of GCIB bombardment which have been described in other sections of this monograph, GCIB-assisted

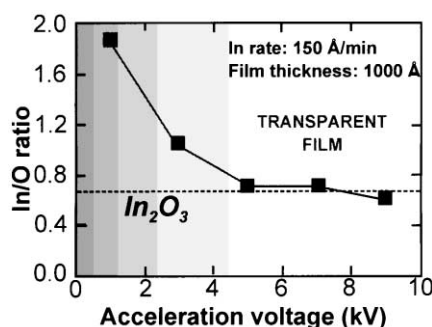


Fig. 70. In/O ratio of films grown at room temperature as a function of the acceleration voltage (V_a).

deposition generally produces thin films compatible to, or better than, the films which can be obtained by other physical vapor deposition methods.

7. GCIB equipment

Commercial GCIB equipment is now available to support fundamental investigations of cluster ion–surface interactions, for process applications development, and for practical production in the case of some of the applications which have been recognized. High throughput GCIB processors are being developed for a broad range of applications related to semiconductor devices, photonic devices, optical surfaces, sensors, micromachines, tribological surfaces, and implantable biomedical devices. Substantial projects to develop GCIB equipment to satisfy production requirements in many of these areas are being supported by governments of the United States and Japan [112,113].

Earliest equipment developed at Kyoto University for investigations of gas cluster ion interactions with solid surfaces was operational by 1988 [5]. Subsequently, several GCIB systems were constructed at Kyoto University in different configurations for fundamental studies of cluster physics and to facilitate investigations of prospective applications of the unique phenomena which occur during cluster ion interactions with surfaces. Many of the wide range of GCIB laboratory equipment configurations employed to date have resulted in contributions to the technology which are discussed elsewhere in this review. Various GCIB units designed and constructed for developmental work have provided gas cluster ions at energies from only a few keV to as high as 200 keV. Several systems now operating at Kyoto University are able to provide cluster ion beams into target chambers incorporating in situ diagnostic tools such as reflection high energy electron diffraction (RHEED), secondary ion mass spectrometry (SIMS) and scanning tunneling microscopy (STM). Several systems at Kyoto University and elsewhere provide cluster ion beams of inert gases or reactive gases for surface smoothing and etching investigations and other systems combine gas cluster ion sources and physical vapor deposition sources for cluster ion-assisted thin film growth purposes.

In order to produce a beam of energetic gas cluster ions which can be used to modify a surface, a GCIB processor employs a gas expansion nozzle to generate neutral clusters, a skimmer to transmit a directed axial stream of neutral clusters while blocking flow of excess gas from the nozzle, an assembly to cause ionization of the clusters, and electrodes at high potentials to accelerate the ionized clusters to high energies. Because the gas flows used for cluster generation are relatively high, typically several hundreds of sccm for most gases, separate pumps are usually employed for the

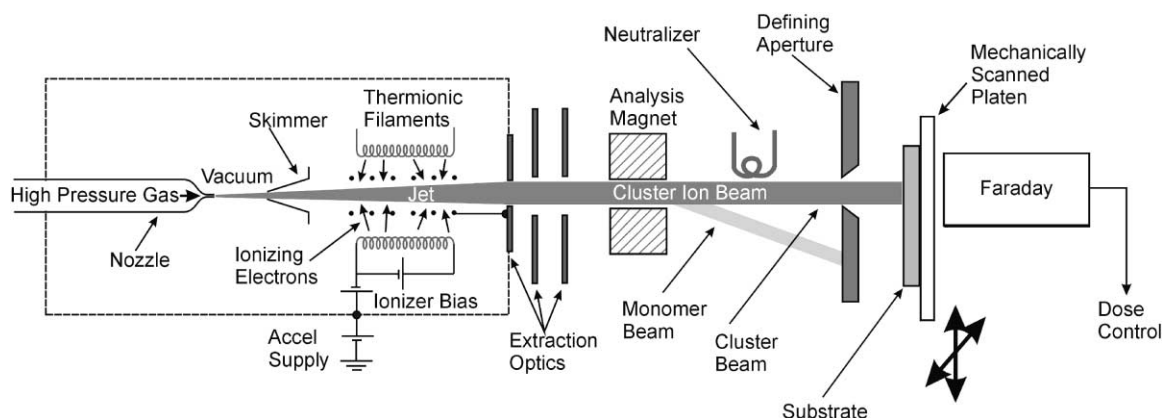


Fig. 71. Typical schematic configuration of a GCIB processor.

nozzle, ionization/acceleration and target chamber stages of a GCIB system. Sometimes, a differential pumping stage is used between the cluster nozzle source and the ionization chamber in order to allow high gas flows through the cluster generation nozzle while still maintaining acceptably good vacuum in the cluster ionization and acceleration regions. Additional lens assemblies can be utilized to improve the efficiency of cluster ion transport to target substrates. Electrostatic or magnet filtering is employed to eliminate monomer ions and small cluster ions which behave differently than large cluster ions upon target impact. Uniform processing of large area substrates is accomplished by means of electrostatic scanning of the cluster ion beams or by mechanical scanning of substrates within a fixed beam. Faraday current monitors allow accurate cluster ion dose control. Low-energy electron flood sources can be used to prevent charge build-up on surfaces undergoing processing. Fig. 71 shows a schematic representation of a typical GCIB processing system.

Beam current is a parameter of concern for GCIB practical applications. Production processes demand adequate throughput capabilities in order to be economically viable and throughputs of GCIB processes are usually limited by available cluster ion currents. Cluster ion currents in early equipment were very low, sometimes only of the order of a few nanoamperes, and the factors responsible for beam intensity limitations were not well understood at the time. In order to generate and transport even the very low cluster ion currents which could be produced in early systems, GCIB equipment typically employed costly high-capacity vacuum pumps. By 1995, it was recognized that it would not be practical to use substantially greater gas flows in order to increase cluster ion beam currents to the levels to be required for production processors. Efforts to improve generation and effective use of neutral clusters, and to increase efficiency of cluster ionization and subsequent transport and use of the ionized cluster beams, without increasing gas consumption and pumping requirements, have been successful. Cluster ion beam currents of several hundred microamperes are now being produced with source gas flows of less than 500 sccm. At present beam current levels, many production applications of GCIB are economically practical. Other applications will require beam currents of 1000 μA or more. Development programs now being conducted are expected to result in milliampere-level cluster ion beams within about 2 years.

During collaboration with Kyoto University in support of work sponsored by the Japan Research and Development Corporation, Epion Corporation began development of commercial GCIB equipment in 1995. GCIB systems built by Epion for research and development now exist in a several laboratories in Japan and the US Epion now offers GCIB production systems for atomic scale surface smoothing applications. Fig. 72 shows a photograph of a 25 keV GCIB Ultra-SmootherTM



Fig. 72. Epion GCIB Ultra-Smoothen™ Production System.

Production System equipped for high throughput automated processing of 200 mm diameter substrates. The system employs argon cluster ions to reduce surface roughness of high-quality metal, semiconductor, or insulator surfaces to limits typically below 1 nm R_a . A number of these systems are operational in Japan and the US.

8. Conclusions

In conclusion, bombardment of solid surfaces using GCIBs has been found to involve a number of important new surface interaction phenomena that are now beginning to be understood. Many unresolved questions remain. GCIB can satisfy demands for processes that can enhance the nano-level smoothness of surfaces of virtually all materials, can form thin films of superior quality and can process at high rates with little or no damage to crystal structures. GCIBs appear to offer major advantages for an unusually wide range of challenging applications. Experimental demonstrations of GCIB capabilities and development of manufacturing-worthy equipment for applications which will take advantage of these capabilities are advancing rapidly.

References

- [1] T. Geherels, Collisions with comets and asteroids, *Sci. Am.* (1996) 54.
- [2] K.L. Merkle, W.J. ager, *Philos. Mag. A* 44 (1981) 741.

- [3] D. Takeuchi, K. Fukushima, J. Matsuo, I. Yamada, Nucl. Instrum. Meth. B 121 (1997) 493.
- [4] Z. Insepov, I. Yamada, Nucl. Instrum. Meth. B 112 (1996) 16.
- [5] I. Yamada, in: Proceedings of the 14th Symposium on Ion Sources and Ion-Assisted Technology, Tokyo, The Ion Engineering Society of Japan, Tokyo, 1991, p. 227.
- [6] I. Yamada, Radiat. Effects Defects Solids 124 (1992) 69.
- [7] I. Yamada, Nucl. Instrum. Meth. B 148 (1999) 1.
- [8] I. Yamada, J. Matsuo, in: Proceedings of the MRS Symposium, Vol. 396, 1996, p. 149.
- [9] I. Yamada, Nucl. Instrum. Meth. B 112 (1996) 242.
- [10] W.K. Chu, Y.P. Li, J.R. Liu, J.Z. Wu, S.C. Tidrow, N. Toyoda, J. Matsuo, I. Yamada, Appl. Phys. Lett. 72 (1998) 246.
- [11] A. Nishiyama, M. Adachi, N. Toyoda, N. Hagiwara, J. Matsuo, I. Yamada, in: Proceedings of the Conference on Application of Accelerators in Research and Industry'98, AIP Press, New York, 1999, p. 421.
- [12] K. Goto, J. Matsuo, Y. Tada, T. Tanaka, Y. Momiyama, T. Sugii, I. Yamada, A high performance 50 nm PMOSFET using decaborane ($B_{10}H_{14}$) ion implantation and 2-step activation annealing process, IEDM Tech. Dig., IEEE (1997) 471.
- [13] I. Yamada, J. Matsuo, E.C. Jones, D. Takeuchi, T. Aoki, K. Goto, T. Sugii, Mat. Res. Soc. Symp. Proc. 438 (1997) 363.
- [14] H. Katsumata, J. Matsuo, T. Nishihara, T. Tachibana, K. Yamada, M. Adachi, E. Minami, I. Yamada, in: Proceedings of the Conference on Application of Accelerators in Research and Industry'98, AIP Press, New York, 1999, p. 409.
- [15] E.W. Becker, On the history of cluster beams, in: F. Trager, G. zu Putlitz (Eds.), Proceedings of the International Symposium on Metal Clusters, 1986, Springer, Berlin, 1986, p. 1.
- [16] R.L. McEachern, W.L. Brown, M.F. Jarrold, M. Sosnowski, G.H. Takaoka, H. Usui, I. Yamada, J. Vac. Sci. Technol. A 9 (1991) 3105.
- [17] W.L. Brown, M.F. Jarrold, R.L. McEachern, M. Sosnowski, G. Takaoka, H. Usui, I. Yamada, Nucl. Instrum. Meth. B 59/60 (1991) 182.
- [18] T.G. Dietz, M.A. Duncan, D.E. Powers, R.E. Smalley, J. Chem. Phys. 74 (1981) 6511.
- [19] H. Schaber, T.P. Martin, Surf. Sci. 156 (1985) 64.
- [20] E.W. Becker, K. Bier, W. Henkes, Z. Phys. 146 (1956) 333.
- [21] O. Hagen, Surf. Sci. 106 (1981) 101.
- [22] L.D. Landau, E.M. Lifshitz, Fluid Mechanics, Pergamon Press, London, 1987, p. 316.
- [23] J.A. Anderson, in: P.W. Wegener (Ed.), Molecular Beams and Low Density Gas Dynamics, Marcel Dekker, New York, 1974, Chapter 1, p. 1.
- [24] O. Hagen, in: P.W. Wegener (Ed.), Molecular Beams and Low Density Gas Dynamics, Marcel Dekker, New York, 1974, Chapter 2, p. 93.
- [25] O.F. Hagen, W. Obert, J. Chem. Phys. 56 (1972) 1793.
- [26] E. Ashkenas, F.S. Sherman, in: J.H. de Leeuw (Ed.), Rarefied Gas Dynamics, Vol. 2, Academic Press, New York, 1966, p. 84.
- [27] R.F.K. Herzog, W.P. Poschenrieder, J. Franzen, Radiat. Effects 18 (1973) 199.
- [28] R.G. Wilson, G.R. Brewer, Ion Beams — with Applications to Ion Implantation, Wiley, New York, 1973, p. 19.
- [29] H.H. Andersen, Matematisk-fysiske Meddelelser 43 (1993) 127.
- [30] P. Sigmund, in: R. Behrisch (Ed.), Sputtering by Particle Bombardment I, Springer, Berlin, Heidelberg, 1981.
- [31] R.J. Beuler, L. Friedman, Chem. Rev. 86 (1986) 521.
- [32] D.E. Maxwell, in: D.J. Roddy, R.O. Pepin, R.B. Merrill (Eds.), Impact and Explosion Cratering, Pergamon Press, New York, 1977, p. 1003.
- [33] H. Szichman, S. Eliezer, Laser Particle Beams 10 (1992) 23.
- [34] R. Beuler, L. Friedman, Chem. Rev. 86 (1986) 521.
- [35] C. Deutch, Laser Particle Beams 10 (1992) 217.
- [36] R.A. Zubarev, I.S. Bitensky, P.A. Demirev, B.U.R. Sundqvist, Nucl. Instrum. Meth. B 88 (1994) 143.
- [37] Ya.B. Zel'dovich, Yu.P. Raiser, in: Physics of Shock Waves and High-Temperature Hydrodynamic Phenomena, Academic Press, New York, 1967, Chapter 11.
- [38] D.A. Thompson, Radiat. Eff. 56 (1981) 105.
- [39] H.H. Andersen, H.L. Bay, J. Appl. Phys. 45 (1974) 953.
- [40] I. Yamada, W.L. Brown, J.A. Northby, M. Sosnowski, Nucl. Inst. Meth. Phys. Res. B 82 (1993) 223.
- [41] N. Toyoda, J. Matsuo, I. Yamada, in: Proceedings of the Conference on Application of Accelerators in Research and Industry'96, AIP Press, New York, 1997, p. 483.
- [42] Z. Insepov, I. Yamada, Nucl. Instrum. Meth. B 99 (1995) 248.
- [43] Z. Insepov, I. Yamada, Nucl. Instrum. Meth. B 121 (1997) 44.
- [44] Z. Insepov, I. Yamada, M. Sosnowski, Mater. Chem. Phys. 54 (1998) 234.
- [45] Z. Insepov, M. Sosnowski, I. Yamada, Trans. Mat. Res. Soc. Jpn. 17 (1994) 111.
- [46] Z. Insepov, I. Yamada, Nucl. Instrum. Meth. B 153 (1999) 199.
- [47] Y. Kitazoe, Y. Yamamura, Radiat. Effects Lett. 50 (1980) 39.

- [48] F.M. Fahey, P.B. Griffin, J.D. Plummer, Point defect and dopant diffusion in silicon, *Rev. Mod. Phys.* 61 (1989) 289.
- [49] E. Chasen, S.T. Picraux, J.M. Poate, J.O. Borland, M. Current, T. Diaz dela Rubia, D.J. Eaglesham, O.W. Holland, M.E. Law, C.W. Magee, J.W. Meyer, J. Meingailis, A.F. Tasch, *Appl. Phys. Rev.* 81 (1997) 6513.
- [50] M. Tang, L. Colombo, J. Zhu, T.D. dela Rubia, *Phys. Rev.* 55 (1997) 14279.
- [51] M. Akizuki, J. Matsuo, I. Yamada, M. Harada, S. Ogasawara, A. Doi, *Nucl. Instrum. Meth. B* 112 (1996) 83.
- [52] J. Matsuo, N. Toyoda, M. Akizuki, I. Yamada, *Nucl. Instrum. Meth. B* 121 (1997) 459.
- [53] K. Kanaya, K. Houjou, K. Koga, F. Toki, *Jpn. J. Appl. Phys.* 12 (1973) 1297.
- [54] N. Laegreid, G.K. Wehner, *J. Appl. Phys.* 32 (1961) 365.
- [55] R.C. Bradley, *Phys. Rev.* 93 (1954) 719.
- [56] H.H. Andersen, H.L. Bay, in: R. Behrisch (Ed.), *Sputtering by Particle Bombardment I*, Springer, Berlin, 1981, p. 145.
- [57] N. Matsunami, Y. Yamamura, Y. Ichikawa, N. Itoh, Y. Kazumata, S. Miyagawa, K. Morita, R. Shimizu, H. Tawara, *Atom. Data Nucl. Data Tables* 31 (1984) 1.
- [58] H. Fetz, *Z. Physik* 119 (1942) 590.
- [59] G.K. Wehner, *J. Appl. Phys.* 25 (1954) 270.
- [60] P. Sigmund, *Phys. Rev.* 184 (1969) 383.
- [61] G.K. Wehner, D. Rosenberg, *J. Appl. Phys.* 31 (1960) 177.
- [62] N. Toyoda, H. Kitani, N. Hagiwara, T. Aoki, J. Matsuo, I. Yamada, *Mater. Chem. Phys.* 54 (1998) 262.
- [63] W. Zhenxia, L. Wenyun, W. Chuanshan, W. Wenmin, *Vacuum* 47 (1996) 1465.
- [64] P. Sigmund, *Nucl. Instrum. Meth. B* 27 (1987) 1.
- [65] D.J. Oostra, A. Haring, A.E. de Vries, F.H.M. Sanders, G.N.A. van Veen, *Nucl. Instrum. Meth. B* 13 (1986) 556.
- [66] C.M. Melliard-Smith, J. Mogab, in: J.L. Vossen, W. Kern (Eds.), *Thin Film Processes*, Academic Press, New York, 1978, Chapter 5-2, p. 502.
- [67] H. Gokan, M. Itoh, S. Esho, *J. Vac. Sci. Technol. B* 2 (1984) 34.
- [68] J.W. Coburn, H.F. Winters, *Nucl. Instrum. Meth. B* 27 (1987) 243.
- [69] J.L. Vossen, *J. Appl. Phys.* 47 (1976) 544.
- [70] Z. Liao, T.T. Sheng, *Appl. Phys. Lett.* 32 (1978) 716.
- [71] S. Rusponi, C. Boragno, U. Valbusa, *Phys. Rev. Lett.* 78 (1997) 2795.
- [72] E. Chason, T.M. Mayer, B.K. Kellerman, D.T. McIlroy, A.J. Howard, *Phys. Rev. Lett.* 72 (1994) 3040.
- [73] G. Carter, V. Vishnyakov, *Phys. Rev. B* 54 (1996) 17647.
- [74] G. Carter, V. Vishnyakov, Yu.V. Martynenko, M.J. Nobes, *J. Appl. Phys.* 78 (1995) 3559.
- [75] E-H. Cirlin, J.J. Vajo, R.E. Doty, T.C. Hasenberg, *J. Vac. Technol. A* 9 (1991) 1395.
- [76] S.W. MacLaren, J.E. Baker, N.L. Finnergan, C.M. Loxton, *J. Vac. Technol. A* 10 (1992) 468.
- [77] T.M. Mayer, E. Chason, A.J. Haward, *J. Appl. Phys.* 76 (1994) 1633.
- [78] K. Oyoshi, S. Hishita, K. Wada, S. Suehara, T. Aizawa, *Appl. Surf. Sci.* 100 (1996) 374.
- [79] F.A. Stevie, P.M. Kahara, D.S. Simons, P. Chi, *J. Vac. Technol. A* 6 (1988) 76.
- [80] Eun-Hee Cirlin, *Thin Solid Films* 220 (1992) 197.
- [81] R.M. Bradley, Eun-Hee Cirlin, *Appl. Phys. Lett.* 68 (1996) 3722.
- [82] T.A. Winningham, Z. Zou, K. Douglas, N.A. Clark, *J. Vac. Sci. Technol. A* 16 (1998) 1178.
- [83] R. Bradley, J. Harper, *J. Vac. Sci. Technol. A* 6 (1988) 2390.
- [84] I. Koponen, M. Hautala, O.-P. Sievanen, *Phys. Rev. Lett.* 78 (1997) 2612.
- [85] H. Kitani, N. Toyoda, J. Matsuo, I. Yamada, *Nucl. Instrum. Meth. B* 121 (1997) 489.
- [86] R.M. Bradley, *Phys. Rev. E* 54 (1996) 6149.
- [87] G. Carter, *Appl. Phys. Lett.* 71 (1997) 3066.
- [88] N. Toyoda, H. Kitani, N. Hagiwara, J. Matsuo, I. Yamada, *Mater. Chem. Phys.* 54 (1998) 106.
- [89] S. Matsumoto, Y. Sato, M. Kamo, N. Setaka, *Jpn. J. Appl. Phys.* 21 (1982) L183.
- [90] M.F. Ravet, F. Rousseaux, *Diamond Relat. Mater.* 5 (1996) 812.
- [91] L.A. Säfer, A. Bluhm, C.-P. Klages, B. Löchel, L.-M. Buchmann, H.-L. Huber, *Diamond Relat. Mater.* 2 (1993) 1191.
- [92] H. Tokura, C.F. Yang, M. Yoshikawa, *Thin Solid Films* 212 (1992) 49.
- [93] S. Ilias, G. Sene, P. Moller, V. Stambouli, J. Pascallon, D. Boucheir, A. Gicquel, A. Tardieu, E. Anger, M.F. Ravet, *Diamond Relat. Mater.* 5 (1996) 835.
- [94] S. Kiyohara, I. Miyamoto, T. Masaki, S. Honda, *Nucl. Instrum. Meth. B* 121 (1997) 191.
- [95] H. Buchkremer-Hermanns, C. Long, H. Weiss, *Diamond Relat. Mater.* 5 (1996) 845.
- [96] R.E. Rawles, S.F. Komarov, R. Gat, W.G. Morris, J.B. Hudson, M.P. D'Evelyn, *Diamond Relat. Mater.* 6 (1997) 791.
- [97] A. Yoshida, M. Deguchi, M. Kitabatake, T. Hirao, J. Matsuo, N. Toyoda, I. Yamada, *Nucl. Instrum. Meth. B* 112 (1996) 248.
- [98] C.L. Cheng, H.C. Chang, J.C. Lin, K.J. Song, *Phys. Rev. Lett.* 78 (1997) 3713.
- [99] D. Takeuchi, N. Shimada, J. Matsuo, I. Yamada, in: *Proceedings of the 11th International Conference on Ion Implantation Technology — IIT'96*, IEEE, Piscataway, NJ, 1997, p. 772.
- [100] K. Goto, J. Matsuo, T. Sugii, H. Minakata, I. Yamada, *IEDM Technol. Dig.* 1996, IEEE, 1996, p. 435.

- [101] K.S. Jones, G.A. Rozgonyi, in: R.B. Fair (Ed.), *Rapid Thermal Processing Science and Technology*, Academic Press, Boston, 1993, p. 123.
- [102] A. Agarwal, D.J. Eaglesham, H.-J. Gossmann, L. Pelaz, S.B. Herner, D.C. Jacobson, T.E. Haynes, Y. Erokhin, R. Simonton, Boron-enhanced-diffusion of boron: the limiting factor for ultra-shallow junction, *IEDM Technol. Dig.* (1997) 467.
- [103] A. Agarwal, H.-J. Gossmann, D.J. Eaglesham, L. Pelaz, D.C. Jacobson, T.E. Haynes, Y.E. Erokhin, *Appl. Phys. Lett.* 71 (1997) 3141.
- [104] L.C. Feldman, R.L. Kaufmann, P.J. Silverman, *Phys. Rev. Lett.* 39 (1977) 38.
- [105] M. Rodder, Q.Z. Hong, M. Nandakumar, S. Aur, J.C. Hu, I.-C. Chen, *IEDM Technol. Dig.* (1996) 563.
- [106] M. Bohr, S.S. Ahmed, S.U. Ahmed, M. Bost, T.R. Ghani, J. Greason, R. Hainsey, C. Jan, P. Packan, S. Sivakumar, S. Thompson, S. Yang, *IEDM Technol. Dig.* (1996) 847.
- [107] J. So, E. Crabbe, P. Agnello, E.W. Nowak, R. Schultz, S. Rauch, H. Ng, T. Newman, A. Ray, M. Hargrove, A. Acovic, J. Snare, S. Crowder, B. Chen, J. Sun, B. Davari, in: *Proceedings of the Symposium on VLSI Technology, Technol. Dig., IEEE* (1996) 12.
- [108] M. Akizuki, J. Matsuo, M. Harada, S. Ogasawara, A. Doi, K. Yoneda, T. Yamaguchi, G.H. Takaoka, C.E. Ascheron, I. Yamada, *Nucl. Instrum. Meth. B* 99 (1995) 225.
- [109] J. Matsuo, W. Qin, M. Akizuki, T. Yodoshi, I. Yamada, *Mat. Res. Soc. Symp. Proc.* 504 (1997) 87.
- [110] J. Matsuo, H. Katsumata, E. Minami, I. Yamada, *Nucl. Instrum. Meth. B* (2000), in press.
- [111] NEDO consortium program, 1997–1999, Project leader: Isao Yamada, Project office: Osaka Science and Technology Center, Utsubo, Osaka Japan: R&D for ultra-high quality transparent conductive film fabrication.
- [112] US Department of Commerce Advanced Technology Program Contract 1998-06-0028A Gas Cluster Ion Beam Manufacturing Tool for Next-Generation Semiconductor Devices, Epion Corporation.
- [113] MITI Millennium Project, 2000–2005, Project leader: Isao Yamada, Project office: Osaka Science and Technology Center, Utsubo, Osaka Japan: R&D for cluster ion beam process technology.